

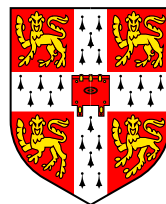
A STOCHASTIC APPROACH TO CONDENSED MATTER PHYSICS

Andrew J. Morris

A STOCHASTIC APPROACH TO CONDENSED MATTER PHYSICS

Andrew J. Morris

Selwyn College
University of Cambridge



A dissertation submitted for the degree of
Doctor of Philosophy

September 2009

Abstract

IN THIS DISSERTATION we discuss two important areas of condensed matter physics. In Part I we explore ultracold atom systems, the new test-bed for quantum mechanics. We use highly accurate quantum Monte Carlo (QMC) techniques. Within QMC we study the BEC-BCS crossover and perform the most accurate QMC calculation to date of the universal parameter ξ . The momentum density and the condensate fraction in the unitarity limit are presented.

In Part II, we apply the new technique of “*ab initio* random structure searching” (AIRSS) to point-defects in semiconductors. Using this technique within the framework of the well-established density-functional theory several new structures are calculated. First, we study how hydrogen molecules dissociate in bulk silicon to form point defects. Several new low-energy hydrogen/silicon defects are reported and thermodynamical calculations are performed to show which ones are the most likely to form.

Our attention is then turned to nitrogen and hydrogen defects in silicon and diamond. AIRSS is shown to reproduce easily the DFT ground states of all of the previously-known defects that we attempted: an important step in testing the method. Finally, the binding of hydrogen to nitrogen/oxygen defects in bulk silicon is studied. Four new hydrogen/nitrogen/oxygen complexes are presented.

Declaration

THIS DISSERTATION IS A result of my own work during my time with the Theory of Condensed Matter group in the Cavendish Laboratory, University of Cambridge. It includes nothing which is the outcome of work done in collaboration except where specifically indicated in the text.

This dissertation does not exceed 60,000 words in length.

Parts of this dissertation have been published, or submitted for publication, as follows.

Chapter 4: Andrew J. Morris, Pablo López Ríos, and R. J. Needs, “*Ultracold atoms at unitarity within quantum Monte Carlo.*”, In review with *Phys. Rev. A*.

Chapter 8 & part of 2: Andrew J. Morris, Chris J. Pickard and R. J. Needs, “*Hydrogen/silicon complexes in silicon from computational searches.*”, *Phys. Rev. B* **78**, 184102 (2008) [1].

Chapter 10: Andrew J. Morris, Chris J. Pickard and R. J. Needs, “*Hydrogen/nitrogen/oxygen complexes in silicon from computational searches.*”, *Phys. Rev. B* **80**, 144112 (2009) [2].

Andrew J. Morris
September 2009

Acknowledgements

THIS DISSERTATION WOULD NOT have been possible without a large number of people's help throughout my time in Cambridge. The scientific support I acknowledge here, the emotional I believe is better done in person, so will not feature below.

First of all, I thank my supervisor, Prof. Richard Needs for his guidance and patience throughout. He gave me the best ideas and made sure that my own ideas did not bring me to too much harm. I thank my collaborators Pablo López Ríos and Chris Pickard for their help throughout my projects.

A theoretical physicist depends heavily on the computational resources available. Without Michael Rutter's dedication to TCM's computing this dissertation would have taken much longer to write. I thank him also for his help with computing problems and without it, minor problems would have caused major delays.

Another great asset to TCM is Tracy Ingham, who has hidden the administrative burden well, so that I could concentrate on physics.

Office mates have been a great source of wisdom, so I thank Mark Robinson, Alexander Badinski and Matthew Brown for their help.

There are few doors in TCM on which I have not knocked to find answers to one of my *quick questions*. The willingness of people behind those doors to help and their patience when I have knocked a second time, has always amazed me. The people behind those doors were Profs Ben Simons, David Khmelnitskii and Matthew Foulkes: Drs Neil Drummond, James Kermode, Jonathan Yates, John Trail, Nick Hine, Jonathan Keeling and Norbert Nemec.

I also acknowledge the help and continuing guidance of those from afar, namely Rex Godby, Matthew Probert, Phil Hasnip, Kris Delaney, Martin Stankovski and David Quigley who shaped my interest in electronic structure and directed me towards Cambridge.

I also thank two great friends in college and the Cavendish, Fay Tuddenham and Gareth Conduit for many a topical discussion over breakfast, lunch, dinner or supper and for the careful reading of early drafts of this dissertation.

Contents

List of Figures	xiii
List of Tables	xv
1 Overview	1
2 Introduction	3
2.1 Electronic Structure – An Overview	3
2.1.1 Ground State Properties	4
2.1.2 Excited State Properties	5
2.2 The N -body Problem	9
2.3 Hartree Method	10
2.4 Hartree-Fock Theory	12
2.5 Beyond Hartree-Fock	14
2.6 Density-Functional Theory	16
2.6.1 Hohenberg and Kohn	16
2.6.2 Kohn-Sham	17
2.6.3 The <i>Exchange-Correlation</i> Functional – E_{xc}	19
2.6.4 Applications of DFT	20
2.7 Computational Methods	21
2.7.1 Planewaves and Pseudopotentials	22
2.7.2 Convergence	23
2.7.3 The Accuracy of Basis Sets	25
2.7.4 Wavefunction Manipulation	25
2.7.5 Brillouin Zone Sampling Scheme	28

I Random Wavefunction Sampling	33
3 Sampling the Wavefunction with Random Numbers	35
3.1 Introduction to Quantum Monte Carlo	35
3.2 Monte Carlo Method	36
3.3 Variational Monte Carlo	39
3.3.1 Trial Wavefunction	41
3.3.2 The Jastrow Factor	42
3.3.3 Backflow	42
3.3.4 Wavefunction Optimisation	43
3.4 Diffusion Monte Carlo	45
3.4.1 Trial Wavefunction	45
3.4.2 Overview	45
3.4.3 Importance Sampling	47
3.4.4 Practicalities	48
3.5 The Tiling Problem	52
4 Ultracold Atomic Gasses at Unitarity	55
4.1 The Hamiltonian	57
4.2 QMC Methods	58
4.2.1 VMC and DMC Calculations for Fermi Atomic Gases	58
4.2.2 Trial Wavefunctions	59
4.2.3 QMC Calculations	62
4.3 Results	63
4.3.1 Total Energy and the ξ Parameter	63
4.3.2 Pair-Correlation Functions	64
4.3.3 Momentum Density and Density Matrices	66
4.3.4 Varying the Particle Density	68
4.4 Conclusions	70
5 Discussion	73
5.1 Summary	73
5.2 Outlook	75

II Random Structure Searching	79
6 Sampling Structures with Random Numbers	81
6.1 Introduction	81
6.2 Search Methods	84
6.2.1 Simulated Annealing	87
6.2.2 Genetic Algorithms	91
6.2.3 Random Structure Searching	93
6.3 Summary	97
7 Point Defects	99
7.1 Introduction	99
7.2 Experimental Methods	100
7.2.1 Vibrational Spectroscopies	102
7.2.2 Electron Paramagnetic Resonance Imaging	103
7.3 <i>Ab initio</i> Quantities	103
8 Hydrogen in Silicon	105
8.1 Introduction	105
8.2 Computational Approach	107
8.2.1 Random Structure Searching	107
8.2.2 Density-Functional-Theory Calculations	108
8.3 Calculating the Formation Energies	109
8.4 Results	110
8.5 Relative Abundances	115
8.6 Discussion	119
9 Hydrogen / Nitrogen defects in Silicon and Diamond	121
9.1 Introduction	121
9.2 Computational Approach	125
9.3 Results	126
9.3.1 Nitrogen in Silicon	126
9.3.2 Nitrogen in Diamond	129
9.3.3 Hydrogen and Nitrogen in Silicon	134
9.3.4 Hydrogen and Nitrogen in Diamond	136

9.4 Discussion	140
10 Hydrogen / Nitrogen / Oxygen defects in Silicon	143
10.1 Introduction	143
10.2 Computational Approach	145
10.2.1 Random Structure Searching	145
10.2.2 Justification of the Use of 32-Atom Cells	145
10.3 Calculating the Formation Energies	146
10.4 H/N Defects	149
10.5 N/O Defects	149
10.6 H/O Defects	150
10.7 H/N/O Defects	151
10.8 Relative Abundances	152
10.9 Discussion	157
11 Discussion	161
11.1 AIRSS Defect Method	161
11.2 Discussion	164
11.3 AIRSS Outlook	165
A Trial Wavefunctions as a Product of Two Slater Determinants	169
B Pairing Wavefunctions	171
Glossary	173
Bibliography	179
Index	190

List of Figures

2.1	Convergence Tests – Planewave Cut-off	25
2.2	Fourier Transform Grid Sizes	27
2.3	Convergence Tests – FT Grids	28
2.4	A Comparison of BZ Sampling Schemes.	31
3.1	Archery Analogy	38
3.2	Reblocking Plot	41
3.3	Representation of the DMC Algorithm	49
3.4	Timestep Error	50
3.5	Population Control Bias	51
4.1	Gaussian and Polynomial Pairing Orbital Evaluation Speed	60
4.2	Energy per Particle of the Non-Interacting System	64
4.3	Pair-Correlation Functions	66
4.4	Momentum Density and One-Body Density-Matrix	68
4.5	The Two-Body Density-Matrix	69
6.1	Allotropes of Carbon	83
6.2	Energy Surface	84
6.3	Golden Section Search	86
6.4	Lennard-Jones Atomic Clusters	87
6.5	Example Auxiliary Surface	89
6.6	The Genetic Algorithm	93
6.7	The Random Structure Searching Algorithm.	95
7.1	The Czolchalski Process	101

8.1	Formation Energies of Si/H Defects in Silicon	112
8.2	Two Projections of the New {I, H} Defect	112
8.3	The Most Stable {I, H ₂ } Defect	113
8.4	The Second Most Stable {I, H ₂ }* Defect	114
8.5	The New {I, H ₃ } Defect	114
8.6	The New {I, H ₄ } Defect	115
8.7	Relative Abundances of the Si/H Defects	116
9.1	Double-Nitrogen Defects in Silicon	127
9.2	The {4N _s , V} Defect in Diamond	129
9.3	{H ₂ }* Defect in Diamond	130
9.4	Double-Nitrogen Defects Diamond	131
9.5	Single-Nitrogen Defects in Diamond	132
9.6	Hydrogen/Nitrogen Defects in Silicon	135
9.7	Hydrogen/Nitrogen Defects in Diamond	137
9.8	The {N _i , 2H _i } Defect	138
10.1	The {3O _i } Defect	152
10.2	N/O Defects in Silicon	153
10.3	H/O Defects in Silicon	153
10.4	H/N/O Defects in Silicon	154
10.5	Relative Conc. of H/N/O Complexes as a Function of N Conc. . .	155
10.6	Relative Conc. of H/N/O Complexes as a Function of O Conc. . .	156
10.7	Relative Conc. of H/N/O Complexes as a Function of H Conc. . .	156

List of Tables

2.1	Total Energies of Selected Atoms	21
4.1	Values of ξ	65
4.2	Condensate Fraction c	68
4.3	ξ as a Function of r_s	69
8.1	Formation Energies of Silicon Self-interstitial Defects	110
8.2	Formation Energies of Hydrogen Defects in Silicon	111
8.3	Formation Energies of Si/H Defects in Silicon	111
8.4	Linear Programming Constraints for Rel. Abundances	117
9.1	Formation Energies of Nitrogen and Hydrogen Defects in Silicon . .	128
9.2	Formation Energies of Nitrogen and Hydrogen Defects	130
9.3	Bond Lengths of $\{N_s, 2H_i\}$	139
10.1	Formation Energies of Different Oxygen Complexes	148
10.2	Defect Formation Energies	148

Chapter 1

Overview

On two occasions I have been asked, “Pray, Mr. Babbage, if you put into the machine wrong figures, will the right answers come out?” I am not able rightly to apprehend the kind of confusion of ideas that could provoke such a question.

Charles Babbage

THIS DISSERTATION CONTAINS two quite distinct topics within condensed matter physics. However, these topics do have common themes. The first concept is *simulation*, in our case the use of computers to model the behaviour of atoms in solids. *Simulation* can be thought of as an experiment in a computer. Most modern theoretical problems in physics are too hard to solve analytically. With simulation, we explicitly state the initial conditions and dynamical rules of the problem, and allow the computer to propagate them to a solution. The advantage of this approach is the ability to *turn off* parts of physics to see what is important to the outcome of the problem. For example, we can freeze the core electrons of an atom in a calculation. This will not only speed up the calculation, but also demonstrates that it is the valence electrons that are important in chemical bonding. In a computer we are also able to simulate processes at finite temperatures, pressures and magnetic

field strengths which would not be accessible in a laboratory environment, such as the Earth's core [3, 4, 5].

The lowest energy structures of bulk solids are the ones most likely to form naturally and hence they are the ones most interesting to scientists. Therefore it is important to be able to accurately calculate the energy of a structure. The lowest energy structure is known as the *ground state*.

The second concept which runs throughout this dissertation is *random numbers* which are used to generate low-energy structures and to calculate ground-state energies. In Part I in order to obtain the ground-state energy of a system, random numbers are used to evaluate

$$\frac{\int \Psi^* \hat{H} \Psi d\mathbf{R}}{\int \Psi^* \Psi d\mathbf{R}}. \quad (1.1)$$

This method is known as *quantum Monte Carlo* (QMC). The *configurations* of the system used to sample the wavefunction follow a random walk.

In contrast in Part II random numbers are used to generate random trial structures. These structures are then relaxed using density-functional theory (DFT) methods, explained in Sect. 2.6. The lowest energy relaxed structures are then further analysed by computational techniques.

Chapter 2 introduces electronic structure methods and the different techniques for approximating a solution to the many-body problem. Part I contains Chapters 3, 4 and 5. The first introduces the QMC method and the second goes on to apply it to a system of interacting ultracold atoms. The third chapter concludes the work on QMC and gives an outline of my views on the future of QMC calculations. In Part II, Chapter 6 introduces the random structure searching method. Chapter 7 explains the importance of the theoretical study of point-defects. Random structure searching is then applied to hydrogen / silicon defects in silicon in Chapter 8, hydrogen / nitrogen defects in silicon and diamond in Chapter 9 and hydrogen / nitrogen / oxygen complexes in silicon in Chapter 10.

Chapter 11 concludes the work on random structure searching and discusses its place in the structure prediction field.

Chapter 2

Introduction

2.1 Electronic Structure – An Overview

IT IS INDEED DIFFICULT TO OVERSTATE the reasons why we *do* electronic structure calculations. The last century or so has seen huge developments in the understanding of the fundamentals of science. The discovery of a full quantum mechanical theory in the 1920s has led to an understanding of matter at very small length-scales. In line with this new understanding, technological advances occur at an unprecedented pace, transmogrifying all aspects of human life.

An understanding of *Cathode Rays*, later identified as electrons, not only kick-started the field of electronics, giving us the radio and television, but, with the invention of the transistor, paved the way for microchips, the constituent “brains” behind computers which have dramatically changed everyday life (as well as theoretical physics). The invention of the laser has made possible the CD player and high-speed telecommunications.

Our understanding of composite ceramics, alloys and plastics has allowed us to build spacecraft capable of taking photos of other worlds and even escape from the solar system. A little nearer to home, we can build satellites for global positioning (GPS), satellite TV and weather monitoring.

Knowledge of molecules and their bonding gave us the ability to decode DNA, the building block of life. An understanding of how proteins fold within the body

and chemical reaction rates have led us to new drugs and treatments. Progress with nuclear magnetic resonance (NMR) and X-ray photography has benefitted medicine and avoided much exploratory surgery.

Advances in technology such as those above rely on an understanding of the characteristics of materials. We must understand how the constituent atoms are bonded together and how the material reacts under pressure or high temperature. We need to calculate how it reacts with air, water and other materials. We must know how it emits and absorbs light, conducts electricity and behaves in magnetic fields.

*Ab initio*¹ electronic structure calculations can describe these things in detail. And for these reasons we *do* electronic structure calculations.

2.1.1 Ground State Properties

Broadly, there are two types of electronic structure properties: ground state properties, described in this section and excited state; described in the next.

The ground state is the lowest energy configuration of electrons and nuclei in a solid. It is important as at room temperature almost all materials are very close to their ground state. DFT can be used to calculate reasonably accurate ground state energies of solids. We can calculate the forces on the ions once we know the energy of a structure. Using these forces we can *relax* the ionic positions of solids to their ground state. This allows us to determine the structure of a solid from first principles, and enables the calculation of lattice constants, bulk moduli and other properties. In practice structure determination is subtly more complicated, as we will discuss in Chapter 6. The calculation of, for example, the vibrational modes of a solid, NMR or electron paramagnetic resonance (EPR) spectra allows direct comparison between *ab initio* derived structures and experiment.

By calculating the ionic forces on molecules, we can “watch” chemical reactions take place. For example, we can observe how hydrogen diffuses through structures and how tightly it bonds to bulk materials. This understanding is important for

¹From first principles: meaning the calculation from an understanding of quantum mechanics rather than fitted to experimental data.

hydrogen storage as the material must be able to hold hydrogen safely until it is required, then release it easily. Once this is possible hydrogen fuel cells should become much more practical as a means of powering cars. However, DFT is not always accurate enough, and other methods are generally too expensive to perform the many thousands of energy calculations required. It should be possible, however, when using *linear-scaling* DFT [6], to calculate how proteins and biological molecules fold which is important for biology and the pharmaceuticals industry. Using the recent *learn-on-the-fly* technique [7, 8], it is possible to model how biological molecules behave in water, adding much realism to the calculations. Learn-on-the-fly treats different parts of the simulation with different levels of accuracy and dynamically changes these regions as required. For example, in the propagation of a crack in silicon, the behaviour of the tip of the crack can be calculated quantum mechanically, whereas the rest of the bulk need only be treated with classical forces.

From the ground state energy, we can also calculate the binding energy of molecules. For small molecules we can use very accurate Configuration Interaction (CI) techniques (which includes van der Waals interactions not described by standard DFT) to recover almost exactly the experimental energies. To perform calculations on larger systems than is possible using CI we use quantum Monte Carlo, which is described in Chapter 3.

In Part II point defects in bulk silicon and diamond are studied. These change the properties of semiconductors, including how they conduct an electric current. This is important to the electronics industry and is also describable within ground state calculations.

2.1.2 Excited State Properties

An excited state is any state of the system that is not the ground state. Excited state properties are very important as they describe how a system responds to an input of energy – perhaps caused by a lattice vibration, or an incident photon. A lot of excited state properties are accessible to experiment as probes such as neutrons, electrons or photons excite the system from the ground state. For example, in electron energy loss spectroscopy (EELS) a beam of electrons with a given kinetic

energy is inelastically scattered from a solid. By measuring the energy loss of the scattered electrons the structure of the solid can be inferred.

Many of the more recent technological advances have involved the interaction of light with solids. A photon absorbed by a metal causes an electron to be excited from its ground state, leaving behind a hole. The electron and hole interact, leading to a two-particle excitation which can be described by the Bethe-Salpeter equation [9]. Time-dependent-DFT (TDDFT) [10], (a generalisation of DFT for time-dependent potentials), allows the calculation of absorption spectra and the electron energy levels of atoms.

The experimental technique of angle-resolved photoemission spectroscopy (ARPES) allows the determination of the energy and momentum of electrons in the material by irradiating the sample with high energy photons. Single particle excitations can be described by Hedin's *GW* approximation to many-body perturbation theory [11, 12]. This can be used to gain an understanding of quantum transport which is the theory of electricity at the quantum level.

With an understanding of the energy and momentum of electrons in a material, we are able to understand a material's *band structure*. For example, an atom has orbitals that only electrons of certain energies are allowed to occupy, whereas free-electrons (ones not experiencing a potential) may occupy a continuum of states. Most bulk materials lie between these two extremes. Within bulk materials there are *bands* of allowed electron energies. If a band is completely filled with electrons (called a *valence band*), and if there is a large energy gap between it and the next empty band (the *conduction band*), the material is an insulator. Electrons need to gain a large amount of energy before they are free to travel long distances (conduct) in the unoccupied conduction band. A smaller gap between full (occupied) and empty (unoccupied) bands implies a semiconductor. No gap, or a partially-filled band tells us that the material is a metal.

Even within DFT, a ground state theory, it is possible to glean information about the band structure of crystals. For more accurate results we may use the *GW* approximation. By changing the physical structure of a semiconductor, we can change the bands of the material and for example, tune its band gap. This in turn

changes the frequency of the photon emitted when an electron in the conduction band recombines with the hole left in the valence band. This is the principle behind the light emitting diode (LED).

It is clear that there are many interesting problems to investigate and many techniques devised to solve them. I now begin a description of some of the techniques available.

2.2 The N-body Problem

The two-body problem, for example, a planet orbiting a sun, or an electron orbiting a nucleus can be solved analytically. In August 1684 Edmund Halley (1656–1742), struggling to understand the path of a body moving around a central force, travelled to Trinity College, Cambridge to ask Isaac Newton (1643–1727) if he knew the solution. Newton was able to tell him that it followed an elliptical path.

Most of the interesting systems in physics, however, contain more than two bodies. It is generally the complexity of a system that makes it *interesting* to physicists. Even the three-body problem of a planet orbiting a binary star is not solvable analytically. Hence in order to model a solid containing $\sim 10^{23}$ electrons, approximations are clearly required.

Quantum mechanical problems generally require solving the Schrödinger equation for many particles. The solution of this is the “holy grail” of quantum physics. However, the Schrödinger equation is usually impossible to solve in all but the simplest cases.

For time-independent problems the Schrödinger equation reduces to a simpler, but only slightly easier to solve, eigenvalue problem,

$$\hat{H}\phi_i = E_i\phi_i, \quad (2.1)$$

where ϕ_i are the (energy) eigenstates of the Hamiltonian, \hat{H} , and E_i are the (energy) eigenvalues. The lowest E_i is the ground state energy, E_0 .

The Hamiltonian of a system of N interacting electrons, in atomic units² and M interacting ions is written as,

$$\hat{H} = -\frac{1}{2} \sum_i^N \nabla_i^2 + \frac{1}{2} \sum_{i \neq j}^N \sum_j^N \frac{1}{|\mathbf{r}_i - \mathbf{r}_j|} - \sum_i^N \sum_{\alpha}^M \frac{Z_{\alpha}}{|\mathbf{r}_i - \mathbf{R}_{\alpha}|} + \frac{1}{2} \sum_{\alpha \neq \beta}^M \sum_{\alpha}^M \frac{Z_{\alpha}Z_{\beta}}{|\mathbf{R}_{\alpha} - \mathbf{R}_{\beta}|},$$

where the terms are, in order, the kinetic energy of the electrons, the Coulomb interaction between electrons, the Coulomb interaction energy between electrons

²The electron mass, electronic charge, the reduced Planck constant (\hbar) and the Bohr radius are all set to unity. Hence energies are reported in Hartrees.

and ions, and the Coulomb interaction between ions. The latter is a constant as the ions are assumed to be fixed, using the Born-Oppenheimer approximation [13]. We argue that since the proton is 1836 times heavier than the electron, it generally travels much more slowly than the electron. The quantum mechanical representation of the nucleus can then be replaced by a classical Coulomb potential acting on the “quantum” electron.

Now we have a Hamiltonian for our system, the Variational principle tells us that for *any* wavefunction, Ψ , we have,

$$\frac{\int \Psi^* \hat{H} \Psi \, d\mathbf{r}_1, \dots, d\mathbf{r}_N}{\int \Psi^* \Psi \, d\mathbf{r}_1, \dots, d\mathbf{r}_N} \geq E_0, \quad (2.2)$$

where the equality holds for $\Psi = \phi_0$. This now gives us a prescription for finding an approximate solution to Eqn. 2.1 by approximating the MB wavefunction.

The MB wavefunction is a function of each electron’s position. Hence for a system of N -electrons, the problem is $3N$ -dimensional. We define the MB wavefunction $\Psi(\mathbf{r}_1, \sigma_1, \mathbf{r}_2, \sigma_2, \dots, \mathbf{r}_N, \sigma_N)$ where \mathbf{r}_i is the spatial and σ_i is the spin co-ordinate of the i^{th} particle.

2.3 Hartree Method

Perhaps the simplest method is the *mean-field* Hartree [14] approximation. The Hartree method assumes the wavefunction is separable and approximates the MB wavefunction as a product of one-electron orbitals,

$$\Psi(\mathbf{r}_1, \mathbf{r}_2, \dots, \mathbf{r}_N) = \phi_1(\mathbf{r}_1)\phi_2(\mathbf{r}_2)\dots\phi_N(\mathbf{r}_N). \quad (2.3)$$

When these orbitals $\phi_i(\mathbf{r}_i)$ are squared and summed they give the electron density,

$$n(\mathbf{r}) = 2 \sum_i |\phi_i(\mathbf{r}_i)|^2, \quad (2.4)$$

where doubling the sum takes into account electron spin. Minimising the energy in the Schrödinger equation with respect to the form of the Hartree orbitals gives an

eigenvalue problem of the form

$$\hat{H}_H \phi_i = \epsilon_i \phi_i, \quad (2.5)$$

where \hat{H}_H is the Hartree Hamiltonian, ϕ_i are the Hartree one-electron orbitals.

The Hartree Hamiltonian takes the form,

$$\hat{H}_H = \left[-\frac{\nabla_{\mathbf{r}_i}^2}{2} + V_{\text{ext}}(\mathbf{r}_i) + V_{\text{eff}}^i(\mathbf{r}_i) \right], \quad (2.6)$$

where V_{ext} is the electron-ion energy and V_{eff}^i is an effective orbital-dependent potential, described by the Hartree potential,

$$V_{\text{eff}}^i(\mathbf{r}_i) = V_H^i(\mathbf{r}_i) = \sum_{j \neq i}^N \int \frac{|\phi_j(\mathbf{r}_j)|^2}{|\mathbf{r}_i - \mathbf{r}_j|} d\mathbf{r}_j. \quad (2.7)$$

The electrons are thus described as *non-interacting* (with each other) but experience the Hartree potential, which is the *average* Coulomb interaction of all of the other electrons. This is a *mean-field* approximation. The total energy is obtained from the sum of the eigenvalues minus the double-counted electrostatic terms.

The Hartree method overestimates the potential energy of electrons, that is, the Hartree energy, E_H , derived from the Hartree potential is too large. It has omitted two important factors. Firstly that Electrons are fermions, so like-spin electrons are kept apart by the Pauli Exclusion Principle; which reduces their contribution to the potential energy. Secondly, *interacting* electrons repel each other, thus further lowering the potential energy through their correlated motion.

The Hartree potential is itself a function of the orbitals. Therefore the Hartree equation must be solved self-consistently, until the total energy converges. Sometimes the Hartree method is simplified by removing the orbital dependence of V_H^i . The sum in Eqn. 2.7 is then performed over all j , including $i = j$. This of course means that only one V_H must be calculated during each self-consistency cycle but introduces a *self-interaction error*, as the electron in orbital i experiences a Coulomb force from its own contribution to V_H . I note that the more modern usage of “Hartree Energy” implies that $i = j$ term is present.

The Hartree method is usually qualitatively correct, but is not really accurate enough to be used for predictions. As there are more accurate methods with the same computational cost, the Hartree method is no longer used. These reasons, along with the lack of the Pauli exclusion leads us to consider Hartree-Fock theory (HF).

2.4 Hartree-Fock Theory

The Pauli exclusion principle requires that the wavefunction is antisymmetric with respect to the electron co-ordinates, that is,

$$\Psi(\mathbf{r}_1, \sigma_1, \mathbf{r}_2, \sigma_2, \mathbf{r}_3, \sigma_3, \dots, \mathbf{r}_N, \sigma_N) = -\Psi(\mathbf{r}_1, \sigma_1, \mathbf{r}_3, \sigma_3, \mathbf{r}_2, \sigma_2, \dots, \mathbf{r}_N, \sigma_N).$$

However, this is not the case in Hartree theory since

$$\begin{aligned} & \phi_1(\mathbf{r}_1, \sigma_1)\phi_2(\mathbf{r}_2, \sigma_2)\phi_3(\mathbf{r}_3, \sigma_3)\dots\phi_N(\mathbf{r}_N, \sigma_N) \\ & \neq -\phi_1(\mathbf{r}_1, \sigma_1)\phi_2(\mathbf{r}_3, \sigma_3)\phi_3(\mathbf{r}_2, \sigma_2)\dots\phi_N(\mathbf{r}_N, \sigma_N). \end{aligned} \quad (2.8)$$

This led Slater [15] and Fock [16] to improve on the Hartree method by restricting the wavefunction to an antisymmetric product of one-electron orbitals. This product may be written as a *Slater determinant*,

$$\Psi(\mathbf{r}_1, \sigma_1, \dots, \mathbf{r}_N, \sigma_N) = \frac{1}{\sqrt{N!}} \begin{vmatrix} \phi_1(\mathbf{r}_1, \sigma_1) & \phi_1(\mathbf{r}_2, \sigma_2) & \cdots & \phi_1(\mathbf{r}_N, \sigma_N) \\ \phi_2(\mathbf{r}_1, \sigma_1) & \phi_2(\mathbf{r}_2, \sigma_2) & & \\ \vdots & & \ddots & \\ \phi_N(\mathbf{r}_1, \sigma_1) & & & \phi_N(\mathbf{r}_N, \sigma_N) \end{vmatrix}.$$

We can see that swapping electron co-ordinates is the same as swapping two columns in the determinant, hence changing the sign of the determinant, as required.

Again, minimising the energy with respect to the form of the orbitals in the Slater determinant defines an eigenvalue equation. This equation is of a similar form to Eqn. 2.5 but with a Hamiltonian, \hat{H}_{HF} , now orbital dependent.

The difference being the effective potential, which now contains an extra non-

local term. We must now write

$$V_{\text{eff}}^i(\mathbf{r}_i) \phi_i(\mathbf{r}_i) = V_{\text{H}}^i(\mathbf{r}_i) \phi_i(\mathbf{r}_i) + \int \Sigma_{\text{x}}^i(\mathbf{r}_i, \mathbf{r}_j) \phi_i(\mathbf{r}_j) d\mathbf{r}_j, \quad (2.9)$$

where $\Sigma_{\text{x}}^i(\mathbf{r}_i, \mathbf{r}_j)$ is the non-local *exchange* potential,

$$\Sigma_{\text{x}}^i(\mathbf{r}, \mathbf{r}') = - \sum_{k \neq i}^N \frac{\phi_i^*(\mathbf{r}') \phi_k(\mathbf{r}')}{|\mathbf{r} - \mathbf{r}'|} \delta_{\sigma_i, \sigma_k}, \quad (2.10)$$

which gives rise to an *exchange* energy. This is a correction on top of the Hartree energy E_{H} due to the Pauli exclusion principle. Σ_{x} forces like-spin electrons apart, lowering the energy. The exchange potential Σ_{x} is responsible for an *exchange hole* around the electron and screens the Coulomb interaction between like-spin electrons.

Since the effective potential is still a function of the orbitals, we still need to solve the HF equation iteratively. Importantly, the Hartree potential and exchange potential terms cancel when an electron in an orbital i is subjected to its own contribution to the mean-field Coulomb interaction. This causes the resulting HF energies and orbitals to be self-interaction free and removes the orbital dependence of the effective potential, greatly reducing the computational cost per iteration.

HF is quite successful for atoms and small molecules and reasonable for some solids. It typically produces ground-state energies within 5% of the experimental value. The HF single-particle eigenvalues may be interpreted as excitation energies, if we assume that the N -particle and $N - 1$ -particle orbitals are very similar. However, HF then catastrophically predicts that the homogenous electron gas – the archetypal model of a metallic system – is non-metallic!

Like Hartree theory, HF still overestimates the interaction energy since it does not take into account the reduction in energy from electron-electron repulsion. We define the difference between the HF energy and the true many-body ground-state energy as the *correlation energy*. The rest of the methods in this chapter are attempts to calculate the correlation energy.

2.5 Beyond Hartree-Fock

To improve upon HF we can again minimise co-efficients using a more sophisticated wavefunction. Configuration Interaction (CI) uses a set of Slater determinants as to form a MB wavefunction. These Slater determinants not only contain ground-state orbitals, as in HF, but also excited-state orbitals. The MB wavefunction is made up of a linear sum of these Slater determinants,

$$\Psi(\mathbf{r}_1, \sigma_1, \dots, \mathbf{r}_N, \sigma_N) = \sum_{i=1}^M c_i D_i(r_1, \sigma_1, \dots), \quad (2.11)$$

where c_i are the co-efficients to be optimised and D_i are the Slater determinants of the basis set.

In principle, the exact wavefunction can be obtained if M is taken to infinity, and the D_i contain all combinations of single, double, triple up to N^{th} -order excitations. In practice, it is often possible to obtain much of the correlation energy using only single and double excitations (CISD), and very accurate results can often be obtained if triple and quadruple excitations are added (CISDTQ). As the system becomes larger, higher and higher levels of excitation are required to accurately describe the wavefunction.

CI also scales very badly with the number of electrons, N : for example, full CI scales as $\mathcal{O}(N!)$, CISD scales as $\mathcal{O}(N^6)$ and CISDTQ scales as $\mathcal{O}(N^{10})$. Hence it is computationally impossible to treat systems accurately using CI with more than about 20 electrons. The outlook is bleak. Even with computing power doubling every 18 months (Moore's Law), if 20 electrons is state-of-the-art today, we must wait 15 years before 40 electron CISDTQ calculations are possible.

Hence CI is used only for the smallest benchmark calculations. There are other ways to proceed however, multi-configurational self-consistent field (MCSCF) methods optimise both the co-efficients, c_i , and the orbitals of each determinant. It is then possible to reduce the number of determinants in the description of the wavefunction.

We can also use perturbation theory to add correlations into HF theory through

the Coulomb interaction. This is Møller-Plesset theory, (MP). The second order version, MP2, scales as $\mathcal{O}(N^5)$, whereas fourth order MP4 scales as $\mathcal{O}(N^7)$.

In CI we note that all matrix elements of the Hamiltonian between Slater determinants which differ by more than two spin orbitals are zero. Further, from Brillouin's theorem, matrix elements containing the ground state Slater determinant and single excitations are also zero. Hence to obtain the correlation energy we need only the co-efficients of the doubly excited determinants, c_2 . This would reduce the computational cost but, unfortunately, to obtain c_2 from CI we need to have already evaluated the complete set of c_i .

The idea of only needing the co-efficients of the doubly excited determinants does however lead us to the independent electron-pair approximation, (IEPA). This method uses a shortcut to calculate the correlation energy, by writing down the pair-wavefunction. This wavefunction describes how two electrons behave when excited in a solid, as opposed to all of them, as in full CI. Using the pair-wavefunction we are able to obtain an approximation to the correlation energy.

We can go one step further and calculate how the pairs in IEPA interact with other pairs, using the Coupled Cluster technique (CC). The original version of Coupled cluster, called CCD, approximated c_4 as a product of c_2 co-efficients. This approximation leads to a set of closed but non-linear equations that can be solved for the energy. However the method may also be improved to take into account single excitations, as they have a small indirect effect on the double excitations, giving the CCSD method. The most common of the multi-determinant methods is the CCSD method where triple excitations are also added perturbatively, known as CCSD(T). CCSD(T) however still scales as $\mathcal{O}(N^7)$, and is not variational, since the higher order c_i are only approximate.

The QMC method described in Chapter 3, shows a much more practical $\mathcal{O}(N^3)$ scaling, which makes it possible to calculate properties of bulk systems.

2.6 Density-Functional Theory

Density-functional theory (DFT) is a theory of the ground-state properties of an interacting MB system. Its history goes back to Thomas-Fermi theory, [17, 18], which makes some severe approximations to the kinetic energy of the electrons. DFT by comparison uses an *exact*, albeit *non-interacting*, kinetic energy operator. It is by far the most widely adopted electronic structure method used by both physicists and chemists. DFT is a very large field and we only outline the basics. The interested reader can find more information in the review article by Jones and Gunnarsson [19], or the excellent book by R. M. Martin [20].

DFT reformulates the MB problem in terms of the electron density at each point in space, $n(\mathbf{r})$, that is a function of only 3 spatial variables instead of the $3N$ of the MB wavefunction.

2.6.1 Hohenberg and Kohn

Hohenberg and Kohn [21] showed that the external potential, $V_{\text{ext}}(\mathbf{r})$ of a MB system is uniquely determined by the ground-state electron density. They showed that there exists a system-independent functional, $F[n(\mathbf{r})]$, such that,

$$E[n(\mathbf{r})] = F[n(\mathbf{r})] + \int n(\mathbf{r}) V_{\text{ext}}(\mathbf{r}) \, d\mathbf{r}, \quad (2.12)$$

where $E[n(\mathbf{r})]$ is the total energy of the ground state of the system.

From this, the ground-state energy can be derived using the Variational Principle by minimising $E[n(\mathbf{r})]$ subject to the constraint that the total number of particles, N , is fixed since,

$$N = \int n(\mathbf{r}) \, d\mathbf{r}. \quad (2.13)$$

A Lagrange multiplier, μ , is used to obtain,

$$\delta \left\{ F[n(\mathbf{r})] + \int n(\mathbf{r}) V_{\text{ext}}(\mathbf{r}) \, d\mathbf{r} - \mu \left[N - \int n(\mathbf{r}) \, d\mathbf{r} \right] \right\} = 0, \quad (2.14)$$

which leads to,

$$\frac{\delta F[n(\mathbf{r})]}{\delta n(\mathbf{r})} + V_{\text{ext}}(\mathbf{r}) = \mu, \quad (2.15)$$

where,

$$\frac{\delta F[n(\mathbf{r})]}{\delta n(\mathbf{r})} = \lim_{\delta n(\mathbf{r}) \rightarrow 0} \frac{F[n(\mathbf{r}) + \delta n(\mathbf{r})] - F[n(\mathbf{r})]}{\delta n(\mathbf{r})}, \quad (2.16)$$

defines the functional derivative. All of Hohenberg and Kohn's derivations were exact, but the form of $F[n(\mathbf{r})]$ was unknown and remains so.

2.6.2 Kohn-Sham

The fundamental assumption of Kohn and Sham [22] was that for any interacting system, a local single-particle potential can reproduce the density of the interacting system from the ground-state density of a fictitious system of *non-interacting* particles.

$F[n(\mathbf{r})]$ is divided into 3 parts,

$$F[n(\mathbf{r})] = \mathcal{T}_s[n(\mathbf{r})] + E_H[n(\mathbf{r})] + E_{\text{xc}}[n(\mathbf{r})], \quad (2.17)$$

where $E_H[n(\mathbf{r})]$ is the usual Hartree energy, $E_{\text{xc}}[n(\mathbf{r})]$, is the *exchange and correlation energy* and $\mathcal{T}_s[n(\mathbf{r})]$ is the kinetic energy of a system of *non-interacting* electrons with the same $n(\mathbf{r})$. E_{xc} contains the electron-electron interactions of the MB system beyond Hartree theory.

For the non-interacting system $F[n(\mathbf{r})] = F_s[n(\mathbf{r})] = \mathcal{T}_s[n(\mathbf{r})]$, so the Lagrange equation analogous to Eqn. 2.15 may be written as

$$\frac{\delta \mathcal{T}_s[n(\mathbf{r})]}{\delta n(\mathbf{r})} + V_s(\mathbf{r}) = \mu, \quad (2.18)$$

where $V_s(\mathbf{r})$ is some local potential to be determined that has been adjusted so that μ is the same in both equations. Rearranging Eqns. 2.15 and 2.18 we obtain,

$$V_s(\mathbf{r}) = \frac{\delta F[n(\mathbf{r})]}{\delta n(\mathbf{r})} + V_{\text{ext}}(\mathbf{r}) - \frac{\delta \mathcal{T}_s[n(\mathbf{r})]}{\delta n(\mathbf{r})}, \quad (2.19)$$

which, after taking the functional derivative of Eqn. 2.17 and substituting, gives the

effective Kohn-Sham potential as

$$V_{\text{KS}} = V_s(\mathbf{r}) = V_H(\mathbf{r}) + V_{\text{ext}}(\mathbf{r}) + \frac{\delta E_{\text{xc}}[n(\mathbf{r})]}{\delta n(\mathbf{r})}. \quad (2.20)$$

We have shown that Kohn-Sham theory replaces the MB problem with one of independent particles moving in a local *Kohn-Sham potential*, V_{KS} . It is possible to write down a Schrödinger-type equation for these fictitious non-interacting particles

$$-\frac{1}{2}\nabla_{\mathbf{r}_i}^2\phi_i(\mathbf{r}) + V_{\text{KS}}\phi_i(\mathbf{r}) = \epsilon_i\phi_i(\mathbf{r}). \quad (2.21)$$

The eigenvalues of Eqn. 2.21 are the Lagrange multipliers and should not be confused with the eigenvalues of the interacting system. The eigenvalue of the highest occupied state ϵ_N however, is equal to the chemical potential. The Kohn-Sham orbitals $\phi_i(\mathbf{r})$ are related to the full MB wavefunction since their modulus squared is equal to the ground-state density, $n(\mathbf{r})$.

Eqn. 2.21 must be solved iteratively. An effective potential V_{KS} is estimated, which through the Kohn-Sham equation gives rise to a ground-state density. This density is then used to obtain a better approximation for V_{KS} .

The sum of the eigenvalues may be written from its constituent energy contributions,

$$\sum_{i,\text{occ}}\epsilon_i = \mathcal{T}_s[n(\mathbf{r})] + \int n(\mathbf{r})V_H d\mathbf{r} + \int n(\mathbf{r})V_{\text{ext}} d\mathbf{r} + \int n(\mathbf{r})V_{\text{xc}} d\mathbf{r}, \quad (2.22)$$

where V_{xc} is defined as the functional derivative of E_{xc} with respect to the density and since,

$$E_H[n(\mathbf{r})] = \frac{1}{2} \iint \frac{n(\mathbf{r})n(\mathbf{r}')}{|\mathbf{r} - \mathbf{r}'|} d\mathbf{r} d\mathbf{r}', \quad (2.23)$$

$$V_H(\mathbf{r}) = \frac{\delta E_H[n(\mathbf{r})]}{\delta n(\mathbf{r})} = \int \frac{n(\mathbf{r}')}{|\mathbf{r} - \mathbf{r}'|} d\mathbf{r}', \quad (2.24)$$

we can use Eqns. 2.12 and 2.17 to obtain the ground-state energy,

$$E[n(\mathbf{r})] = \sum_{i,\text{occ}} \epsilon_i - \frac{1}{2} \iint \frac{n(\mathbf{r}) n(\mathbf{r}')}{|\mathbf{r} - \mathbf{r}'|} d\mathbf{r} d\mathbf{r}' + E_{\text{xc}}[n(\mathbf{r})] \quad (2.25)$$

$$- \int n(\mathbf{r}) V_{\text{xc}} d\mathbf{r}.$$

2.6.3 The Exchange-Correlation Functional – E_{xc}

The Kohn-Sham DFT scheme is a successful prescription for obtaining the ground-state energy and density of a set of interacting electrons without having to deal explicitly with the $3N$ -dimensional MB wavefunction. In its place we have a set of non-interacting Kohn-Sham orbitals. However, so far we have “swept under the carpet” all of the MB effects and placed them into E_{xc} which is still unknown and must now be approximated.

The exchange-correlation functional, E_{xc} , contains all of the MB effects of the interacting system. Hence E_{xc} must include, amongst other things,

- the difference in kinetic energy between the non-interacting and interacting systems;
- the correction to the self-interaction which is introduced by the Hartree term³.

The best-known approximation for E_{xc} is the local density approximation (LDA). In the LDA we assume that each volume element of density contributes the same E_{xc} as if it were a homogeneous (fully interacting) electron gas (HEG) at that density. The results for the HEG were calculated using quantum Monte Carlo (QMC) by Ceperley and Alder [23] and this was parameterised by Perdew and Zunger [24]. There is also a spin-dependent version (the LSDA) applicable for spin-polarised systems. The LDA works unjustifiably well, mainly due to a fortuitous cancellation of errors between correlation and exchange energies.

Compared to bulk solids, for atoms and small molecules assuming that the exchange-correlation energy is only a function of the density at one point in space is a poorer approximation. For this reason a large number of different generalised

³This is because there is no longer an explicit exchange integral to cancel the self-interaction.

gradient approximations (GGA) have been devised. These contain a contribution from the gradient of the local-density. This class of exchange-correlation functionals is the most commonly used today. It is possible to improve further E_{xc} by making it a function of the non-interacting kinetic energy. These are the so called meta-GGGAs although the functionals soon become quite computationally expensive to calculate.

A more promising way than GGAs to go beyond the LDA is the optimised effective potential (OEP) method. Here the exchange-correlation functional is made an explicit functional of the orbitals. This makes it much more difficult to obtain its functional derivative, which must now be obtained from a response function, (as in time-dependent DFT)⁴. This makes OEP a very expensive method. The advantages are that the self-interaction can be completely removed from DFT allowing the computation of exact-exchange (EXX). OEP was approximated in the method of Krieger, Li and Iafrate [25] (KLI).

2.6.4 Applications of DFT

DFT is widely used for ground-state energies and gives good ground-state charge densities. It predicts the lattice structure of crystalline materials quite well, hence is useful for structure determination. The forces on the ions may be calculated from the derivatives of the energies, and the ions are moved to minimise the forces thereby minimising the ground-state energy. This method is covered in more detail in Chapter 6.

The orbitals produced by a DFT calculation are important as they allow us to calculate the ground-state charge density $n(\mathbf{r})$ and approximations to many other quantities of interest. They are also the usual initial orbitals for a wide range of other MB methods, such as QMC and the GW approximation [12, 26].

DFT is not so good for surface properties nor is it good at calculating hydrogen bonds, since V_{xc} is local there is an absence of long range correlation, hence it also does not describe van der Waals forces. It cannot describe effects where an electron brought close to a surface, polarises the surface and experiences an attraction to the *image charge*.

⁴The generalisation of DFT to time-dependent potentials. See [10].

Atom	HF	DFT-LDA	DFT-KLI	CI
He	-1.4303 ^a	-1.4171	-1.43089	-1.45189 ^c
Be	-3.6433 ^b	-3.6110	-3.64050	-3.66684 ^c
Ne	-12.855 ^a	-12.8184	-12.8509	-12.89370 ^c

^a See reference [27] ^b See reference [28] ^c See reference [29]

Table 2.1: All energies in Hartrees per electron. Comparison of HF and different DFT methods, compared to very accurate CI calculations. The LDA performs poorly compared to HF which gives an accurate description of exchange. However, the superior KLI approximation, an optimised effective potential that is formally self-interaction free for a two-electron system improves the DFT result giving a similar energy to HF.

For isolated atoms DFT-LDA is not as good for total energies as HF due to HF's account of exchange. However the KLI method shows improvement over the LDA, see Table 2.1⁵.

Due to the ground-state nature of DFT, it is not technically correct to take the Kohn-Sham eigenvalues as single-particle energies. However, this is frequently done for the calculation of band structures. DFT overestimates the bandwidth of metals by as much as 30 % for Ni and underestimates the bandgap of semiconductors, by as much as 100 %. The true V_{xc} should contain a discontinuity when an electron is added, as shown by Perdew and Levy and Schlüter and Sham [30, 31]. Later, Godby, Schlüter and Sham [32, 33, 34] were able to show that the absence of a discontinuity is not a failing of the LDA but of the *exact* local V_{xc} and is due to the non-local nature of the true exchange-correlation potential. However, this debate still remains controversial.

2.7 Computational Methods

We now have all the theory necessary to write a DFT computer program. This section details some of the more technical aspects of a practical DFT scheme. Throughout this thesis we have, unless otherwise stated, used the CASTEP [35] package for DFT calculations. The methods below refer specifically to CASTEP, but similar

⁵The DFT results were calculated by the author using the SPDF code, a spherical real-space basis set DFT code developed by P. Rinke and K. T. Delaney, University of York.

considerations arise for any electronic structure code.

2.7.1 Planewaves and Pseudopotentials

One-electron orbitals are represented in a computer by a weighted combination of functions, known as a *basis set*. There are many different ways to do this. A common method, especially in quantum chemistry, is to use atomic orbitals centred on ions. This exploits the fact that the orbitals in molecules and solids still have a large isolated-atom character.

We choose a different approach: *planewaves*. Planewaves are eigenfunctions of momentum. In reciprocal space the kinetic energy matrix is diagonal as a result. It is also easy to increase systematically the quality of basis set, by adding higher frequency planewaves. The accuracy of planewave methods is discussed in Sect. 2.7.3.

Planewaves are not without their associated problems. Near a nucleus the Coulomb potential increases quickly, causing a rapid change in the orbital near the nucleus. Many high frequency planewaves are therefore needed to accurately describe the orbital. However, the electrons in the lower energy states are fortunately not that important to the way atoms bond together. Hence we can divide the electrons into two sets, the *core* electrons and the *valence* electrons. The core electrons are in filled shells. Their behaviour plays little part in the way atoms interact although their charge is important. The valence electrons must be described accurately as their dynamics *are* important to bonding.

We write a new Hamiltonian for the valence electrons only, which contains a *pseudopotential* which the valence electrons experience. We incorporate the core electrons into this potential. The core electron's effect on the valence electrons is described by the pseudopotential but they are no longer described quantum mechanically. Hence if we wished to describe silicon with a pseudopotential we would begin with the all-electron orbitals, $1s^2 2s^2 2p^6 3s^2 3p^2$, and, for instance, place all of the low energy orbitals into the pseudopotential, leaving the $3s^2 3p^2$ electrons to be described by the pseudo-Hamiltonian. We have reduced the number of electrons in our calculation from 14 to 4. As long as the pseudopotential can accurately describe

the effect of the $1s^2 2s^2 2p^6$ electrons on the $3s^2 3p^2$ electrons, the properties of the system should remain unchanged.

A Norm-conserving pseudopotential must cause the eigenvalues of the pseudo-Hamiltonian to be the same as in the all-electron case. It must also cause the pseudo-orbitals to look the same as the all-electron orbitals outside of some pre-defined cut-off region. The pseudopotential is chosen separately for each angular momentum channel which forces the pseudopotential to be non-local. However the advantage is great: this pseudopotential is much weaker than the bare Coulomb potential, hence far fewer planewaves are required to describe the orbitals within the *core region*. The pseudo-orbital looks smoother within the core region but the same as the all-electron wavefunction outside of it.

Much softer pseudopotentials may be formed if the norm-conservation requirement is relaxed. An ultrasoft pseudo-wavefunction[36] that does not conserve charge in the core region may be described with far fewer planewaves. The charge deficit is described by an augmentation charge non-zero within the core region, which is represented on CASTEP's *fine-grid*.

The planewave-pseudopotential approach works well for energy differences and structure determination. However, the Hamiltonian has been substituted by a *pseudo*-Hamiltonian hence the absolute total energy is different from the all-electron value.

2.7.2 Convergence

In any numerical method there are a number of parameters that control the level of the approximations made within the calculation. These must be altered in a consistent way so that the total accuracy of the calculation increases, which inevitably increases the cost of the calculation. Once the answer is obtained to the required accuracy, we say that the calculation is *converged*.

Planewave DFT contains three major controllable approximations. Namely, the quality of the basis set, the quality of the wavefunction representation on a finite integration grid and the quality of the Brillouin-zone (BZ) integration. We must

decide what level of accuracy we require in conjunction with the level of accuracy we can afford. Note that we are talking about the computational accuracy of our calculation compared to the *true* DFT result — not compared to the true experimental result. Each parameter should be converged to the same level of accuracy; it makes little sense to spend all of the effort getting an excellent BZ integration, if the wavefunction concerned is described poorly by the basis set. It is also true though, that if something is computationally cheap, it may as well be converged very accurately so as to leave the errors only from the expensive parameters.

It is also important for the convergence to be “reasonable”. For example, there is no merit in converging a total energy to high precision when the energy *difference* between two systems is required. If we are primarily seeking the lowest energy structures, the results need only be converged to a level to show which candidate structure is favourable, they need not give the *exact* DFT result for the total energy of each structure.

We carry out the following tests for the hydrogen / silicon project, described in detail in Chapter 8, taking a *typical* calculation as a benchmark for the project. The benchmark is the energy difference between a system containing two bond-centred H atoms in a crystal of Si, and another system containing a H₂ molecule in the silicon crystal. We take three simulation cells: bulk Si with 256 atoms: bulk Si with 256 atoms and a bond-centred H: and bulk Si with 256 atoms and a H₂ molecule present at an interstitial site. The energy difference is defined as,

$$\Delta E = E(256 \text{ Si}) + E(256 \text{ Si} + \text{H}_2) - 2E(256 \text{ Si} + \text{H}_{\text{bc}}). \quad (2.26)$$

These calculations are representative of those used in the study as they contain the same species of atoms, the same pseudopotentials and the same size system and bulk lattice geometry. They contain all of the bond types that can form: H–H, Si–Si and Si–H.

Suppose we decide that we would like ΔE to be converged to within 0.04 eV of the exact DFT-GGA result, which is often regarded as chemical accuracy⁶. It is

⁶“chemical accuracy” is normally defined as 1 kcal mol⁻¹ = 0.04336 eV.

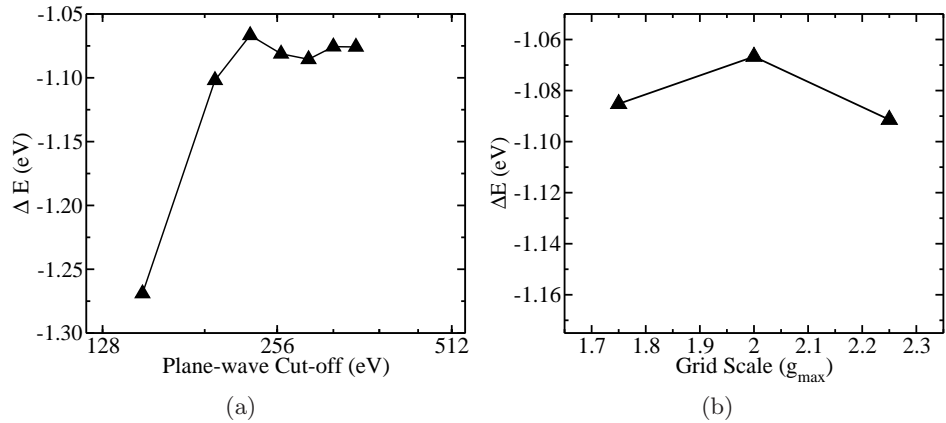


Figure 2.1: (a) Convergence of ΔE (defined in Eqn. 2.26) with respect to planewave cut-off — We see that above about 230 eV the calculation is converged to our required tolerance of 0.04 eV. (b) Convergence with respect to Fourier transform grid - The grid scale is the extent of the FT grid, in units of the largest Fourier component in the basis set, g_{\max} . We see that all values of the grid scale are well within our desired tolerance. However the change in ΔE is actually caused by the fine-grid explained in Sect. 2.7.4, see Fig. 2.3.

attainable in DFT and is a good enough level of accuracy to be able to distinguish between ground state and meta-stable structures.

2.7.3 The Accuracy of Basis Sets

The choice of pseudopotential affects the size of the basis set needed for a calculation. The softer the pseudopotential the fewer high frequency planewaves are needed to accurately describe the orbitals. The orbital basis set is defined by the kinetic energy, $E_{\text{PW}} = p^2/2$, of the most energetic free-electron orbital contained within the basis set.

We increase E_{PW} until the calculated ΔE remains constant to within the required tolerance. See Fig. 2.1(a), where $\ln(E_{\text{PW}})$ is plotted against ΔE . We see that the energy difference is converged above $E_{\text{PW}} = 230$ eV.

2.7.4 Wavefunction Manipulation

E_{PW} defines the highest frequency Fourier component, g_{\max} , that is contained in the planewave expansion of the orbital, $u(\mathbf{r})$.

In order to understand the possible problems with Fourier transforming the finite representation of the wavefunction, we must first consider what happens when a discretely sampled function is Fourier transformed. We know that a continuous periodic function $f(x)$ (such as the wavefunction) with a period $2\pi/a$ Fourier transforms to discrete function $F(x')$ consisting of delta-functions separated by a . However, if we only sample, as we must with a computer, our continuous periodic function $f(x)$ with points $2\pi/ab$ apart (where $b > 1$) and then Fourier transform, we obtain the same function $F(x')$ as before, but repeated at intervals of ab . Each repeat is called an image. These images will overlap if the highest Fourier component of $f(x) > ab/2$, an artifact known as *aliasing*.

The wavefunction $u(\mathbf{r})$ may be expressed on a real-space grid with no loss of information when Fourier transformed as long as the reciprocal-space grid's maximum value, γ_{\max} (in units of g_{\max}), is large enough. The default value is set to $\gamma_{\max} = 1.75$ within CASTEP. This is a controversial issue. Some would argue that since the density, ρ , equals uu^* , we should expect it to have Fourier components up to $2g_{\max}$. Since V_{xc} is a function of the density and may have an infinite number of Fourier components, it is unclear why we should attempt to treat the density exactly, but a function of the density in an approximate way. In Fig. 2.2, we show that whilst reducing the FT grid from $\gamma = 2.00$ to $\gamma = 1.75$ reduces the FT grid and hence the computational effort by $\sim 33\%$, only 6.7% of the volume of the sphere is lost. Since we do not know the Fourier components of V_{xc} , the only sensible way to proceed is to increase γ_{\max} until the total energy has converged.

From Fig. 2.1 (b) we see that, as expected, there is little change in the total energy after $1.75g_{\max}$. This tells us that both the grid and the basis set are large enough to eliminate noticeable aliasing. The slight change that is noticeable is not caused by increasing the grid scale at all, but is actually a consequence of changing the *fine-grid*; as explained below.

An added complication when using ultra-soft pseudopotentials (USPP) is CASTEP's *fine-grid*. When using USPPs the augmentation charge within the core region also needs Fourier transforming. As the charge is closer to the nucleus, it is likely that it contains higher frequency components than the rest of the wavefunction, hence a

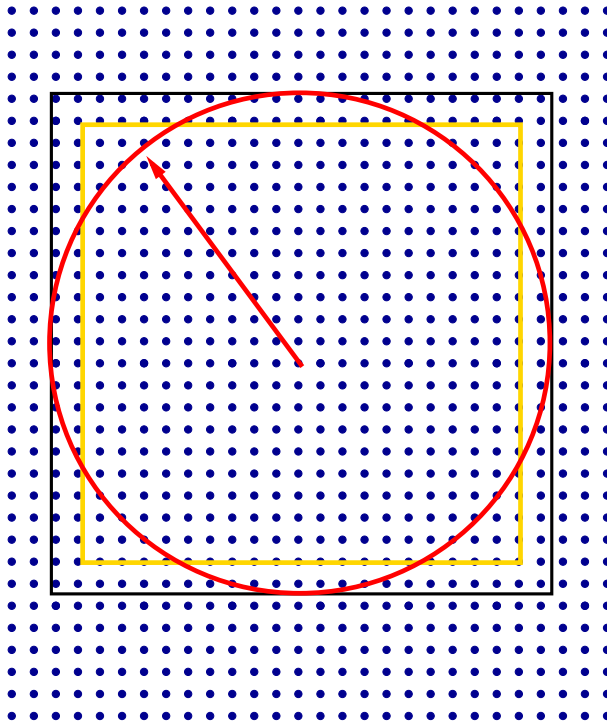


Figure 2.2: Fourier Transform Grid Sizes. Each blue dot represents a frequency component of the density. The red circle has a diameter of $2g_{\max}$ hence the black FT box, with a width of $2 \times 2g_{\max}$ completely encompasses it. However, the gold box, with a width of $2 \times 1.75g_{\max}$ does not include some of the higher frequencies. From the diagram it is clear that the reduction in FT box size from black to gold only omits a few frequencies in two dimensions and this will be a smaller fraction in three dimensions. I calculate that whilst the volume of the FT box is reduced by some 33% by changing from the black to the gold boxes in 3D, the volume of the red sphere truncated in the reduction, (*i.e.* the number of Fourier components omitted) is only 6.7%.

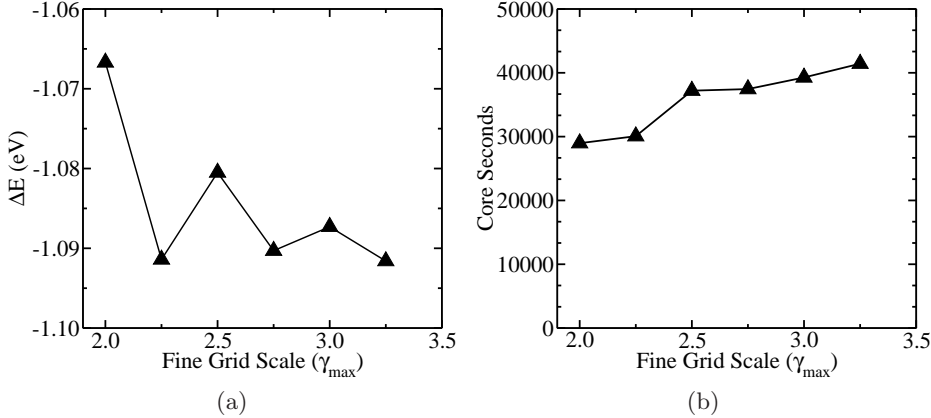


Figure 2.3: Fourier Transform Fine Grid convergence — (a) The Fine-Grid convergence. All values are within tolerance although $\gamma_{\max} \geq 2.75$ means that the computational error will be dominated by other terms. (b) A demonstration of the computing power necessary to converge the fine grid, showing the total time to obtain the ground-state energy of a 256 atom simulation cell, on a 3.00 GHz “Woodcrest” processor. This illustrates that large fine-grid scale calculations cost only marginally more than small ones. The step between 2.25 and 2.50 is caused by increasing the number of computer processors used in the calculation from 16 to 32 and the imperfect parallel scaling of CASTEP that results.

finer grid is required. This grid is not used for the whole calculation for reasons of economy. Above, the fine-grid maximum was set equal to γ_{\max} . Now, we take the converged $\gamma_{\max} = 2$ and increase the fine-grid density. It can be seen in Fig. 2.3 (a) that all values of the fine-grid parameter γ_{\max} are within our acceptable tolerance, but that above $\gamma_{\max} = 2.75$ the error is negligible. As increasing the fine-grid scale costs little extra computational effort, see Fig. 2.3 (b), we use $\gamma_{\max} = 2.75$ and eliminate the error altogether. We note that the increase in calculation time between $\gamma_{\max} = 2.25$ and 2.50 is not caused by the fine-grid being increased but is a consequence of imperfect parallel scaling when changing the number of processors from 16 to 32. This is due to the increased communication between processors. The memory usage increases with grid-size in the same way as the calculation time.

2.7.5 Brillouin Zone Sampling Scheme

The quantum number \mathbf{k} describes the crystal momentum of the electron in periodic system. The relation between \mathbf{k} and the energy E gives rise to the *band structure*.

As the crystal is periodic we use Bloch's theorem to map all k-points into ones within the first Brillouin zone (1BZ). All other k-points are just repeats of this. However, in order to evaluate the total energy of the crystal we must integrate over all \mathbf{k} in the 1BZ. As \mathbf{k} is a continuous quantum number we require a method of evaluating this integration computationally.

The importance of performing accurate Brillouin zone integrations when calculating defect formation energies has been emphasised by, among others, Shim *et al.* [37]. Therefore studying BZ integration is very important to the second part of this dissertation. DFT calculations by Gharaibeh *et al.* [38] explored the convergence of BZ sampling for self-interstitial-hydrogen complexes in silicon.

Throughout this dissertation, instead of standard Monkhorst-Pack (MP) sampling [39] we use the multi-k-point generalisation of the Baldereschi mean-value point scheme [40] outlined by Rajagopal *et al.* [41, 42].

Three linearly-independent reciprocal lattice vectors ($\mathbf{b}_1, \mathbf{b}_2, \mathbf{b}_3$) are chosen, which need not be primitive, and a $l \times m \times n$ grid of k-points is defined by

$$\mathbf{k}_{ijk} = \frac{i\mathbf{b}_1}{l} + \frac{j\mathbf{b}_2}{m} + \frac{k\mathbf{b}_3}{n} + \mathbf{k}_B(l, m, n), \quad (2.27)$$

where

$$i = 0, 1, \dots, l - 1; \quad (2.28)$$

$$j = 0, 1, \dots, m - 1; \quad (2.29)$$

$$k = 0, 1, \dots, n - 1. \quad (2.30)$$

It is clear from the mean value theorem that there is at least one point within the 1BZ which gives the average value of the band energy over the 1BZ. Baldereschi [40] showed this point for certain crystal geometries. He defined the *first-failure star*, which is the lowest frequency set of reciprocal lattice vectors that are not perfectly integrated in the 1BZ. He then found the point in the BZ which (a), maximised the frequency of the first-failure star and (b), minimised this first-failure star's error.

The standard Baldereschi mean-value point can be written in terms of the \mathbf{b}_i

$$\mathbf{k}_B = \alpha_1 \mathbf{b}_1 + \alpha_2 \mathbf{b}_2 + \alpha_3 \mathbf{b}_3, \quad (2.31)$$

which defines the α_i , and the offset $\mathbf{k}_B(l, m, n)$ for the multi-k-point scheme [41, 42] is

$$\mathbf{k}_B(l, m, n) = \frac{\alpha_1 \mathbf{b}_1}{l} + \frac{\alpha_2 \mathbf{b}_2}{m} + \frac{\alpha_3 \mathbf{b}_3}{n}. \quad (2.32)$$

This is the natural multi-k-point generalisation of Baldereschi's scheme. It corresponds to sampling the Baldereschi mean-value point of the super-cell obtained by choosing direct (real-space) lattice vectors $(l\mathbf{a}_1, m\mathbf{a}_2, n\mathbf{a}_3)$, where the \mathbf{a}_i are related to the \mathbf{b}_i by the standard dual transformation. We will refer to this as the Multi-B scheme.

We can think of this generalisation as follows. If the Baldereschi point is the *best* single k -point to use in the simulation cell, then a $2 \times 2 \times 2$ supercell with 8-times the volume, also has a (different) Baldereschi point which is its best single k -point. Since by translation, one point in $2 \times 2 \times 2$ supercell corresponds to 8 points in the original simulation cell, we can obtain the 16-atom silicon simulation cell result by calculating 8 k -points in the 2-atom cell. This is, of course, more efficient since DFT scales as N^3 , so that a 1 k -point 16-atom calculation takes $8^3 = 512$ times as long as a 2-atom calculation, whereas 8 k -point calculations of 2-atoms only takes 8 times as long. Hence by translation the Baldereschi point of the $n \times n \times n$ supercell into the original M -atom simulation cell, we can obtain the best $M \times n \times n \times n$ -atom result (*i.e* at the Baldereschi point) with only an n^3 increase in cost over the M -atom result.

In Fig. 2.4 a comparison for bulk silicon of standard $n \times n \times n$ Monkhorst-Pack grids, the same grids but centred on $\mathbf{k}=0$ (Multi- Γ), and the Multi-B scheme is reported. For odd values of n the MP and Multi- Γ grids are the same, although we could, of course, introduce an appropriate shift of the MP grid for odd n which gives smooth convergence. The MP scheme gives smaller errors than the Multi- Γ scheme for even n . The Multi-B energies converge smoothly with n and give the smallest

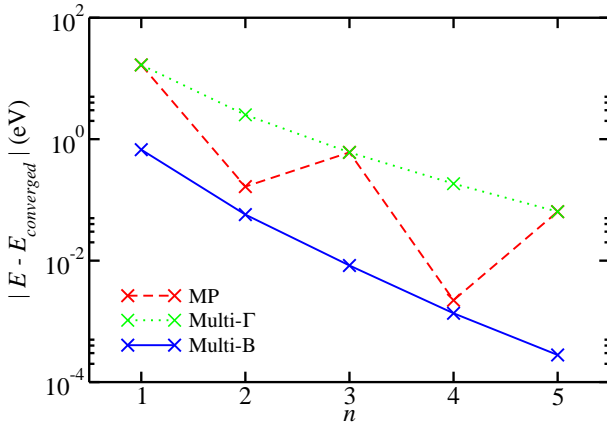


Figure 2.4: Magnitudes of the energy differences between the converged energy (taken from a Multi-B calculation with $n = 20$) and energies obtained with different k-point grids for a 2-atom cell of diamond-structure silicon. The energies are in eV per cell and the number of points in each grid is n^3 .

errors for each value of n .

The cost of a BZ integration is determined not by n but by the number of symmetry inequivalent k-points in the grid and the most efficient k-point grid generally depends on the symmetry of the structure. Symmetric structures normally have more inequivalent k-points in the Multi-B grid than in the corresponding MP grid. During the random structure searches (see Part II), symmetry is not imposed and all n^3 grid points are used, and therefore the Multi-B scheme is the most efficient.

Part I

Random Wavefunction Sampling

Chapter 3

Sampling the Wavefunction with Random Numbers

3.1 Introduction to Quantum Monte Carlo

THE METHODS DISCUSSED so far have involved approximating the many-body wavefunction as a product of single-particle orbitals. In QMC we calculate expectation values of operators, \hat{O} , acting on a many-body wavefunction, $\Psi(\mathbf{R})$. This involves integrating $\Psi^*(\mathbf{R})\hat{O}\Psi(\mathbf{R})$ over all space, although we do this stochastically.

Let us take the naïve approach and use normal quadrature to perform the integration. The trapezium rule is rather simplistic, so we choose the next order of approximation, *Simpson's rule*¹. The error in a Simpson's rule integration scales as $1/N^{4/d}$, where N is the number of grid points and d is the dimension of the integral (*i.e.*, to halve the uncertainty in a calculation in 2-dimensions, we require $\sqrt{2}N$ grid-points). For a system of 10 quantum particles, for instance, the wavefunction is 30-dimensional. Hence to halve the uncertainty we must increase the number of grid-points 180-fold².

The advantage of Monte Carlo (MC) integration is that the error always decreases as $1/\sqrt{N}$ where N is the number of sample points, regardless of the dimen-

¹Where the function is interpolated quadratically.

²That is, $\frac{\text{Error}}{2} = \frac{1}{2N^{30}} = \frac{1}{N'^{30}} \implies N' \approx 180N$.

sionality of the integral. Therefore, for any problem of more than 8-dimensions, (hence in 3-D, three or more electrons) MC integration is clearly more suitable.

Standard fermion QMC also scales well with system size: the computational effort scales as $\mathcal{O}(N^3)$, where N is the number of particles. This is not quite as favourable as DFT which scales as $\mathcal{O}(N^3)$ ³ with a much smaller pre-factor but much more so than the quantum chemistry methods such as second-order Møller-Plesset(MP2) $\mathcal{O}(N^5)$ and coupled cluster methods. (CCSD(T)) scales as $\mathcal{O}(N^7)$. QMC can be much more accurate than DFT since the approximating of exchange-correlation functionals is not required.

By far the most famous application of QMC, as mentioned earlier, is Ceperley and Alder's [23] treatment of the HEG and its application to the LDA exchange-correlation potential. QMC has been applied to HEG slabs [44, 45] and spheres [46], liquid helium-3 [47] and has also been applied to model bosonic systems [48].

Real systems are also calculable in QMC, for example, transition metal oxides [49], Bose gases [50], Li and H₂O clusters [51] and dimers [52]. For further discussion see the review article by Foulkes *et al.*[53].

3.2 Monte Carlo Method

We begin with an explanation of the MC integration of a function, $f(x)$, between two limits, $a \leq x \leq b$.

Pick N random numbers from a uniform distribution, r_n , where $a \leq r_n \leq b$ and evaluate $f(r_n)$. The average of $f(r_n)$,

$$\frac{1}{N} \sum_{n=1}^{n=N} f(r_n), \quad (3.1)$$

is an estimate of the average of $f(x)$ over the range a to b . Therefore as $N \rightarrow \infty$

³ $\mathcal{O}(N)$ -scaling DFT methods are also available, but are not used in this thesis [6, 43].

the value of the sum is,

$$\frac{b-a}{N} \sum_{n=1}^{n=N} f(r_n) \rightarrow \int_a^b f(x) dx. \quad (3.2)$$

For example, imagine that we wish to find the average score of a particular archer in the archery club. We define two functions:

- The probability density function (PDF) of the arrow landing at a particular point on the target. This should be approximately a Gaussian function centred on the gold disk at the centre of the target. We define this as $w(x)$ and model the target as 1-dimensional, $-\infty < x < \infty$, where $x = 0$ is at the centre of the target, as shown in Fig. 3.1.
- The score function $s(x)$, where the score is greater nearer the centre of the target.⁴

The probability of an arrow landing at a particular point on the target is $w(x)$, which is the probability of getting the score, $s(x)$. If arrow landing positions, x , are randomly sampled from a uniform distribution, the average score can be obtained by MC integration of the composite function $f(x) = w(x)s(x)$ as in Eqn. 3.2.

This leads us to *importance sampling*. For a competent archer, large values of x (*i.e.* really poor shots) form a very small amount of the average. If the PDF of the arrow landing on the target, $w(x)$, is known, a set of n random numbers, $\{r_w\}$, are generated to the distribution, $w(x)$. The target function, s , is then sampled with the random numbers, just as the archer does with the arrows. Hence the average score, is again just the average of $\{s(r_w)\}$. In the large N limit,

$$I = \frac{\int w(x)s(x) dx}{\int w(x) dx} = \frac{b-a}{N} \sum_{n=1}^{n=N} s(r_{w,n}), \quad (3.3)$$

where the n^{th} , random number is $r_{w,n}$ and the $\{r_w\}$ are distributed according to

⁴On a normal target the score is divided into concentric discs, however let us assume that the number of discs tends to infinity in this case.

$\frac{w(x)}{\int_a^b w(x) dx}$, and the variance is,

$$\sigma_I^2 = \frac{\sum_{n=1}^N [s(r_w, n) - I]^2}{N(N-1)}. \quad (3.4)$$

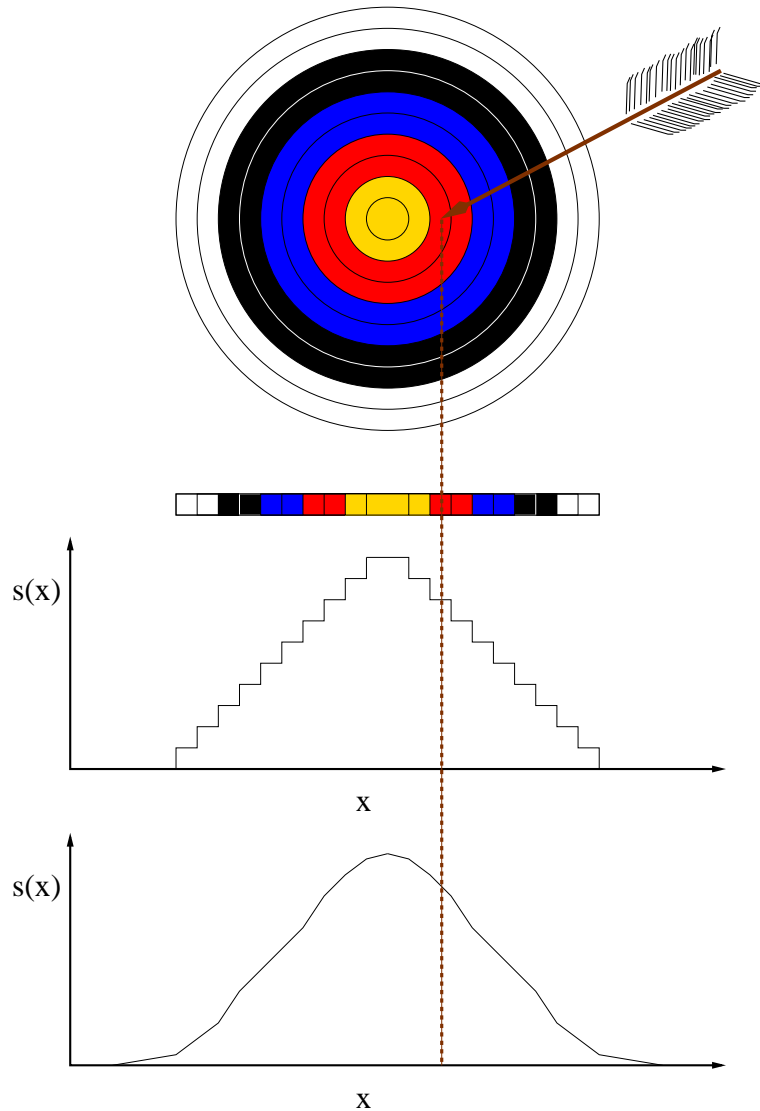


Figure 3.1: Archery Analogy – An archery target is shown with a 1-dimensional representation of the target shown below it. The scores, $s(x)$, corresponding to this 1-D representation are plotted in the graph below it. The final graph shows a continuous function version of the score. The brown dotted line shows the score, $s(x)$, on the graphs that the arrow on the target obtains.

3.3 Variational Monte Carlo

Variational Monte Carlo (VMC) is used to find an estimate of the true ground-state energy of a system of interacting particles. Let us pick some normalisable wavefunction $\Psi(\mathbf{R})$ where \mathbf{R} is the set of the positions of the N electrons in the system, $\mathbf{r}_1, \mathbf{r}_2, \dots, \mathbf{r}_N$. A particular \mathbf{R} is called a *configuration* of the system⁵. The total electronic energy is given by

$$E_{\text{VMC}} = \frac{\int \Psi^*(\mathbf{R}) \hat{H} \Psi(\mathbf{R}) d\mathbf{R}}{\int \Psi^*(\mathbf{R}) \Psi(\mathbf{R}) d\mathbf{R}}. \quad (3.5)$$

We may now reduce the noise in the integration just as we did in the archery case. We define the *local energy*, $E_L(\mathbf{R}) = \Psi^{-1}(\mathbf{R}) \hat{H} \Psi(\mathbf{R})$, of configuration, \mathbf{R} , and rewrite the above integral as

$$E_{\text{VMC}} = \frac{\int |\Psi(\mathbf{R})|^2 E_L(\mathbf{R}) d\mathbf{R}}{\int |\Psi(\mathbf{R})|^2 d\mathbf{R}}. \quad (3.6)$$

This is now of the form of Eqn. 3.3, so the integration can be performed by randomly selecting configurations from the distribution $\frac{|\Psi(\mathbf{R})|^2}{\int |\Psi(\mathbf{R})|^2 d\mathbf{R}}$ and averaging the resulting $E_L(\mathbf{R})$.

Generating configurations distributed according to $|\Psi(\mathbf{R})|^2$ is performed by the Metropolis Algorithm[54]. A trial move $\mathbf{R}_n \rightarrow \mathbf{R}'_n$ is proposed and the value

$$\gamma = \frac{|\Psi(\mathbf{R}')|^2}{|\Psi(\mathbf{R})|^2}, \quad (3.7)$$

is calculated. A random number, r , where $0 \leq r \leq 1$ is chosen and if $\gamma > r$ the move $\mathbf{R}_n \rightarrow \mathbf{R}'_n$ is accepted, *i.e.*, $\mathbf{R}_{n+1} = \mathbf{R}'_n$ otherwise it is rejected, $\mathbf{R}_{n+1} = \mathbf{R}_n$. Note that if \mathbf{R}_n causes the configuration to move to a region of higher probability, $\gamma > 1$ and the move is always accepted.

As always, when using the Metropolis algorithm a period of equilibration is necessary. The configurations must be allowed to reach dynamic equilibrium whereby they will be distributed according to $|\Psi(\mathbf{R})|^2$. Only once this equilibrium is reached may the MC integration begin.

⁵For reasons that will become clearer later, it is also known as a *walker*.

The Metropolis Algorithm produces correlated results, $(\Psi(\mathbf{R}_n))$ is inevitably similar to $(\Psi(\mathbf{R}_{n+1}))$. In general we use the *electron-by-electron* algorithm, where only one electron is moved at each step. This of course increases the correlation between steps compared to moving an entire configuration at once, but it is still advantageous as it greatly increases the chance of the move being accepted. The correlations are dealt with by averaging over successive steps or sampling every t steps, where t is greater than the correlation length. The length of the trial step between \mathbf{r}_n and \mathbf{r}_{n+1} is set so that the chance of accepting a move is $\sim 50\%$. This has been shown by López Ríos [55], in many circumstances, to sample a large volume of configuration space in a short time.

Since the local energies, E_L , are correlated, their variance, $\sigma_{E_L}^2$, will be an underestimate of the true error in E_{VMC} . An estimate of the true variance of E_L may be obtained by *re-blocking* the data. If we have M timesteps we divide these data into blocks of length $B_b = 2^b$, where b is the reblocking-transformation number. Hence we have $N_b = M/B_b$ blocks, where B_b need not be an integer as the last block may be incomplete. We average the local energy E_L in each block obtaining E_b and the variance of this, σ_b^2 . As the block length, B_b , increases, the re-blocked energies, E_b become uncorrelated. The reblocking-transformation number, b , is plotted against the standard error, $\sigma_b/\sqrt{N_b}$, in Fig. 3.2. This shows a plateau in the standard error at $b = 7$, when the block size is large enough to de-correlate the re-blocked energies, E_b . The plateau value of the standard error is taken as an estimate of the standard error of E_L . Note that the re-blocking of the energies does not alter the mean value. Hence, $\overline{E_b} = E_{VMC}$ for every value of b .

VMC plus the variational principle gives a prescription for finding an approximation to the ground-state wavefunction. Choose some trial wavefunction Φ_T and use Monte Carlo integration to find, E : then take a new trial wavefunction Φ'_T which, if $E' < E$, will be a better approximation to the true ground-state wavefunction, ϕ_0 . The next section discusses how to form a good trial wavefunction that can be varied to find the lowest E_{VMC} .

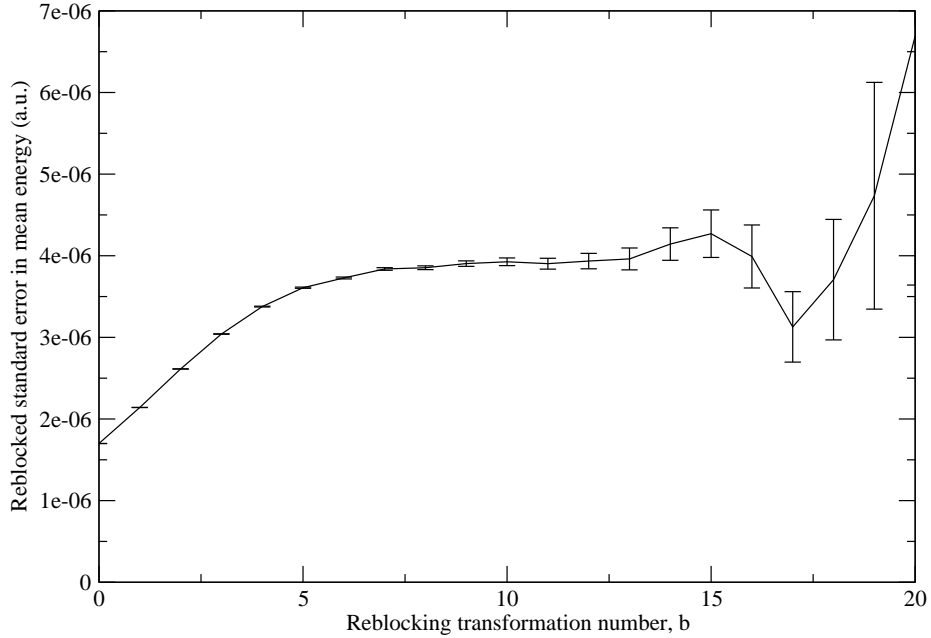


Figure 3.2: Reblocking plot for a sample VMC run. As the reblocking-transformation number, b , increases, so does the standard error in the mean, until $b = 7$, where the standard error plateaus. At this point each block is large enough to be uncorrelated from its neighbours and the standard error of the energy of each block is an estimate of the standard error in the calculation. For large values of the reblocking-transformation number $b > 15$, the standard error in the standard error increases due to the small number of large blocks.

3.3.1 Trial Wavefunction

Choosing a trial wavefunction is the most important part of the QMC algorithm. When dealing with electrons or, as shall be done later, fermionic atoms, a wavefunction in the form of a determinant is used so as to impose antisymmetry with respect to an interchange of particle coordinates. Usually a pair of Slater determinants is used but in the case of fermionic atoms a pairing function is used, which is a single Slater determinant, see Appendix B. It can be shown, (see Appendix A), that for a spin-independent operator, such as the Hamiltonian used in Chapter 4, if Ψ is a Slater determinant then the expectation value $\langle \Psi | \hat{H} | \Psi \rangle$ can be written as, $\langle D_{\uparrow} D_{\downarrow} | \hat{H} | D_{\uparrow} D_{\downarrow} \rangle$ which is a product of two determinants: one containing the up-spin particles and one the down-spin particles. This effectively treats up-spin and down-spin particles as distinguishable. The expectation value of the energy

may then be obtained with this product of Slater determinants, $D_\uparrow D_\downarrow$, using the VMC method. However, since we have not included correlation we should expect to obtain the HF energy.

3.3.2 The Jastrow Factor

The Jastrow factor, e^J , modifies the Slater wavefunction in the following way,

$$\Psi_{\text{SJ}} = e^J \Psi_S[\mathbf{R}] = e^J D_\uparrow D_\downarrow, \quad (3.8)$$

where D_\uparrow and D_\downarrow are the up- and down-spin determinants respectively.

The Jastrow factor is a function of the electronic positions and so adds *correlation* into the trial wavefunction. To achieve the flexibility necessary the Jastrow factor contains many optimisable parameters.

As two charged particles approach each other the Coulomb potential diverges. The *cusp conditions* [56, 57] are imposed using the Jastrow factor to force the local energy to be finite at the coalescence point. The cusp conditions must be obeyed by the exact wavefunction.

The Jastrow factor is an exponential function and therefore it is always a positive multiplier of the Slater determinant. Therefore it does not change the nodal surface of the wavefunction.

3.3.3 Backflow

In order to create a more accurate trial wavefunction it is desirable to include correlation such that when one particle is moved, all particles respond by altering their positions. Hence *collective co-ordinates*⁶, \mathbf{x}_i , are formed for electron, i , [55, 58] where

$$\mathbf{x}_i = \mathbf{r}_i + \zeta_i(\mathbf{R}), \quad (3.9)$$

and \mathbf{r}_i is the position of particle i and ζ_i is some parameterised function of the particle positions, \mathbf{R} . This makes a wavefunction of the Slater-Jastrow-Backflow

⁶Or *quasiparticle coordinates*.

form,

$$\Psi_{\text{SJB}} = e^J \Psi_S[\mathbf{X}(\mathbf{R})]. \quad (3.10)$$

The backflow function ζ is then subdivided, in a similar way to the Jastrow factor, into electron-electron and electron-ion terms. It is then simple to optimise the parameters in the backflow function, ζ , using the optimisation techniques discussed in the next section.

Backflow was first proposed by Feynman and Cohen [59] for a ${}^3\text{He}$ impurity in liquid ${}^4\text{He}$. It was first used in QMC by Lee *et al.* [60] for modelling ${}^3\text{He}$ in a diffusion Monte Carlo (DMC) calculation. Inhomogeneous backflow was first used by López Ríos [58]. It has also been applied to model systems of Fermi fluids [61] and the 2- and 3-dimensional electron gases [62, 63] and has also been applied to metallic hydrogen [64, 65].

${}^3\text{He}$ has been extensively studied using backflow [66] and is still a good system for testing backflow: Holzmann *et al.* [67] have tried 4-body correlations in their backflow function which further improved the results.

3.3.4 Wavefunction Optimisation

I have presented how to parameterise a wavefunction that is able to describe correlation. These parameters must now be varied so as to minimise the energy. These parameters are represented by the vector, \mathbf{a} . To that end, a cost-function to minimise must be chosen. An obvious choice for this function is the VMC energy, however this has been out of reach until very recently due to numerical instabilities. Energy minimisation has probably been the most important algorithmic development in the past couple of years [68, 69]. This method was tried in the subsequent chapter, but tended to be unstable for the wavefunctions chosen in this project. For this reason we reverted to the tried and tested variance minimisation method, which is very stable. However the implementation on CASINO has since been greatly improved by López Ríos and Trail⁷.

When the trial wavefunction is an eigenfunction of the Hamiltonian, the variance

⁷Unpublished

of the local energy E_L is zero. The variance can be used as a measure of how close the trial wavefunction is to an eigenstate. Hence we can use the variance of the local energies as the cost function. This has the advantage of having a definite lower bound of zero, although there is no guarantee that the minimum of the energy and variance coincide.

In order to reduce the statistical noise in the difference between successive steps, the same equilibrated configurations are used for each step in the minimisation. New configurations are generated from time to time as the wavefunction is optimised. This method is called *correlated sampling*. Hence the entire minimisation procedure uses, $|\psi(\mathbf{a}_0)|^2$, where \mathbf{a}_n is the set of parameters found in the n^{th} minimisation step. The cost function is,

$$\sigma^2(\mathbf{a}_n) = \frac{\int |\psi(\mathbf{a}_0)|^2 \frac{|\psi(\mathbf{a}_n)|^2}{|\psi(\mathbf{a}_0)|^2} [E_{\text{VMC}}(\mathbf{a}_n) - E_L(\mathbf{a})]^2 d\mathbf{R}}{\int |\psi(\mathbf{a}_0)|^2 \frac{|\psi(\mathbf{a}_n)|^2}{|\psi(\mathbf{a}_0)|^2} d\mathbf{R}}, \quad (3.11)$$

where we call $\frac{|\psi(\mathbf{a}_n)|^2}{|\psi(\mathbf{a}_0)|^2}$ the *weighting function*, $w(\mathbf{a}_0, \mathbf{a}_n)$.

However, this *re-weighted* variance minimisation procedure is also quite unstable, a few, or sometimes only one of the $w(\mathbf{a}_0, \mathbf{a}_n)$ can become very large. In effect, too much freedom is being given to the minimiser: the minimiser is able to not only change the function $\psi(\mathbf{a})$ through the parameters, \mathbf{a} , but also to change how much weight is given to each configuration that is sampled, through $w(\mathbf{a}_0, \mathbf{a}_n)$.

There are a number of ways to solve this problem: *limited re-weighting* truncates $w(\mathbf{a}_0, \mathbf{a}_n)$ at some value, so that not all the weight can be given to one configuration. Setting $w(\mathbf{a}_0, \mathbf{a}_n) = 1$ in all cases has proven to be a very stable technique [70]. Although the cost function is no longer the true variance, it has the same minimum, that is eigenstate, if the trial wavefunction is able to describe the true ground state: this is called *un-reweighted* variance minimisation. If the nodal surface is moved through a configuration during optimisation, this normally causes the local energy to diverge. This can be remedied by *filtering* the E_L and removing or giving a smaller weight to any configuration whose local energy is very different from the mean value. Taking the median absolute deviation rather than the variance can also solve this problem and is the method used for optimising the wavefunctions for

ultracold atoms discussed in the next chapter.

3.4 Diffusion Monte Carlo

3.4.1 Trial Wavefunction

DMC is a more accurate method than VMC. A VMC wavefunction is normally used as the initial wavefunction for DMC. In DMC there are no parameters to optimise and the only constraint is the *fixed-node approximation*, which will be discussed later and means that the accuracy of a DMC energy depends only on the accuracy of the nodes of the trial wavefunction. Hence we found it to be important in the ultracold atom project to use backflow, which can change the nodal surface of the trial wavefunction if the nodes are not known exactly. The Jastrow factor, however, is always a positive multiplier of the Slater wavefunction and hence cannot change the nodal surface. The variance of the DMC energy, $\sigma_{E_{\text{DMC}}}^2$, is approximately,

$$\sigma_{E_{\text{DMC}}}^2 \sim \frac{E_{\text{T}} - E}{\tau}, \quad (3.12)$$

where E_{T} is the VMC energy of the initial trial wavefunction, E is the energy of the (unknown) exact wavefunction and τ is the DMC time-step, which we will explain a little later. Hence it is important to have the best E_{T} possible to minimise the variance in the DMC energy and therefore a Jastrow factor is used in trial wavefunctions for DMC calculations.

3.4.2 Overview

Consider the time-dependent Schrödinger equation,

$$\hat{H}\Psi(\mathbf{R}, t) = i\frac{\partial\Psi(\mathbf{R}, t)}{\partial t}, \quad (3.13)$$

whose solution can be expanded in a basis of eigenstates of the Hamiltonian as

$$\Psi(\mathbf{R}, t) = \sum_{n=0}^{\infty} c_n \phi_n(\mathbf{R}) e^{iE_n t}. \quad (3.14)$$

where c_n are constants and $\phi_n(\mathbf{R})$ is the n^{th} eigenfunction with eigenenergy E_n .

If we set $t = i\tau$ and introduce a shift in the energy E_T , which is approximately equal to the ground-state energy, we obtain,

$$\Psi(\mathbf{R}, t) = \sum_{n=0}^{\infty} c_n \phi_n(\mathbf{R}) e^{-(E_n - E_T)t}. \quad (3.15)$$

When this wavefunction is propagated according to the imaginary-time Schrödinger equation, all of the excited states in the sum (*i.e.* $\phi_{n>0}$) decay exponentially. Hence as $\tau \rightarrow \infty$, $\Psi(\mathbf{R}, \tau) \rightarrow \phi_0$ we have a way of extracting the ground-state wavefunction from a trial wavefunction.

We still require a mechanism to propagate this wavefunction in imaginary time and for this we use the Green's function, $G(\mathbf{R}, \mathbf{R}', \delta\tau)$, which tells us that for a starting configuration, \mathbf{R}' and final configuration, \mathbf{R} , the probability of the system moving from \mathbf{R}' to \mathbf{R} , in time $\delta\tau$,

$$\Psi(\mathbf{R}, \tau + \delta\tau) = \int G(\mathbf{R}, \mathbf{R}', \delta\tau) \Psi(\mathbf{R}', \tau) d\mathbf{R}'. \quad (3.16)$$

An approximation to $G(\mathbf{R}, \mathbf{R}', \delta\tau)$ can be obtained by splitting the Schrödinger equation into two parts:

$$\text{a diffusion equation } \frac{1}{2} \nabla^2 \Psi = \frac{\partial \Psi}{\partial \tau}, \quad (3.17)$$

$$\text{a rate equation } -U\Psi = \frac{\partial \Psi}{\partial \tau}, \quad (3.18)$$

which is a good approximation for short times, $\delta\tau$. For both equations the correct form of the Green's function is known, we then form $G(\mathbf{R}, \mathbf{R}', \delta\tau)$ from a product of the drift and diffusion Green's functions, assuming $\delta\tau$ is small. The rate equation and its Green's function are poorly behaved, since they are dependent on the potential energy, U , which will diverge at certain points in space for the Coulomb interaction leading to instabilities.

I have now described how to propagate a many-body wavefunction in imaginary time so as to obtain the ground-state energy. However, the bosonic ground state is lower in energy than the fermionic one, hence the solution propagates to the

bosonic ground state. Even if the trial wavefunction is completely antisymmetric, the stochastic sampling will introduce a small bosonic component which will then grow to dominate the calculation. This problem is known as the *fermion sign problem* and appears in different guises in many different QMC algorithms. In the DMC algorithm described so far it manifests itself in the following way. The diffusion equation describes the wavefunction as a probability distribution. From Eqn 3.16, we see that Ψ is not a probability distribution, it can have negative and positive regions, indeed since the fermionic ground state must be antisymmetric, the wavefunction *must* have a negative part if it describes two or more particles of the same spin. To solve this problem the position of the nodes is fixed at the start of the calculation so that a configuration, \mathbf{R} cannot pass through them. This is the fixed-node approximation. To impose this approximation and to make the rate equation better behaved we use importance sampling.

3.4.3 Importance Sampling

Let us define the function

$$f(\mathbf{R}, \tau) = \Psi(\mathbf{R}, \tau)\Phi(\mathbf{R}), \quad (3.19)$$

and substitute into the Schrödinger equation, giving

$$-\frac{1}{2}\nabla^2 f(\mathbf{R}, \tau) + \nabla \cdot \{\mathbf{V}(\mathbf{R})f(\mathbf{R}, \tau)\} + \{E_L(\mathbf{R}) - E_T\} f(\mathbf{R}, \tau) = -\frac{\partial f(\mathbf{R}, \tau)}{\partial \tau},$$

which is the Fokker-Planck equation for drift and diffusion, with an extra *branching* term. We define the *drift velocity* as in the Fokker-Planck equation, $\mathbf{V}(\mathbf{R}) = \Phi^{-1}(\mathbf{R})\nabla\Phi(\mathbf{R})$. The local energy of the trial wavefunction is defined in the same way as in VMC, $E_L(\mathbf{R}) = \Phi^{-1}(\mathbf{R})\hat{H}\Phi(\mathbf{R})$.

The advantage of this transformation is that the resulting function $f(\mathbf{R}, \tau)$ has its nodes fixed to those of the initial trial wavefunction, $\Phi(\mathbf{R})$, since $f(\mathbf{R}, \tau) \geq 0$ when $\Phi(\mathbf{R}) = 0$, (see Eqn. 3.19). The branching depends on the local energy, $E_L(\mathbf{R})$, which should fluctuate much less than the potential energy, U , since $\Phi(\mathbf{R})$ should already be close to an eigenstate of the Hamiltonian. The integral for the propagation

of $f(\mathbf{R}, \tau)$ is

$$f(\mathbf{R}, \tau + \delta\tau) = \int \tilde{G}(\mathbf{R}, \mathbf{R}', \delta\tau) f(\mathbf{R}', \tau) d\mathbf{R}'. \quad (3.20)$$

We then obtain the two parts of the Green's function, \tilde{G} , the drift and diffusion part G_D and the branching part G_B . Again, assuming that the time-step $\delta\tau$ is small, we can write $G' \approx G_D G_B$ where

$$G_D(\mathbf{R}, \mathbf{R}', \tau) = \frac{1}{(2\pi\tau)^{\frac{3N}{2}}} \exp\left(-\frac{(\mathbf{R} - \mathbf{R}' - \tau\mathbf{V}(\mathbf{R}'))^2}{2\tau}\right) \quad (3.21)$$

is the solution to the Fokker-Planck equation and

$$G_B(\mathbf{R}, \mathbf{R}', \tau) = \exp\left(-\frac{\tau}{2} (E_L(\mathbf{R}) + E_L(\mathbf{R}') - 2E_T)\right). \quad (3.22)$$

is the Green's function associated with the rate equation.

In practice we represent $f(\mathbf{R}, \tau)$ by a set of weighted configurations,

$$f(\mathbf{R}, \tau) = \sum_c^{N_c} w_c(\tau) \delta(\mathbf{R} - \mathbf{R}_c(\tau)) \quad (3.23)$$

where w_c , is the weighting factor for configuration, c . Substituting this into Eqn. 3.20 we obtain

$$f(\mathbf{R}, \tau + \delta\tau) = \sum_c^{N_c} w_c(\tau) G_B(\mathbf{R}, \mathbf{R}_c, \tau) G_D(\mathbf{R}, \mathbf{R}_c, \tau), \quad (3.24)$$

where \mathbf{R}_c is a discrete point in space, known as a configuration. In the next section the implementation of this algorithm is discussed.

3.4.4 Practicalities

Each configuration is moved by allowing it to drift by a distance $\tau\mathbf{V}$ and then diffuse by a random distance distributed normally about 0 with a variance of τ . Once all of the electrons have moved, the branching factor for the configuration is calculated, which determines the number of copies of the configuration which survive into the next timestep. Each configuration sampled will have a corresponding local energy, which is averaged to find the DMC energy. In Fig. 3.3, we show a pictorial representation of configurations drifting, diffusing and branching. It is important to

equilibrate the configurations at the beginning of the run so that the excited-state information is lost from the $f(\mathbf{R}, \tau)$ distribution.

There are a number of problems that arise with this algorithm. The first is *timestep error*. The algorithm only being correct as $\tau \rightarrow 0$ so that the calculation will contain a bias due to τ being finite. Hence τ must be small enough so that the timestep error is small compared to the standard error of the calculation but τ must be large enough so that the configurations sample the configuration space in a reasonable (computational or *real*) time. In practise a number of runs with different τ are normally performed then extrapolated to zero τ . An example of timestep extrapolation is given in Fig. 3.4.

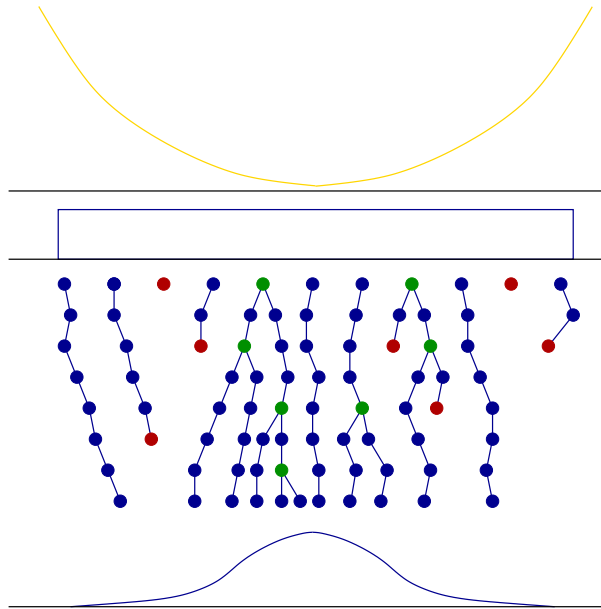


Figure 3.3: Representation of the DMC algorithm. Imaginary time propagates down the page. The potential is shown in gold. The configurations are generated according to the flat distribution shown in blue below the potential. Configurations, shown in blue, green and red then propagate through imaginary time down the page; configurations that die at a timestep are shown in red, configurations that branch are shown in green. After 7 timesteps the walkers are distributed according to the blue wavefunction shown at the bottom of the figure.

Another error is called *population control bias* (PCB). As some of the configurations are copied and some are killed each timestep, the total number of configurations will vary with time. As it is computationally efficient to have roughly the same num-

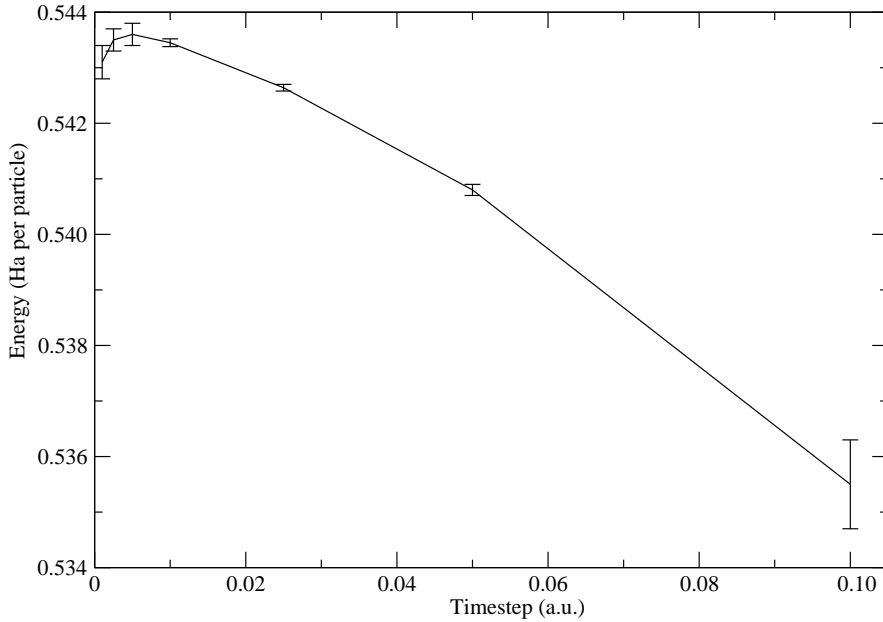


Figure 3.4: Timestep error in DMC for the ultracold atom system. The wavefunction is not well optimised, so we would expect the timestep error to be smaller for the published results. As the timestep τ is reduced, the DMC energy converges to 0.543(1) Ha per particle. The larger error bars for smaller values of τ are due to insufficient sampling of configuration space, due to the small timestep.

ber of configurations throughout the calculation, E_T is altered each timestep in an attempt to keep the number of configurations constant. This population control causes a bias. Let us assume that a lot of configurations have an energy less than the best estimate of the ground-state energy, E_{Best} , hence they are all in a region of low E_L hence the algorithm forces them to multiply. The population control tries to suppress this, so the average energy is not as low as it should be – there are less configurations with this low energy than the DMC algorithm without population control would have. Contrariwise when a lot of configurations have an energy greater than E_{Best} the DMC algorithm without population control would force them all to die. This is suppressed by the population control mechanism and hence there are too many configurations with too great an energy, hence the energy is raised. In practice PCB is rarely seen in calculations where the total population is greater than 100 configurations, although it has been seen in Wigner crystals [71]. The system we study later has not been studied by us before and therefore we have thoroughly

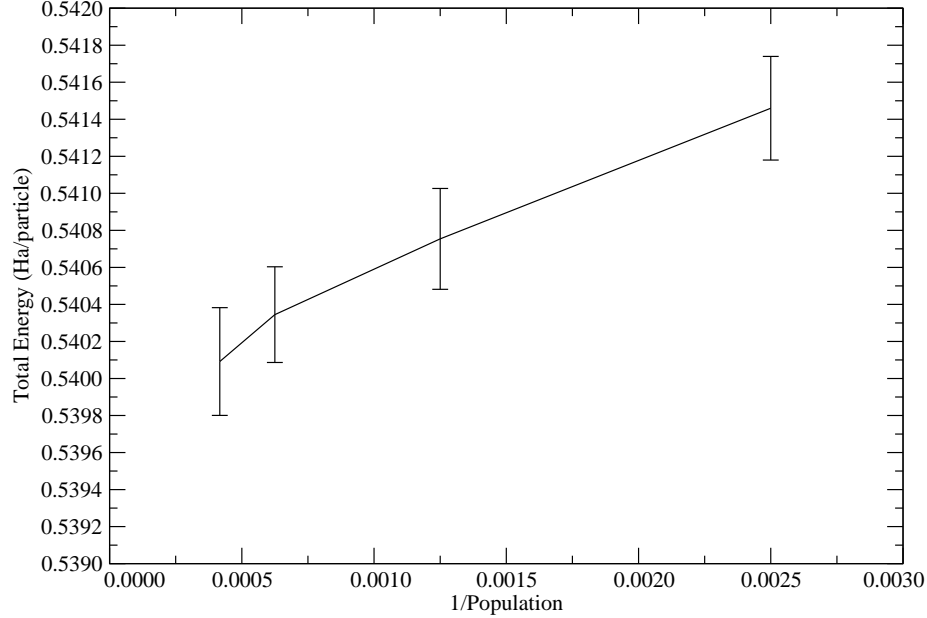


Figure 3.5: Population-control bias — We see that PCB is not an issue for large population sizes (≥ 1000), although the error-bars are still quite large. The error-bars could be reduced by running the calculation for longer. However comparing with Fig. 3.4 we see that any PCB is a tiny fraction of the timestep error. The timestep was 0.05 a.u.1 for all the points in the graph. Once fully optimised the trial wavefunction in the ultracold atom project was more accurate than the one presented here, hence we would expect a further reduction in PCB.

tested it for PCB. An example of the results can be found in Fig. 3.5.

DMC expectation values of operators which do not commute with the Hamiltonian depend on the entire trial wave function, not just its nodal surface. To reduce this bias, at the expense of an increase in noise, one can use the extrapolation approximation,[72]

$$\langle \hat{A} \rangle \simeq 2 \langle \hat{A} \rangle_{\text{DMC}} - \langle \hat{A} \rangle_{\text{VMC}} + \mathcal{O} [(\Psi_T - \Phi)^2], \quad (3.25)$$

where $\langle \hat{A} \rangle_{\text{DMC}}$ and $\langle \hat{A} \rangle_{\text{VMC}}$ are the DMC and VMC expectation values, respectively. The quantity $\langle \hat{A} \rangle_{\text{DMC}} - \langle \hat{A} \rangle_{\text{VMC}}$ gives a measure of the accuracy of the trial wave function.

3.5 The Tiling Problem

A fermionic MB wavefunction (MBWF) is a many-dimensional function that is zero on the *nodal surface*. The nodes divide the MBWF into *nodal pockets*. If the number of nodal pockets is greater than the number of configurations, which is almost always the case, there must be some pockets that contain no configurations. Configurations cannot cross nodes, by the nature of the fixed-node algorithm, so some nodal pockets **never** get sampled in DMC.

However this is not as serious an issue as it seems at first sight. The Tiling Theorem states that an exact ground-state wavefunction contains only one type of nodal pocket, all other are simply copies obtained by relabelling particles. I follow the proof by Ceperley [73].

Theorem: Define a nodal cell or pocket, $\Omega(\mathbf{R})$, as all the points that can be reached from \mathbf{R} without crossing a node. For any \mathbf{R}' not on a node, \mathbf{R}' is related to a point in $\Omega(\mathbf{R})$ by permutation \hat{P} alone, *i.e.*, $\mathbf{R}' = \hat{P}\mathbf{R}''$ where $\mathbf{R}'' \in \Omega(\mathbf{R})$ and the permutation operator \hat{P} permutes all of the positions of identical particles. Therefore $\sum_P \Omega(\hat{P}\mathbf{R})$ generates the whole space.

Proof: Assume that there is a ground-state wavefunction, $\phi_0(\mathbf{R})$, with energy, E_0 , such that,

$$\hat{H}\phi_0(\mathbf{R}) = E_0\phi_0(\mathbf{R}). \quad (3.26)$$

Assume also that $\sum_P \Omega(\hat{P}\mathbf{R})$ leaves out a nodal cell so that there exists $\Omega(\mathbf{R}_1)$ and $\Omega(\mathbf{R}_2)$ which are not related by permutation \hat{P} and they have a common border. (If there are two different types of nodal cell 1 and 2 then some permutation, \hat{P} , of the nodal cell 1 must have a border with some permutation of the nodal cell 2.)

We can now lower the energy of the system by removing the boundary between these two types of nodal cell. Eliminating a node always lowers the energy as it reduces the curvature of the wavefunction. We now have a function ϕ' that is positive in $\Omega(\mathbf{R}_1) \cup \Omega(\mathbf{R}_2)$ so that after anti-symmetrisation, $\hat{A}\phi'(\hat{P}\mathbf{R})$, we have a wavefunction that gives a lower energy than the ground state! Hence by contradiction our assumption that there are two types of nodal pocket is false.

Q.E.D.

Therefore although the configurations \mathbf{R} cannot cross a node, they all explore nodal pockets of the same type, only differing by the labels of indistinguishable particles. Hence there is no problem as long as the nodal surface of the trial wavefunction is that of the ground-state of a Hamiltonian with a local potential.

Chapter 4

Ultracold Atomic Gasses at Unitarity

THE FIELD OF ULTRACOLD atomic gasses is one where much of our intuition about the laws of physics is invalid. The very concept of localised atoms and molecules fails and we are forced to obtain our understanding from the wavefunction and by measuring the statistics of the strongly correlated exotic flavours of matter that form. Due to its ability to deal directly with the many-body wavefunction and recover large fractions of the correlation energy along with its inherent statistical nature, quantum Monte Carlo seems the ideal tool to study these types of system.

When certain atoms are cooled below a critical temperature they couple together in *Cooper pairs*. The atoms then exhibit superfluidity (the analogous phenomena to superconductivity in a charged fermionic system). The liquid has zero viscosity and loses all resistance to movement. This has truly remarkable consequences as liquid helium is now able to climb the walls of its vessel!

An equally remarkable quantum behaviour is that of Bose-Einstein condensation. When a gas of bosonic atoms is cooled below a critical temperature the particles no longer have the thermal energy to occupy a range of eigenstates. Instead, they all condense into the lowest eigenstate leading to a condensate. In both of the above phenomena it becomes impossible to distinguish individual particles and the system is best described by a macroscopic wavefunction.

Superfluid pairing in ultracold trapped atoms has been the subject of much experimental and theoretical work [74, 75, 76, 77, 78]. The range of the inter-atomic interaction in a dilute atomic Fermi gas is much smaller than the average distance between the atoms, and only the *s*-wave scattering length a is relevant. The only relevant dimensionless coupling parameter is then $1/(ak_F)$, where k_F is the Fermi wave vector of the gas.

Applying a magnetic field to the gas can cause $1/(ak_F)$ to vary from large negative to large positive values via a Fano-Feshbach resonance [79, 80, 81, 82]. This resonance occurs in the atomic collisions if there is a bound state in a closed channel coupled resonantly to an open-channel in a continuum state. The atoms are then temporarily captured by the quasi-bound state giving rise to a very large scattering length. When the interaction is weakly attractive and k_F is sufficiently small, $1/(ak_F) \rightarrow -\infty$, and the gas is in the Bardeen-Cooper-Schrieffer (BCS) superfluid regime. When $1/(ak_F) \rightarrow +\infty$, the molecules are tightly bound and the system forms a Bose-Einstein condensate (BEC). The behaviour in the intermediate regime changes smoothly with $1/(ak_F)$ and where $|1/(ak_F)| \rightarrow 0$, a smooth crossover between BCS-like and BEC-like behaviour occurs, which is called the *unitarity* point.

At unitarity, so called because the scattering length becomes larger than the inter-particle distance and the only energy scale is k_F^2 (we consider a particle mass of unity)¹, the gas has both short-range interactions between particles and an infinite scattering length. This juxtaposition is remedied by abandoning our concept of individual particles and focusing only on a macroscopic wavefunction which describes the whole system. This longe-range order is demonstrated later through the two-body density matrix.

Since the only relevant energy scale is k_F^2 , the ground state energy E_0 can therefore be written as

$$E_0 = \xi \frac{3}{10} k_F^2, \quad (4.1)$$

where the factor of 3/10 is chosen so that ξ is the fraction of the energy of the non-

¹We use Hartree atomic units, so that energies are in Ha and masses are in multiples of the electron mass.

interacting Fermi gas at the same density. A number of experimental and theoretical determinations of the universal parameter ξ have been reported. In each case the parameter was found to be smaller than unity, showing that the interactions are attractive at unitarity.

In this chapter we report calculations of the energy, pair correlation functions (PCFs), momentum density and the one- and two-body density matrices, of the Fermi gas at unitarity. We use the zero-temperature VMC and DMC methods, as have been used in previous studies [83, 84, 85, 86, 87, 88, 89]. Our study differs from earlier ones mainly in the construction of the trial wavefunctions, the larger system size used, in studying the dependence on the particle density used in the simulations and in the smaller statistical error bars obtained. Other quantum Monte Carlo methods have been used to study ultracold atomic systems at finite temperatures [90, 91].

The rest of the chapter is set out as follows, in Sec. 4.1 the model Hamiltonian we use to describe the system is discussed. In Sec. 4.2 we describe the trial wavefunction used in the calculations. The total energy and the ξ parameter are studied in Sec. 4.3 along with the pair-correlation functions, momentum density and density matrices. The condensate fraction is also obtained. A discussion of our results is presented in Sec. 4.4.

4.1 The Hamiltonian

The Hamiltonian takes the form

$$\hat{H} = -\frac{1}{2} \sum_i \nabla_i^2 + \sum_{i < j} v(r_{ij}), \quad (4.2)$$

where $v(r_{ij})$ is the interaction potential. We use face-centred cubic (fcc) simulation cells subject to periodic boundary conditions. We wish to study the system with a delta-function potential, but this is difficult to sample using Monte Carlo methods.

We have instead used the Pöschl-Teller interaction which, on resonance, is given by

$$v(r_{ij}) = -\frac{2\mu}{\cosh^2(\mu r_{ij})}, \quad (4.3)$$

where r_{ij} is the distance between particles i and j , and $2/\mu$ is the effective width of the potential well. Since the inter-particle interaction is very short-ranged, particles of the same spin are kept apart by the antisymmetry of the wavefunction, and the interaction between them is negligible for the well widths used here and would be precisely zero for the delta-function potential. We therefore set the interaction between particles of the same spin to zero, as has been done in previous calculations. The Pöschl-Teller interaction has been used in previous QMC calculations [83, 88], and we prefer it to the square-well which has also been used in QMC calculations [84, 86], because its smoothness aids Monte Carlo sampling. In all of our QMC calculations reported here we have used $\mu = 12$.

The particle density is $k_F^3/(3\pi^2)$, but we report densities in terms of the r_s parameter, which is the radius of a sphere containing one atom on average, and $r_s = (9\pi/4)^{1/3}/k_F$. For most of our calculations we have used a density parameter $r_s = 1$, so that $\mu r_s \gg 1$, as required for dilute conditions, although in Sec. 4.4 we report some investigations of the effect of increasing r_s .

4.2 QMC Methods

4.2.1 VMC and DMC Calculations for Fermi Atomic Gases

The construction of accurate trial wavefunctions for Fermi atomic gases is not straightforward. The variation of the wavefunction must be described very accurately at small inter-particle separations where the interaction potential varies very rapidly. The binding energy of an isolated molecule is vanishingly small at resonance, but the exact value of ξ for the gas is certainly smaller than the BCS mean-field value of 0.59[92], and therefore the interactions between molecules are very important at unitarity. The exact wavefunction for an isolated pair of opposite spin fermionic atoms at resonance decays as the inverse distance between the

particles, and we must describe the deviations from this behaviour in the gas phase. We conclude that it is necessary to provide a good description of both the long- and short-ranged behaviour of the pairing function to obtain accurate results for the system at unitarity.

The simulations are performed with a finite number of particles, and we wish to obtain results which accurately reflect those that would be obtained with an infinite number. Many DMC calculations have been performed for the electron gas and, to obtain accurate results, it has been found necessary to extrapolate the energies obtained from finite simulation cells to the infinite system limit. The finite size effects are reduced and the variation of the energy with particle number becomes much smoother if “twist averaging” is used, which amounts to averaging the results from a set of different wave vectors [93]. Extrapolating the twist averaged data to the infinite system limit appears to give excellent results. The DMC studies of ultracold atoms reported so far have not employed very large numbers of particles and have not used twist averaging, and it is not clear whether the results are converged with respect to system size.

Another problem is that we really want the solution for a delta-function potential, but for computational reasons we use a well of finite width. The ground state of the many-particle system with the delta-function potential is a molecular gas because bound states with more than two particles cannot exist in this case, but for a finite well-width clusters of particles can form at high densities[92]. In practice this instability of the gas phase occurs only for densities $\mu r_s \ll 1$, and we work at much lower densities. Nevertheless, it is clear that the results of QMC calculations will depend on both the well width and the particle density.

4.2.2 Trial Wavefunctions

We used a singlet-pairing BCS-like wavefunction consisting of a determinant of identical pairing orbitals, $\varphi(r_{ij})$, each of which is a function of the separation of an up- and a down-spin particle. The pairing orbital is represented by a sum of polynomial

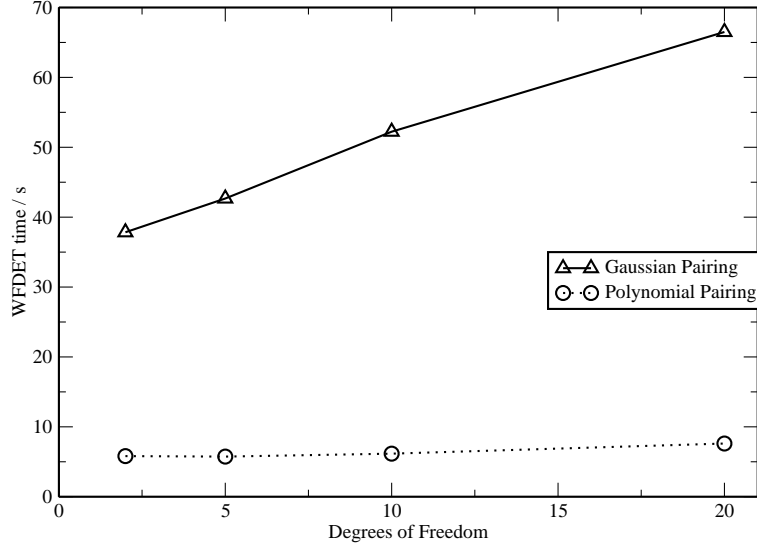


Figure 4.1: Comparison of the speed of evaluation of Gaussian and Polynomial pairing orbitals — showing how much faster the wavefunction evaluation routine, WFDET calculates polynomials than Gaussians. We plot degrees of freedom as each additional Gaussian orbital adds two degrees of freedom whereas for each additional polynomial only one degree of freedom is added.

terms,

$$\varphi(r_{ij}) = \left(\frac{L_P - r_{ij}}{L_P}\right)^3 \sum_{n=0}^{N_P} \gamma_n r_{ij}^n. \quad (4.4)$$

The third power in Eq. (4.4) was chosen to ensure that the local energy is continuous at L_P , and φ is set to zero for r_{ij} greater than the cut-off length L_P . The value of the parameter γ_1 is determined by the condition that φ is cuspless at the origin. We tested various values of N_P and chose a value of $N_P = 4$ for the results presented here. The optimised value of the cut-off length was $L_P = 3.5$ a.u., *i.e.* 3.5 times the average distance between particles. We also tested orbitals represented by linear combinations of Gaussian orbitals, linear combinations of plane waves, and combinations of Gaussian orbitals, plane waves, and polynomials. Gaussian orbitals also appeared to be a useful choice, but we chose the polynomial basis as the orbitals and their derivatives can be evaluated much more rapidly, see Fig. 4.1.

The determinant of pairing orbitals is multiplied by a Jastrow factor of the form

e^J , with

$$J(\mathbf{r}_{ij}) = \sum_{s=1}^{N_s} \lambda_s \sum_{\mathbf{G} \in s} \exp \{i\mathbf{G} \cdot \mathbf{r}_{ij}\} + \left(\frac{L_J - r_{ij}}{L_J} \right)^3 \sum_{n=0}^{N_J} \theta_n r_{ij}^n, \quad (4.5)$$

where s is a star of symmetry-related reciprocal lattice vectors \mathbf{G} , N_s is the number of such stars in the planewave expansion, L_J is an optimisable cut-off length, N_J is the order of the polynomial expansion, and $\{\lambda_s\}$ and $\{\theta_n\}$ are optimisable parameters, with θ_1 determined by the condition that J is cuspless at the origin. We set the polynomial part of J to zero for $r_{ij} > L_J$ [94]. After some testing we chose $N_s = 4$, $N_J = 8$ and $L_J = 0.86$ a.u.

We also applied backflow transformations to the trial wavefunctions [95, 96]. The particle coordinates \mathbf{r}_i are replaced by collective coordinates $\mathbf{x}_i(\mathbf{R}) = \mathbf{r}_i + \zeta_i(\mathbf{R})$, where $\zeta_i(\mathbf{R})$ is the backflow displacement of particle i , which depends on all the particle positions. The backflow displacement is given by

$$\zeta_i(\mathbf{R}) = \sum_{j \neq i} \eta_{ij}(r_{ij}) \mathbf{r}_{ij}. \quad (4.6)$$

We have used the form

$$\eta_{ij}(r_{ij}) = \left(\frac{L_B - r_{ij}}{L_B} \right)^3 \sum_{n=0}^{N_B} \rho_n r_{ij}^n, \quad (4.7)$$

where L_B is an optimisable cut-off length, N_B is the order of the polynomial expansion, and $\{\rho_n\}$ are optimisable parameters, with ρ_1 determined by the condition that η is cuspless at the origin [58]. We chose $N_B = 5$ and found the optimal value of $L_B = 1.04$ a.u.

Previous QMC calculations for atomic Fermi gases have used wave functions with an overall wave vector of $\mathbf{k} = \mathbf{0}$, so that the wavefunction is unchanged when a particle is translated by a vector of the simulation-cell lattice. Wavefunctions at other wave vectors may be constructed by multiplying each pairing orbital by $\exp \{i\mathbf{k} \cdot \mathbf{r}_{ij}\}$ and allowing the pairing orbital φ to depend on \mathbf{k} and to take complex values. As mentioned in Sec. 4.2.1, the finite size effects can be reduced by averaging energies over \mathbf{k} . We have performed calculations with 128 particles both at $\mathbf{k} = \mathbf{0}$ (the Γ point) and by averaging over results from 8 k-points which form

a uniform $2 \times 2 \times 2$ grid whose origin is chosen to provide the natural multi-k-point generalisation of the Baldereschi mean-value Brillouin zone integration scheme [40]. This generalisation, first suggested by Rajagopal *et al.* [41, 42], has been used successfully by Morris *et al.* [1, 97], as we described in Sect. 2.7.5 and we refer to it as the multi-Baldereschi (multi-B) scheme. We use canonical twist averaging, that is, the same number of particles at each wave vector.

The wavefunctions were optimised separately at each wave vector within a VMC procedure by minimising the mean absolute deviation of the local energies from their median value. We found this approach to be superior to variance minimisation schemes [98, 70]. The polynomial term in the Jastrow factor is much more important than the planewave part. The Jastrow and backflow functions can, in principle, operate between both parallel and anti-parallel spin particles, although the correlation effects between the parallel-spin particles beyond the exchange interaction already included in the determinant are small. We did, however, find a small lowering of the VMC energy when we allowed the plane wave parameters in the Jastrow factor to be non-zero for parallel-spin particles. We did not include parallel-spin terms for the polynomials, these were tested but found to be unhelpful. The wavefunction at $\mathbf{k} = \mathbf{0}$ contains a total of 28 parameters, and those at $\mathbf{k} \neq \mathbf{0}$ contain four additional parameters to account for the complex pairing orbital. A QMC calculation at $\mathbf{k} \neq \mathbf{0}$ costs about 50% more than one at $\mathbf{k} = \mathbf{0}$, due to the additional complexity of the wavefunction.

4.2.3 QMC Calculations

We used the CASINO code[99] for all of our QMC calculations. We performed some test calculations with 32 and 64 particles, but all of our results reported in this dissertation were obtained with 128 particles and either Γ or $2 \times 2 \times 2$ multi-B k-point sampling. We used a time step of 0.015 a.u. for all the DMC results presented in this dissertation. Test calculations using a timestep of 0.03 a.u. did not change the total energy within the statistical error bars achieved. We used a mean population of 3200 walkers, and tests indicated that the population control bias from this number of walkers is negligible.

4.3 Results

4.3.1 Total Energy and the ξ Parameter

When evaluating the ξ parameter it is not immediately obvious whether to use the non-interacting energy E_{NI} of the finite system studied, the infinite system, or some other value. Energies of non-interacting systems for various particle numbers, k-point samplings, and fcc and simple cubic (sc) simulation cells are shown in Fig. 4.2. E_{NI} oscillates in an irregular manner about the infinite system value as the particle number N is increased and converges rather slowly with N . Earlier DMC calculations of ξ used Γ point sampling with sc cells and particle numbers from $N = 14$ to 66 [83, 84, 87, 88]. The error in E_{NI} for the 66-particle system is quite small (0.5%), although it increases to nearly 5% for the sc cell with 80 particles. The convergence with the Γ point sampling and the fcc cell is not better than for the sc cell. The $2 \times 2 \times 2$ mult-B k-point sampling is performed in exactly the way it would be in a QMC calculation, i.e., calculations are performed at each k-point with a fixed number of particles. The results with the $2 \times 2 \times 2$ mult-B k-point sampling converge rapidly with system size, excellent convergence being achieved by 32 particles.

The convergence of the interacting energy with system size has not been well-studied, but using more particles and averaging over wave vectors is expected to improve the results. The non-interacting system has a Fermi surface, while the interacting one does not, and the presence of a Fermi surface normally leads to larger finite size effects. In the case of the non-interacting system there is occupation jumping when different k-points are used. This effect is much reduced in the interacting system case since the momentum density is smooth, with no discontinuity. One is therefore tempted to conclude that the interacting energy will converge faster with system size than the non-interacting one. However, for 128 particles we find an increase in E_{NI} of only about 2% on changing from Γ -point to $2 \times 2 \times 2$ multi-B sampling, but the interacting energy increases by nearly 13%. We use the finite-system values of E_{NI} to calculate ξ for our 128 particle systems, but is apparent from Fig. 4.2 that it would make an insignificant difference if we used the infinite-system value for $2 \times 2 \times 2$ mult-B k-point sampling, and it would make only a small difference if

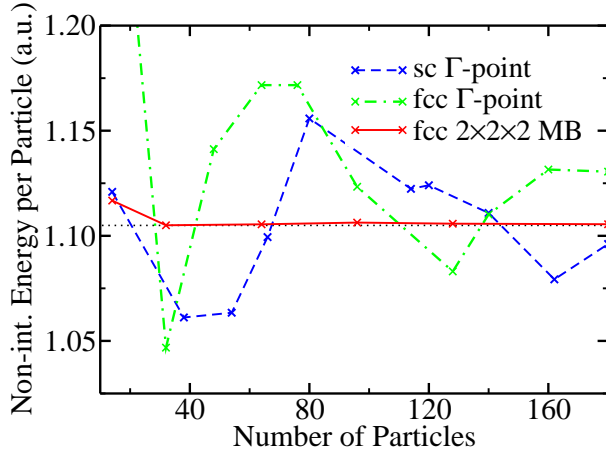


Figure 4.2: Energy per particle of the non-interacting system at $r_s = 1$ for different particle numbers and k-points. The dotted line at 1.10495 a.u. shows the exact value for the infinite system. Where MB refers to the multi-Baldereschi scheme.

we did so for the Γ -point sampling. It should also be noted that the $2 \times 2 \times 2$ multi-B QMC calculation costs about 12 times as much as a Γ -point calculation.

Our values of ξ , and those from other calculations and some experiments, are given in Table 4.1. We obtained DMC values of $\xi = 0.4339(1)$ for the Γ -point sampling and $\xi = 0.4783(1)$ with $2 \times 2 \times 2$ multi-B sampling. The Γ -point value is very similar to previous DMC values [83, 84, 87, 88], but the multi-B sampling gives a significantly larger value. The DMC energy is bounded from above by the VMC energy and from below by the exact energy and, as expected, the VMC values of ξ are a little larger than the DMC ones. Note that the differences between the VMC and DMC values of ξ are very similar (0.0178(3) for Γ -point sampling and 0.0168(8) for multi-B sampling), which suggests that the accuracy of the trial wavefunctions is similar in the two cases.

4.3.2 Pair-Correlation Functions

We evaluated the spatially and rotationally averaged pair correlation functions (PCFs) for the parallel and anti-parallel spin pairs, which are shown in Figs. 4.3(a) and 4.3(b). We performed VMC and DMC calculations for the Γ point wavefunction and for three k-points chosen from the $2 \times 2 \times 2$ multi-B set as having the most widely spaced values of $|\mathbf{k}|$. The difference in the VMC and DMC results was negligible

Method	ξ
Exp.[100]	0.32(10)
Exp.[101]	0.51(4)
Exp.[102]	0.46(5)
Theor.[103]	0.455
Theor.[104]	0.360(20)
DMC[83]	0.44(1)
DMC[84]	0.42(1)
DMC[87]	0.414(5)
DMC[88]	0.42(1)
VMC (Γ)	0.4517(3)
VMC ($2 \times 2 \times 2$ multi-B)	0.4951(8)
DMC (Γ)	0.4339(1)
DMC ($2 \times 2 \times 2$ multi-B)	0.4783(1)

Table 4.1: Values of the universal parameter ξ from experiments and theory.

on the scales of Figs. 4.3(a) and 4.3(b), and consequently the effect of using the extrapolation formula of Sec. 3.4.4 is negligible. The differences between the PCFs obtained with Γ -point sampling and the averages over all four k-points were also negligible. Figures 4.3(a) and 4.3(b) show the data itself, not fits to the data. The noise in the data is very small, but in Fig. 4.3(a) a significant amount of noise can be seen at small r/r_s , where the statistics of the accumulation are poorer. The parallel-spin PCF shown in Fig. 4.3(a) shows a hole largely confined to the region $r/r_s < 2$, which is essentially an exchange hole, and the PCF is very similar to the non-interacting (Hartree-Fock) result. This result is consistent with the fact that we found only a very weak parallel-spin Jastrow factor. The anti-parallel-spin PCF (Fig. 4.3(a)) shows a very strong enhancement for $r/r_s < 1$ arising from the pairing. The behaviour at small r/r_s is not shown as it depends strongly on the well width. The anti-parallel PCF dips below unity in the region $1 < r/r_s < 2$. The PCFs are similar to those reported in Fig. 3 of Astrakharchik *et al.* [84] and Fig. 1 of Chang and Pandharipande [87].

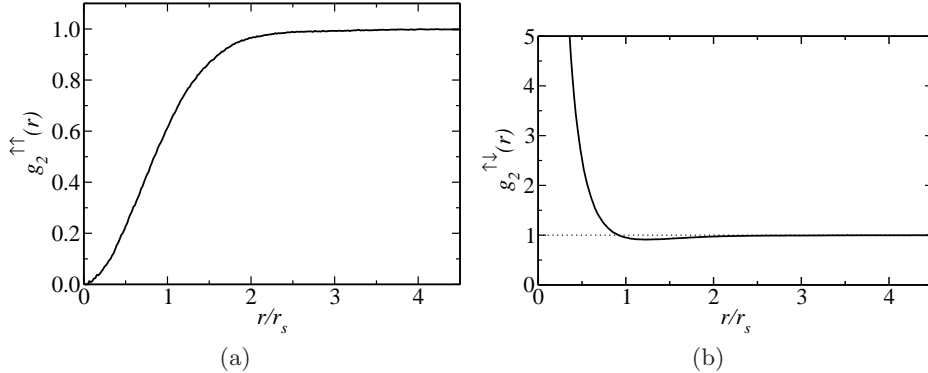


Figure 4.3: (a) Raw data for the parallel-spin PCF. (b) Raw data for the anti-parallel-spin PCF.

4.3.3 Momentum Density and Density Matrices

The one-body density-matrix (OBDM) may be written as

$$\rho_{\alpha}^{(1)}(\mathbf{r}_1; \mathbf{r}'_1) = N_{\alpha} \frac{\int p(\mathbf{R}) \frac{\Psi(\mathbf{r}'_1)}{\Psi(\mathbf{r}_1)} d\mathbf{r}_2 \dots d\mathbf{r}_N}{\int p(\mathbf{R}) d\mathbf{R}}, \quad (4.8)$$

and the two-body density-matrix (TBDM) as

$$\rho_{\alpha\beta}^{(2)}(\mathbf{r}_1, \mathbf{r}_2; \mathbf{r}'_1, \mathbf{r}'_2) = N_{\alpha} (N_{\beta} - \delta_{\alpha\beta}) \frac{\int p(\mathbf{R}) \frac{\Psi(\mathbf{r}'_1, \mathbf{r}'_2)}{\Psi(\mathbf{r}_1, \mathbf{r}_2)} d\mathbf{r}_3 \dots d\mathbf{r}_N}{\int p(\mathbf{R}) d\mathbf{R}}, \quad (4.9)$$

where \mathbf{r}_1 and \mathbf{r}'_1 are α -spin particle coordinates, \mathbf{r}_2 and \mathbf{r}'_2 are β -spin particle coordinates, and $N_{\alpha} = N_{\beta} = N/2$ is the number of particles of each spin type and $p(\mathbf{R})$ is the VMC or DMC probability distributions.

For ease of computation, and according to our requirements, we may simplify the TBDM to a function of three variables by displacing both particles at \mathbf{r}_1 and \mathbf{r}_2 by the same amount, \mathbf{r} ,

$$\rho_{\alpha\beta}^{(2)}(\mathbf{r}_1, \mathbf{r}_2; \mathbf{r}) = N_{\alpha} (N_{\beta} - \delta_{\alpha\beta}) \frac{\int p(\mathbf{R}) \frac{\Psi(\mathbf{r}_1 + \mathbf{r}, \mathbf{r}_2 + \mathbf{r})}{\Psi(\mathbf{r}_1, \mathbf{r}_2)} d\mathbf{r}_3 \dots d\mathbf{r}_N}{\int p(\mathbf{R}) d\mathbf{R}}. \quad (4.10)$$

The VMC probability distribution is

$$p_{\text{VMC}}(\mathbf{R}) = \frac{\Psi_T^2(\mathbf{R})}{\int \Psi_T^2(\mathbf{R}') d\mathbf{R}'} , \quad (4.11)$$

where Ψ_T is the trial wave function and \mathbf{R} is the $3N$ -dimensional vector of the coordinates of the N particles. The DMC probability distribution is,

$$p_{\text{DMC}}(\mathbf{R}) = \frac{\Psi_T(\mathbf{R})\Phi(\mathbf{R})}{\int \Psi_T(\mathbf{R}')\Phi(\mathbf{R}') d\mathbf{R}'} , \quad (4.12)$$

where $\Phi(\mathbf{R})$ is the wave function with the lowest energy among those with the same nodal surface as the trial wave function $\Psi_T(\mathbf{R})$.

We have evaluated the translationally and rotationally averaged density matrices, which we denote by $\rho_\alpha^{(1)}(r)$ and $\rho_\alpha^{(2)}(r)$, respectively. The momentum density $n(k)$ is the Fourier transform of $\rho_\alpha^{(1)}(r)$, but we evaluate it directly in Fourier space, which is a somewhat better numerical approach. Our data for $n(k)$ at unitarity are broadly similar to those presented in Fig. 2 of Ref. [83] and Fig. 2 of Ref. [86], although in detail there are some differences. Our data show a monotonic decrease in $n(k)$ with increasing momentum, in common with the results of Ref. [86], but in conflict with Ref. [83], which show a peak below the Fermi momentum. Carlson *et al.*[83] show VMC and DMC data for 14 and 38 particles, these VMC and DMC data are in good agreement above k_F , but below k_F there are substantial differences. The differences between the VMC and DMC data are very small in our data, and are barely visible on the scale of Fig. 4.4(a). This suggests that our trial wavefunctions are superior to those of Ref. [83]. Astrakharchik *et al.*[86] only report DMC data in the form of a fit, rather than giving the calculated values. Our momentum density is a little closer to the BCS form than the curve shown in Ref. [86].

The OBDM is shown in Fig. 4.4(b). Again, the VMC and DMC data are virtually indistinguishable so that extrapolation is unnecessary, and the differences from choosing different k-points are very small. Our calculated OBDM is very similar to that shown in Fig. 1 of [86].

The condensate fraction c is related to the translationally and rotationally av-

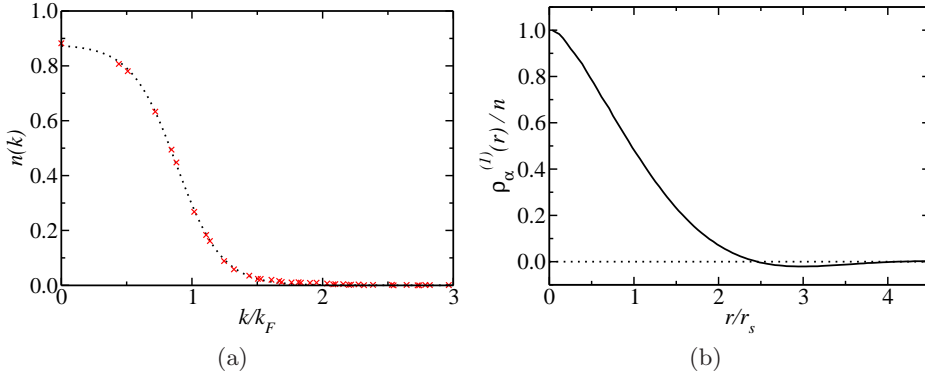


Figure 4.4: (a) Momentum density. The raw DMC data is shown (crosses) and the dotted line is a fit to this data. (b) Raw DMC data for the one-body density-matrix.

eraged TBDM by

$$c = \frac{2\Omega^2}{N} \lim_{r \rightarrow \infty} \rho_{\alpha\beta}^{(2)}(r), \quad (4.13)$$

where Ω is the volume of the simulation cell and $N/2$ is the number of pairs of particles in the system. VMC and DMC data for the TBDM are shown in Fig. 4.5. In this case we find some dependence on the calculational method (VMC or DMC) and the wave vectors chosen. The values of the VMC and DMC condensate fractions c obtained by averaging the last ten points of the data shown in Fig. 4.5 and the extrapolated values obtained using the extrapolation formula described in Sect. 3.4.4 are shown in Table 4.2. Our DMC values are lower than the DMC values of 0.61(2) for 38 particles and 0.57(2) for 66 particles reported by Astrakharchik *et al.*[86].

k-points	c (VMC)	c (DMC)	c (Extr.)
Γ	0.57	0.54	0.51
4 points	0.53	0.52	0.51

Table 4.2: Condensate fraction c in VMC and DMC, for Γ -point sampling and averaged over four k-points.

4.3.4 Varying the Particle Density

As mentioned in Sec. 4.1, we require $\mu r_s \gg 1$ for dilute conditions. This can be satisfied by, for example, fixing r_s and choosing the effective width of the potential well $2/\mu$ to be sufficiently small, or by fixing $2/\mu$ and choosing r_s to be sufficiently

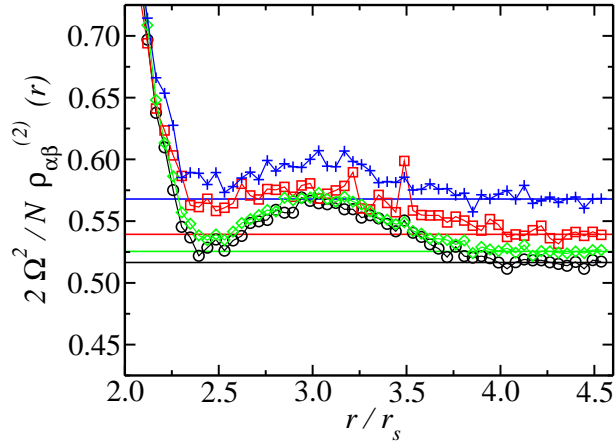


Figure 4.5: The two-body density-matrix. The blue plus signs and green diamonds show VMC data for the Γ -point and $2 \times 2 \times 2$ multi-B sampling, respectively, while the red squares and black circles show DMC data for the Γ -point and $2 \times 2 \times 2$ multi-B sampling, respectively. The horizontal lines shows the estimates of the asymptotic behaviour which gives the condensate fraction.

large. We have tried both of these approaches, but did not obtain a smooth variation of the energy when reducing the range of the interaction, at least partly because the wavefunction optimisation becomes more difficult. We obtained smoother results when reducing the value of k_F while keeping $\mu = 12$, as shown in Table 4.3, and the optimisations worked well in these calculations. The value of ξ slowly increases with μr_s , but this behaviour could arise from the fixed-node error inherent in the trial wavefunction. Note that the differences between the VMC and DMC energies increase with μr_s , indicating that the quality of the trial wavefunctions are becoming less accurate. Increasing the size of the simulation cell extends the range of the trial wavefunction and makes it more difficult to represent.

μr_s	ξ (VMC)	ξ (DMC)
12	0.456(1)	0.4370(4)
14	0.462(1)	0.4379(4)
16	0.470(1)	0.4392(6)
18	0.477(1)	0.4442(5)

Table 4.3: The energy parameter, ξ , with $\mu = 12$ and different particle parameters r_s . (128 atoms with Γ -point sampling.)

4.4 Conclusions

We have performed VMC and DMC calculations of the atomic Fermi gas at zero temperature with a short ranged interaction at unitarity using 128 particles, which is larger than in previous calculations. Energy calculations were performed using a Γ -point wavefunction and a $2 \times 2 \times 2$ multi-B grid of k-points, which should reduce the finite size errors. We found a significantly higher energy using the multi-B grid. This indicated that either finite size effects are significant with 128 particles, or that overall the wavefunctions calculated at the multi-B-grid points were of a poorer quality than those calculated at the Γ -point. It would be interesting to re-optimise the wavefunctions at the Γ -point and those at the multi-B-grid points using CASINO's new energy minimisation procedures, however currently we are not able to optimise complex wavefunctions. This could be combined with calculations at the Γ -point for different numbers of particles leading to a robust study of finite-size effects in the ultracold atom system.

Our DMC results of $\xi = 0.4339(1)$ and $0.4783(1)$ are significantly larger than those obtained from a recent application of the epsilon expansion, which gave $\xi = 0.360(20)$ [104]. The VMC and DMC results for the spherically-averaged pair-correlation functions, the momentum density, and the one-body density matrix were in good agreement, illustrating the high accuracy of our trial wavefunctions. The results for the two-body density matrix, and the condensate fraction derived from it, differ in VMC or DMC and depend somewhat on the wave vector used, indicating that significant errors still arise from the approximate trial wavefunctions and/or finite size effects. We have calculated a somewhat smaller condensate fraction than in other studies using similar methods. We also calculated the variation of ξ with the particle density for a fixed well width, finding a relatively small variation over the range of densities studied, but we were unable to draw a firm conclusion as to whether these variations would be present in a calculation without fixed-node errors.

We are now able to reflect on the non-intuitive behaviour of the ultracold atomic Fermi gas at unitarity. From the parallel-spin PCF in Fig. 4.3 (a) we see the usual exchange hole between like-spin particles, as we would expect in a Fermi gas. The enhancement of the anti-parallel spin PCF (Fig. 4.3 (b)) below $r/r_s = 1$ implies

pairing between opposite spin particles forming molecules. However the condensate fraction, obtained from an analysis of the TBDM shows a long range correlation between particles of anti-parallel spin up to and beyond $r/r_s = 4.0$, even though the interaction has an effective width of $r/r_s = 0.167$. Hence the evidence suggests that the system is dilute, yet strongly correlated. A truly remarkable result.

Chapter 5

Discussion

5.1 Summary

In PART I random numbers were used within the Metropolis algorithm to efficiently sample quantum mechanical expectation values via VMC and DMC.

A discussion of single-particle theories was presented in Chapter 2 along with a practical discussion of planewave-basis-set density-functional theory calculations. Towards the end of the chapter the multi-k-point generalisation of the Baldereschi mean-value Brillouin zone sampling scheme (multi-B) was presented as outlined by Rajagopal *et al.*[41, 42]. The clear superiority of the multi-B scheme over standard Monkhost-Pack (MP) meshes was shown with the example of diamond-structure silicon (see Fig. 2.4). This increased accuracy, however, came at a price: the number of k-points used in the multi-B scheme is not normally reduceable by symmetry, in contrast to the MP mesh. Hence by using symmetry to reduce the number of k-points calculated, finer MP meshes may be used for the same computational effort. However, in the cases where imposing a symmetry on the system would introduce a bias into the results, such as in the case of AIRSS simulations applied to point-defects, the multi-B scheme is the most efficient and accurate scheme to use, for a given number of k-points.

In Chapter 3 the QMC method was discussed in detail. A discussion of some of the practical aspects of QMC calculations was given, such as population control

bias and timestep error. The chapter was concluded with a discussion of the Tiling Theorem. The Tiling Theorem supports the use of a relatively small number of configurations of the system to sample a wavefunction in high-dimensional configuration space. It shows that where naïvely one might think that sampling a small number of nodal pockets would lead to biased results, in fact, all nodal pockets of the same type (positive or negative) are related through permutations of electron labelling.

With a thorough understanding of electronic structure and QMC methods these ideas were applied to a system of ultracold atoms in Chapter 4. QMC is ideal for studying this kind of strongly correlated system due to its ability to recover very high fractions of the correlation energy. A model atomic interaction between atoms of opposite spin types was implemented in CASINO¹, along with a new pairing orbital based on polynomial functions of the distance between pairs of opposite-spin atoms using polynomial functions. This new pairing orbital retained the flexibility of the Gaussian pairing orbitals already implemented, but at a greatly reduced computational cost, see Fig. 4.1.

At unitarity, the BEC-BCS crossover point, the only relevant length-scale is that of a non-interacting gas, for this reason we calculated the ratio of the energy of the interacting gas to that of the non-interacting gas, ξ , which is a universal parameter. Within DMC we obtained $\xi = 0.4339(1)$ which agrees well with other QMC calculations. However, we proceeded to sample the Brillouin zone more accurately than in previous work using the multi-B scheme. Using the multi-B scheme we obtained $\xi = 0.4783(2)$ which is higher than the values obtained in previous work. We conclude that finite-size effects are significant in the 128 atom cell, although maybe less than the difference between Γ -point sampling and multi-B sampling results indicate. The variance per particle of the VMC optimisation calculations suggests that the wavefunctions calculated at the multi-B k-points are of a slightly poorer quality than the wavefunction calculated at the Γ -point.

We also used both VMC and DMC to calculate other expectation values: the parallel and anti-parallel pair correlation functions, the one-body density-matrix

¹By P. López Ríos

and the momentum density. The difference in the VMC and DMC results for these expectation values was very small, implying that our trial wavefunction is quite accurate.

We then obtained the condensate fraction of particles from the two-body density-matrix, the difference between the Γ -point result and the multi-B result was small, 0.512(9) compared with 0.508(8), showing that the Brillouin Zone sampling is perhaps more important for the calculation of the total energy than other expectation values. The value of the condensate fraction calculated in previous work [86] is ~ 0.58 , which is close to but does not agree well with our calculation.

With accurate Brillouin zone sampling any biases left in the results must come from the fixed-node error – which we cannot fully control – or from the finite well-width. The range of the interaction between opposite-spin particles is very short compared to the average distance between particles. The well must be allowed to tend towards an infinitely narrow well: that is, the well-width parameter, $\mu \rightarrow \infty$. This leads to a problem, since as the well-width tends to zero, the wavefunctions become progressively more difficult to optimise since many more configurations of the system are necessary to sample the narrow well. The narrowing well increases the noise in the calculations and makes it very difficult to extrapolate the results to $\mu \rightarrow \infty$. Whilst ξ only varied by 0.007 between $r_s\mu = 12$ to $r_s\mu = 18$, it was not possible to study any narrower well-widths. If more accurate results are needed, this finite well-width problem must be addressed.

It may be that energy minimisation of the trial wavefunctions would yield more accurate results. The multi-B method requires complex wavefunctions currently only optimisable using variance or mean absolute deviation minimisation within CASINO. It was felt that the increase in accuracy brought about by using the multi-B method was more important than using energy minimisation on a single Γ -point calculation.

5.2 Outlook

QMC is the most promising method for providing ground-state energies of large systems to chemical accuracy. It scales much better with system size than other

quantum chemistry methods of a similar accuracy such as Configuration Interaction and Coupled Cluster methods. QMC computer programs are also more flexible than other quantum chemistry codes.

The future of QMC is unclear. Whilst it allows us to calculate a very accurate ground-state energy, charge density and other expectation values, it is computationally expensive to obtain information about the band structure of materials or obtain orbitals suitable for inclusion in excited-state theories such as the *GW* approximation and the Bethe-Salpeter equation. There are dreams of structure optimisation and even molecular dynamics calculations within QMC. Whilst forces are beginning to be accessible [105, 106, 107, 108] it remains very unclear whether these could be calculated within DMC, ions moved, wavefunctions re-optimised and new forces calculated fast enough to perform geometry optimisation.

Moore's law is on QMC's side though: the doubling of computational power every 18 months looks set to continue. QMC can take advantage of the multiple cores in a single chip – VMC is perfectly parallelisable, and if DMC is implemented carefully it should have little problem scaling to hundreds of thousands of processors. This can be further improved by using graphics processing units (GPU) which are now a cheap way to obtain large amounts of computing power.

DMC requires communication between nodes in a massively parallel machine. For load balancing purposes configuration numbers on each node must be approximately equal. For this reason configurations must be swapped between nodes as well as the reference energy, E_T . Since collecting, averaging and redistributing the reference energy to all nodes is necessary at each timestep, this process effectively becomes the “bottle-neck” in the DMC algorithm on very large computer clusters. However, this problem can be overcome by hiding the latency of the collection, averaging and redistribution. This would be achieved by each node sending its reference energy to a master node, but continuing its DMC calculation into the next timestep. Then, at a later time, receiving the updated E_T and correcting for the use of the “wrong” E_T in the interleaving period.

It has been shown recently that correlated configurations lead to a lack of efficiency in DMC for large system sizes [109]. The variance in the local energy increases

proportional to system size². The larger the variance, the more branching that occurs in the DMC algorithm. However, the correlation time of configuration remains constant. Hence it has been shown that for large systems the number of independent configurations decreases with system size for a given variance and the computational effort increases exponentially with system size (not as $\mathcal{O}(N^3)$).

A critical discussion of QMC techniques would not be complete without a discussion of fixed-node error. It seems logical that the better the nodes of the trial wavefunction, the better the overall DMC calculation should be. This idea was explored by Lüchow *et al.*[110] who note that the nodes of the exact Ψ are at the same positions as those of $\hat{H}\Psi$. Hence they devise a scheme to optimise a wavefunction until the nodes of these two functions match. This may not be as beneficial as it seems: an accurate nodal surface will lead to an accurate DMC energy, but other expectation values benefit from a good overall wavefunction, not just good nodal positions. Recently a scheme has been reported [111] which allows the nodes of a trial wavefunction to be systematically improved, however, this method is stable only for small systems.

This leads us to our final point. The many-body problem is believed not to be solvable exactly in polynomial time. Whilst it is far from clear which class of problems the many-body problem belongs to, it may be that it can be solved using a quantum computer. Since algorithms have been written to solve exponentially hard problems in polynomial time using a quantum computer, and since some of these problems can be mapped into other problems of the same class, it may be that the fermion-sign problem is solvable. It would be ironic indeed that the very problem we chose to study, namely the quantum behaviour of electrons, may only be solvable using a quantum computer that relies on the quantum behaviour of electrons.

²Consider the variance in the local energy for a simulation containing one hydrogen atom compared with a simulation containing two hydrogen atoms.

Part II

Random Structure Searching

Chapter 6

Sampling Structures with Random Numbers

6.1 Introduction

IN 1869 THE SWISS PHYSICIAN Friedrich Miescher (1844–1895) discovered a microscopic substance on discarded surgical bandages [112]. He called it “nuclein”, as it was found in the nucleus of cells. There was much discussion over the constitution of nuclein. However, little progress was made in understanding its purpose. The class of substances became known as *nucleic acids*.

It took another 84 years until the structure of the most famous nucleic acid was determined. The X-ray diffraction experiments were performed by Rosalind Franklin [113] and allowed James Watson and Francis Crick [114] to suggest that the substance has a double helix structure. The substance was deoxyribonucleic acid (DNA) and with further work by Crick it was shown that the genetic code it contained was based on codons, which are sequences of the base pairs of DNA. The progress in understanding DNA is a good example of the necessity for determining structures at the atomic level.

Structure determination and predication is very important as there is an ever-increasing demand for new materials in science and technology. The ability to accurately describe and thus understand the characteristics of a material is vital for

technological progress. New technologies demand new materials with characteristics specific to their intended application. For example, we know how to make hydrogen fuel cells to replace batteries in electric cars. However, we have yet to find materials that can be used to store hydrogen safely and efficiently until it is required. The desired material must be able to store and release hydrogen molecules easily and safely, be light enough not to add too much weight to the car and must be easy to manufacture.

To improve batteries we need light materials that are able to store charge for long periods of time. Space exploration demands materials with high melting temperatures, or that are hard-wearing yet light. Medicine also benefits from developments in structure prediction. The study of molecular crystals is important to the pharmaceutical industry. Different molecular crystals made from the same constituent molecules can have quite different properties as drugs, such as their solubility. Hence it is vital for the industry to be able to predict which structures will form under different manufacturing conditions.

Understanding the structure is the key to understanding a material, as different arrangements of a set of atoms can exhibit radically different properties. An example of this is the difference between diamond and graphite, shown in Fig. 6.1. Both materials are made from carbon atoms; it is simply their different arrangements that make diamond the hardest material known to us, whereas graphite will easily flake from the end of a pencil onto paper. Graphite conducts electricity (although not particularly well), whereas diamond is an insulator.

The understanding of structures is of great importance to the semiconductor industry. Semiconductors are the constituent materials of the transistors and microchips found in every computer, television and mobile phone. The semiconductor industry has a £100 billion per annum market and if the current trend continues there will soon be no device left in the home that does not contain a microchip, from microwave ovens to electric toothbrushes. However, at the atomic scale we still do not have a full understanding of semiconductors.

Semiconductors are doped with small quantities of other elements. This introduces *donor* and *acceptor* states within the band gap, allowing them to conduct

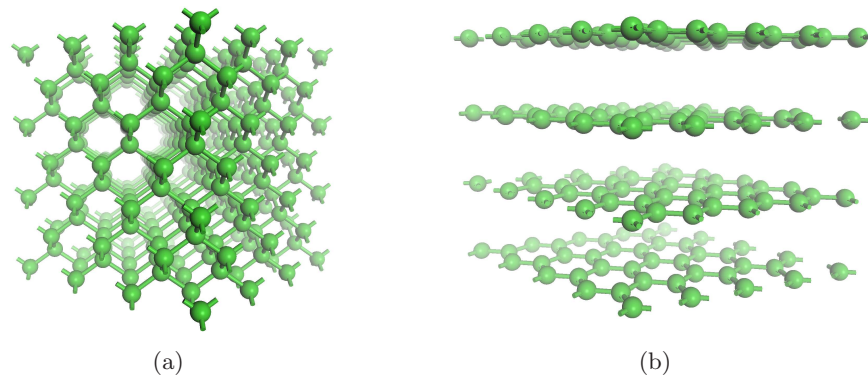


Figure 6.1: Allotropes of carbon. (a) Diamond: the hardest material known. All of the carbon atoms have four tetrahedral covalent bonds, making a strong rigid structure. (b) Graphite. Carbon atoms are arranged in graphene sheets, each atom has only three bonds. The remaining electrons bond the graphene sheets together weakly, making graphite soft.

electricity in certain ways. Hydrogen, nitrogen and oxygen atoms readily enter the semiconductor during manufacture, forming point *defects*. These defects can passivate the donor and acceptor states, making it a much poorer semiconductor, or change the size of the band gap, such as when nitrogen is added to gallium arsenide [115].

For many years experimentalists have used X-ray crystallography to *see* atomic positions inside materials. Theorists have suggested new structures by considering the way in which materials with known structures behave and models of how atoms bond. The predictions of structures remains a difficult problem for both experiment and theory. Experimentalists cannot *see* the structures of defects well, whereas theoreticians have difficulties because of the huge number of possible atomic arrangements. The energy associated with each arrangement can be calculated, and those with the lowest energies are the more likely to form naturally.

We conclude that there is great cause for studying structure determination and prediction methods, as the problems faced are challenging, but the potential gains for technology are great. We now discuss different theoretical search methods available.

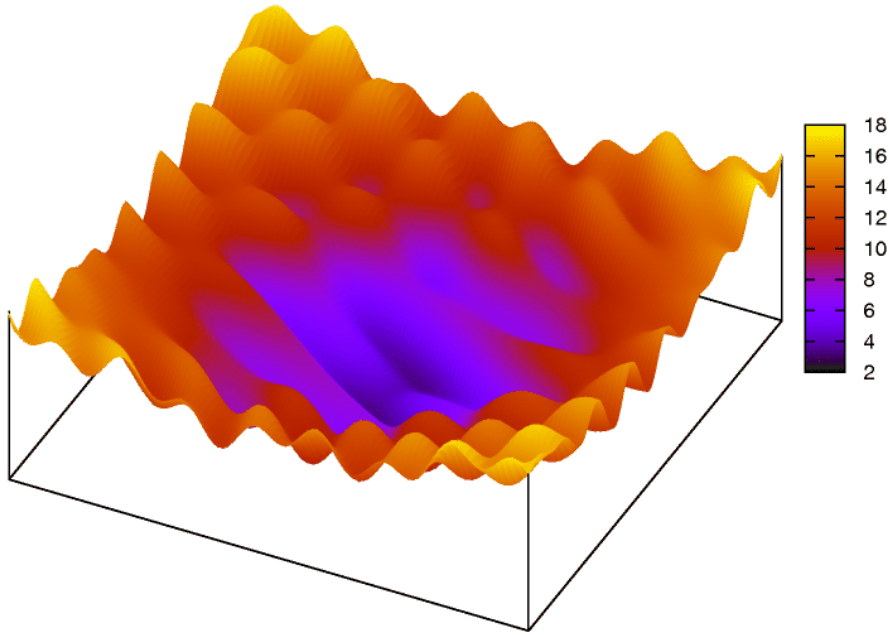


Figure 6.2: A representation of a complicated, 2-dimensional energy surface . This is often called an *energy landscape*.

6.2 Search Methods

In order to discuss structure search methods we must understand the concept of an *energy surface*. This is the surface in $3N$ -dimensional space in which each point represents the energy of a particular *configuration* of atomic positions. Each dimension in this space represents a co-ordinate of an atomic position.

This surface is generally very complex and contains many local minima of which we would like to find the global minimum. Finding the global minimum of this energy surface is equivalent to knowing the atomic co-ordinates of the ground state structure of the system. The two main classes of global minimum searching methods, *simulated annealing* and *genetic algorithms*, will be discussed later in this chapter. These will be contrasted with the new *ab initio random structure searching* technique.

We can imagine the energy surface as a landscape, containing many hills, mountains and valleys. If we imagine a rain-shower over the land, the water always runs down-hill to the nearest river. All of the points on the surface where rain runs into

the same river are defined as the river's *basin of attraction*. The river runs into a lake. The lake, is of course a local minimum in the landscape: there may be other deeper valleys, but for the basin of attraction in question, its corresponding lake is the lowest point in the valley.

Finding local minima in energy surfaces is not a difficult problem. First of all we should discuss a *line minimisation* algorithm. This is simply an algorithm for finding a local minimum in a 1-dimensional space. The algorithm takes successive steps from its start point along the line until it finds a point where the gradient becomes positive, that is, until it begins to travel uphill. It then reduces the stepsize and searches between these two extreme points for the lowest point. There are a number of ways to find its minimum, such as *bisection* searches or *golden ratio* searches. The latter is explained in Fig. 6.3 and its caption.

The energy surface is generally more than 1-dimensional, so we employ a higher dimensional algorithm. The simplest method, called *steepest descents*, consists of a succession of line minimisations. Each time the lowest point in the line is found, the search continues in a new direction, defined as the direction which has the largest (negative) gradient. This process continues until the surface appears locally flat to some predefined tolerance.

Steepest descents, can be improved by using the *conjugate gradient* method. The method proceeds in a similar way, using successive line-minimisation steps. However each new direction is chosen to be the steepest decent possible whilst being orthogonal to all previous search directions. This greatly speeds up the search for a local minimum.

We know that to obtain the ground state structure of a system we need the global minimum. The methods described below use the local minimum techniques described above, but also contain ideas of how to jump from one basin of attraction to another in order to sample more of the configuration space. Finding the global minimum of an energy surface is widely believed to belong to the class of NP-hard problems¹. The set of NP-hard problems are characterised by having no known al-

¹The class of NP-hard problems are at least as hard as the class of NP problems, but do not necessarily belong to the NP set. NP problems are verifiable but not solvable in polynomial time [116].

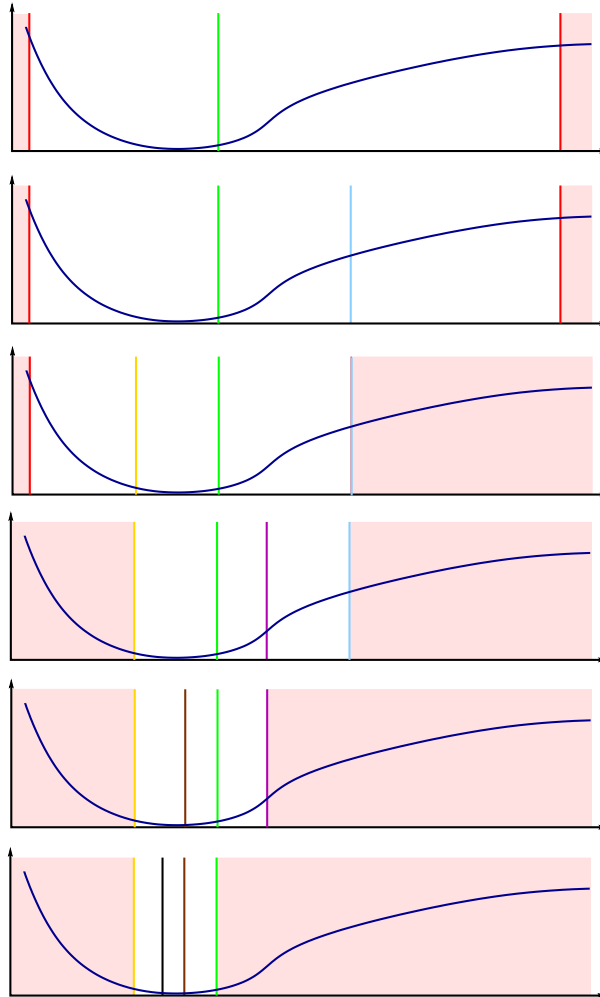


Figure 6.3: Golden Section Search. We wish to find the minimum of the dark-blue function between the two red-line limits in the top figure. The function is evaluated at the green line, the point which divides the interval between the red lines by the golden ratio. The largest of the sub-intervals is sampled, again in the golden ratio by the blue line. If at the blue line the function was higher than at the green line then the interval green-blue-red would be taken to the next stage, but since blue is higher than green, we take red-green-blue. We now subdivide the largest subsection of this new interval with a yellow line. Since yellow is higher than green, we take the interval yellow-green-blue into the next iteration, and divide the largest section with the magenta line. The division by the golden ratio and discarding, based on the new sampling point is continued down the page with the brown and black lines until the difference in the function at the pink endpoints is less than some predefined tolerance. The minimum is taken as the average of the two endpoints.

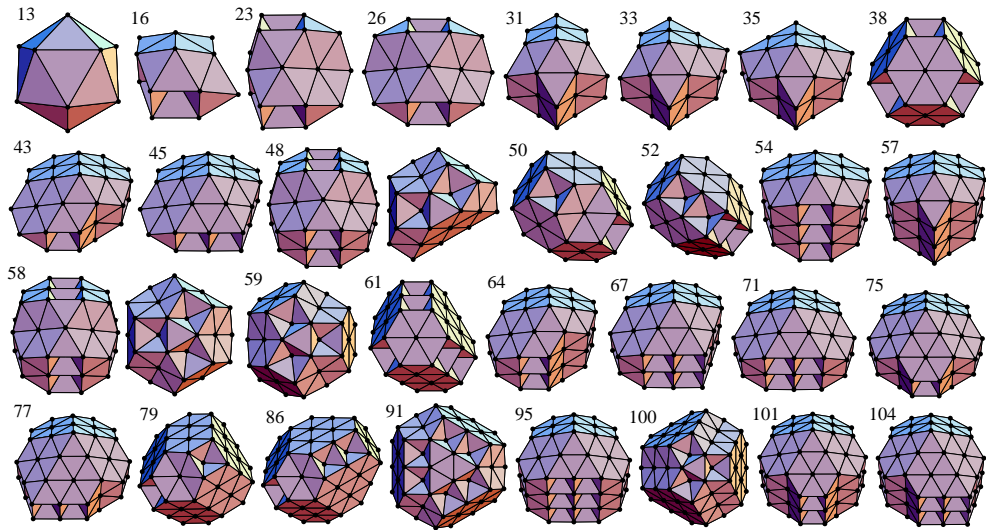


Figure 6.4: Lennard-Jones atomic clusters taken from Doye *et al.* Phys. Rev. B **64**, 235409 (2001) [117]. The numbers of atoms in each cluster is given. These are a classic test-bed for computational structure searches. The forces between atoms are quick to calculate, so it is easy to search large volumes of configuration space to find the global minimum energy structure.

gorithm that guarantees to find their exact solution in polynomial time. This means that the cost will increase exponentially in time for a given increase in complexity. Since the number of local minima increases exponentially with the number of atoms in the problem it is very plausible that the problem is NP-hard.

One of the most important test-beds for different search methods is clusters of atoms, see Fig. 6.4. Atomic clusters can form in many ways, but there is usually only one configuration of atoms that has the lowest energy. They are ideal for testing these types of methods as they have a relatively small configuration space and are quick to calculate in a computer either using classical potentials, or from *ab initio* techniques such as DFT. It is also easy to systematically increase the complexity of the search space by adding atoms.

6.2.1 Simulated Annealing

The method of steepest descents is a *greedy* algorithm; it always goes in the direction that maximises gain (*i.e.* minimises the energy). This of course means that it can never move from one basin of attraction to another as this involves going up-hill some of the time. Simulated Annealing (SA), devised by Kirkpatrick *et al.* [118],

allows the search to move from one basin to another. There is an analogy between this global minimisation technique and the way that a metal cools. Atoms move around as if the system is in contact with a heat-bath of temperature, T . As the simulation progresses, T is slowly reduced, *cooling* the simulation into a basin of attraction.

At each stage of the simulated annealing algorithm a small atomic displacement is proposed. This step is accepted if it reduces the total energy of the system. The atom is moved, and the process begins again. However, if the step increases the total energy by ΔE , the probability of accepting the move $P(\Delta E)$ is calculated as,

$$P(\Delta E) = \exp\left(\frac{-\Delta E}{k_B T}\right), \quad (6.1)$$

where k_B is the Boltzmann constant. Only if $P(\Delta E)$ is greater than some uniform random number between 0 and 1 is the step accepted, otherwise it is rejected and a new atom move is proposed.

If we go back to the analogy of rainwater in a valley, this method allows the possibility of water flowing up-hill, proportional to the temperature of the system. This means that there is a finite probability of the search moving from one basin of attraction to another, allowing the system to escape from a local minimum. As the simulation progresses, and the temperature decreases, the search is frozen into a particular basin.

The temperature, T , is a scale for what features of the energy surface the algorithm samples. At high T , it does not see the tiny features of many local minima but rather it favours areas of the energy surface that are lower on average. As the temperature is reduced, the algorithm sees progressively finer features. If the annealing is performed slowly enough the algorithm has time to find the basin with the lowest minimum, that is, the one that contains the global minimum of the system. SA's strength is its ability to sample the surface at different scales, and home-in on the global minimum. Let us take, for example, a surveyor who is set the task of finding the lowest lying place in the UK. They would start from a map of Britain, discard Snowdonia and the highlands of Scotland and decide to refine their search in East

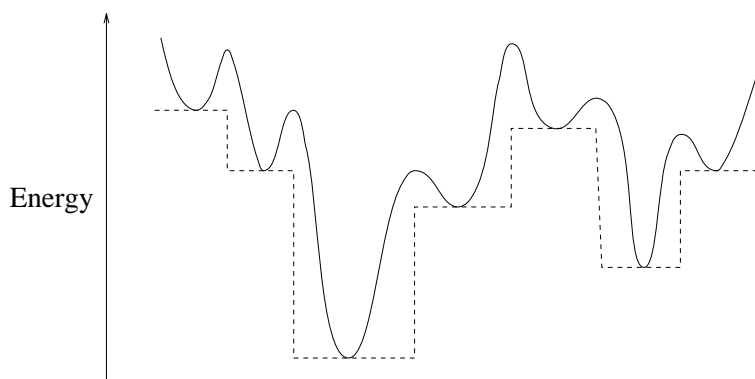


Figure 6.5: An example of the auxiliary surface taken from Prentiss *et al.*, J. Chem. Phys. **128**, 225106 (2008) [122]. The curved line is the original energy surface, which is deformed into a surface where each point in a basin of attraction is mapped to the local minimum of the basin, shown as a dotted line. This reduces the fluctuations in the surface by removing the larger peaks, making it easier for the SA algorithm to move around the energy surface.

Anglia before even leaving their office². They would be foolish indeed to start at John O’Groats and measure the height above sea level every metre along a walk to Land’s End.

A SA run should tend to the global ground state if the temperature is reduced infinitely slowly. Hence for best results T should be reduced as slowly as possible which leads to long simulation times. The *annealing schedule* has to be “just right”, otherwise the results will be biased. SA in its pure form seems impractical for all but the simplest systems, although it has been shown to work well for Lennard-Jones clusters [119].

To improve the speed of the algorithm, various modifications have been proposed, such as the Gaussian Density distribution method devised by Ma and Straub [120]. This attempts to model how the density in configuration space changes with reductions in temperature, T . It has been applied to clusters of water molecules with good results [121].

Temperature bouncing has been proposed by Schneider *et al.*[123] to allow faster decrease in temperature by periodically raising the temperature of the system. The analogy used in their paper is that of a blacksmith. Once the molten metal is cooled

²Their random walk would end at Holme Fen in Cambridgeshire, which is 9 metres below sea-level.

into a rough shape and worked, it is then heated up again until it just glows red, not until it re-melts. It is then re-worked and heated again – sometimes quenched in water, other times allowed to cool slowly. By systematic heating, working and quenching it is possible to get the correct microstructure of the worked metal, without completely re-melting the sample.

Perhaps the most advanced modification is *Basin Hopping* [124]. This maps the energy surface onto another flatter auxiliary surface, see Fig. 6.5. This auxiliary surface is produced by changing the value of the energy at each point in a basin to the minimum value of the basin. This makes a much flatter surface and makes it easier for the algorithm to climb high mountains to find the global minima. Again, the method has been performed on Lennard-Jones clusters.

However, even with these improvements, SA remains very slow. It seems that *parallel tempering* is the most promising enhancement to the basic SA algorithm, see the review article by Earl and Deem [125]. The method uses M replicas of the system, and carries out the random walks over the energy surface *at different temperatures*. The different systems are then allowed to swap configurations whenever their different probability distributions overlap. Although this method is M -times more expensive than standard SA, it reduces the computation time by more than $1/M$. Now ensembles exploring at low T , which would not otherwise have the chance to change basins, are able to swap with higher temperature ensembles, increasing their chance of finding the global minimum.

A method based on parallel tempering with empirical van der Waals forces and DFT has proved to be very successful [126]. This method was compared against a number of others in a blind test of molecular crystal structure prediction organised by the Cambridge Crystallographic Data Centre. It was able to predict the ground state of structures of four molecular solids very accurately. I think that this methodology is clearly the way forward for SA.

6.2.2 Genetic Algorithms

Genetic algorithms (GA) were first suggested by John Holland in his book, *Adaptation in Natural and Artificial Systems* [127], and are explained in detail in the review article by Johnston [128]. GA is a method of global optimisation based largely on Darwin's [129] theory of natural selection, where the genetics of the fittest of the population preferentially carry into the next generation of the species. Here the population is not a *species* of animal but a set of structures, where the structures are bred through successive generations to produce the ground state structure. The *genes* passed down in this case are the atomic positions.

The process can be split up into 6 parts, see Fig. 6.6.

Population generation: A set of different *guesses* for the trial structure is chosen. It is best if these are chosen at random, so that the initial starting configurations are unbiased. It is important to use a population which gives a representative sampling of configuration space, not necessarily just low energy structures. The later stages of the algorithm rely on the diversity of the population.

Assignment of fitness: The different members of the population are assigned a fitness. This is a measure of how similar to the desired result each member is. We are trying to obtain the global minimum of the energy function, so the lower the energy of the structure, the *fitter* it is for our purpose.

Selection: A subset of the population is chosen for breeding. Simplistically this could be just the fittest half of the population. However, this can sometimes lead to *stagnation*, where the population gets stuck in a local minimum and does not have enough variation to improve. Hence it is normally better to select the breeders stochastically so that it is more likely that a fit member of the population will breed but also possible for less fit individuals to contribute their genes to the next generation. This is called *roulette wheel* selection.

Another method is *tournament* selection, where all of the population are paired randomly. The fittest of each pair goes on to the breeding stage. This again allows many more genes to be present at next stage.

Breeding: The subset of the population chosen for breeding is then paired, and

half of each of the genes of the parents are passed to the offspring. In our case, each of the structures will be cut into two and spliced together to form a new structure.

Mutation: In order to keep the population from stagnating, a random mutation may be added to the offspring. For example: this could be a random displacement of one or more of the atoms of the offspring; twisting one of the structures in the breeding step through some angle, before splicing; or a pairwise swap of atomic types. Each of the offspring is then relaxed to a local minimum. Technically this is now a *Lamarckian* theory of evolution since we are now allowing the population to adapt to its surroundings (*i.e.* minimise its energy) *during its lifetime*, which is not a trait found in Darwinism. This Lamarckian addition to GA, sometimes now called an Evolutionary Algorithm, is clearly the correct thing to do for structure determination. It has been tested using an Ising Hamiltonian representation of an $\text{Au}_{1-x}\text{Pd}_x$ alloy [130] and was shown to improve convergence to the lowest energy structures over Darwinian evolution alone.

Natural Selection: The fitness (energy) of each of the new offspring is calculated and they are pooled back with the rest of the population. Some of the population's un-fittest members are then removed.

This process is repeated through new generations until the desired low energy structures are discovered in the population.

GA has been applied to clusters [128] and fullerenes [131], where it successfully discovered fullerene cluster structures up to C_{60} , starting from random atomic positions. Oganov's group in Zurich have successfully applied GA to a range of problems from molecular crystals to solids [132, 133, 134]. The method has found many new high pressure phases of solids such as sulphur, oxygen, nitrogen and CaCO_3 .

GA has also been shown to be advantageous over normal Monte Carlo sampling for lattice binary alloy models [135] in which the species at each lattice point is chosen to minimise the total energy of the lattice. More recently the algorithm has been improved to reduce stagnation [136] by allowing symmetrically equivalent members of the population to be formed from a single configuration³. This allows

³Note that structures that are related by a symmetry operation have the same energy and hence the same fitness.

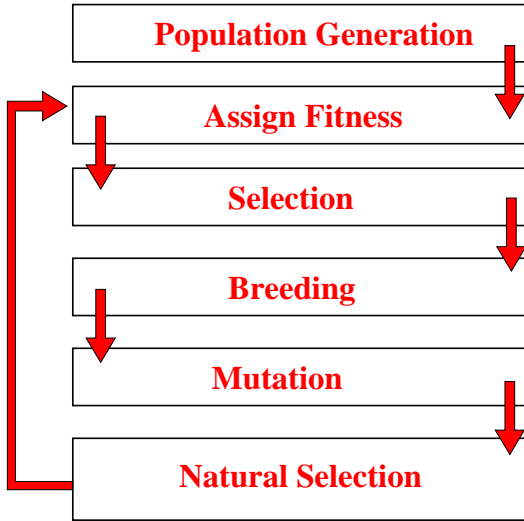


Figure 6.6: The Genetic Algorithm

the evolution of *symmetry* throughout configurations, reducing the probability of stagnation to local minima.

There has also been much interest in applying the method to periodic systems [137]. This was tested on polymorphs of carbon and was able to recover both the graphite and Lonsdaleite-like structures [138]. In order to reduce stagnation, Abraham and Probert [139] enhanced the fitness function, to include a simple structure factor, as well as the enthalpy of the structure. This allowed duplicate structures to be discouraged, giving a greater diversity in the population. This successfully reduced stagnation, enabling the discovery of three new phases of model systems using the Dzugutov potential.

6.2.3 Random Structure Searching

Within the last three years a new method has been developed at the Universities of Cambridge and St. Andrews. The new “*ab initio* (or first-principles) random structure searching” (AIRSS) computational approach, shown pictorially in Fig. 6.7, has led to the discovery of structures which have since been verified by experiments. The method is perhaps the simplest imaginable for obtaining new structures. It is the most unbiased algorithm we can think of.

The problem with *ab initio* structure searching is computational cost. It seems

a good idea to use DFT methods from the outset of the minimisation technique. Cheaper methods exist but greatly increase the chance of finding false minima. DFT is an expensive method however, so we must decide how to spend the limited number of energy evaluations wisely.

A population of structures is generated by randomly placing atoms within a simulation cell. Strong overlap between atoms is rejected as an unphysical starting point. The rejection is not much of a bias as atoms close together would produce large forces in order to move them apart in the early stages of the simulation. We are merely avoiding computational instabilities, since if atoms are too close together this may cause the overlapping of cores of the pseudopotentials. The cell vectors are chosen to be within $\pm 50\%$ of some chosen value, so that there is freedom in the initial volume. Whilst retaining the structure, these vectors are then modified to make the cell more cuboid and less flat, which makes it easier to deal with computationally.

These random configurations are then relaxed using DFT to calculate the forces on the ions and stresses on the unit cell. The DFT calculations must be performed at a good level of accuracy. For example, insufficient BZ sampling leads to structures with unphysical periodic density waves. The convergence to zero force and the required pressure need only be good enough so that candidate structures can be distinguished and so that their symmetries can be determined.

The searches are performed using different random starting points until either the same structures appear many times (in this case we assume that we have sampled configuration space sufficiently) or until the computational budget is exhausted. Once a large ensemble of structures has been relaxed, the lowest energy and most symmetric are further analysed. Since the set of candidate structures has been reduced from say, 1000, down to perhaps 5 it is now feasible to continue their relaxation with more accurate computation. It is not worth doing so at the initial search stage as 995 out of 1000 calculations would have been wasted.

More DFT calculations are performed on the five candidates with higher force tolerances, more complete basis sets and finer BZ integrations. From the results of these, the lowest energy structure is taken as the ground state.

This approach is surprisingly successful and its performance for large systems

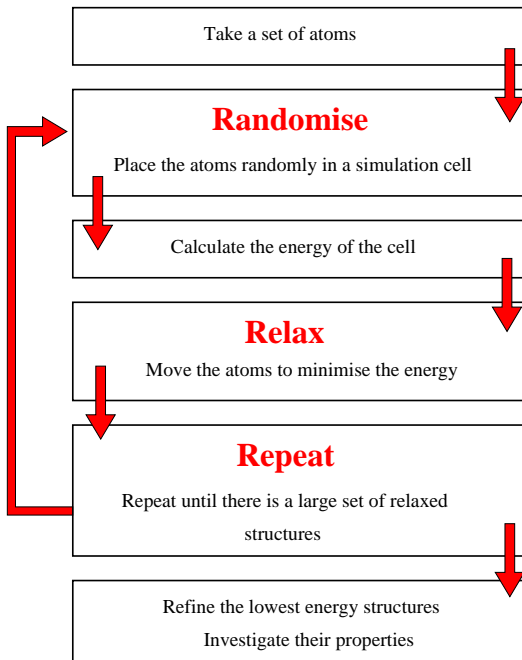


Figure 6.7: The Random Structure Searching Algorithm.

can be improved by imposing one or more constraints. The constraints typically employed are to,

(i) choose the initial positions of a local minimum and randomly displace the atoms by a small amount. This method is still to be fully investigated;

(ii) insert “chemical units” (for example molecules) at random rather than atoms.

The example given in [140] is that of H_2O . It is possible to add atomic H and O into a cell, in a ratio of 2:1, but this causes H_2 to form, which will not dissociate in the subsequent minimisation to form the required H_2O . It is more sensible then, to add H_2O molecules randomly from the beginning, again rejecting if two molecules have a significant overlap;

(iii) search within structures of a particular space group symmetry. The material is allowed to form higher symmetry structures, but cannot break from the (minimum) imposed symmetry throughout the calculation (except by calculational inaccuracy);

(iv) constrain the initial positions of some atoms. For example, if we wish to model defects in graphite, we would *constrain* the initial positions of carbon atoms

into layers.

- (v) co-ordination and bond angle constraints. For example, make sp^2 or sp^3 bonded carbon atoms.

We note that when using constraints of type (i), (ii), (iv) and (v), once the force minimisation begins, the algorithm is free to break any of the initial constraints, if it is energetically favourable to do so. Hence the constraints are more of an initial guide to the area of configuration space that needs searching and not a rule (except in the case of constraint type *iii*).

It seems strange that such a simple method has not been applied before. We believe that this method has been tried many times in the past with little success, for which we propose two reasons. Firstly, the method depends heavily on the quality of the initial search calculations. If 95 % of these calculations are to be thrown away it is natural for the user to make these calculations as computationally light as possible. This leads to the sampling of the wrong energy landscape and hence the inability to find an accurate ground state.

Secondly, it is only recently that electronic structure computer codes have become mature enough to be remotely set off thousands of times, without frequent instabilities occurring. In practice, with the planewave DFT code CASTEP, the vast majority of random searches set off come to a local minima on the energy surface and there are no issues with non-convergence.

In comparison to the GA method, AIRSS has also discovered many new phases of extensively studied solids, at a fraction of the algorithmic complexity. In their first paper, Pickard and Needs applied the AIRSS technique to high-pressure phases of silane [141]. They demonstrated that the AIRSS method works well by performing tests on silicon at zero pressure. They correctly found the diamond structure and three experimentally verified high pressure phases. In another test, important for Chapter 8, they showed that AIRSS can recover the two lowest energy self-interstitial defects in silicon. They concluded that there is a metallic phase of silane that could be obtained experimentally. This phase may be candidate for high temperature superconductivity. The high-pressure insulating $I4_1/a$ phase predicted in this paper

has been observed in the recent X-ray diffraction studies of Eremets *et al.*[142].

They also predicted a new phase of aluminium hydride [143] that is metallic at sufficiently low pressures to be formed in diamond-anvil-cell experiments. The high-pressure metallic $Pm\bar{3}n$ phase predicted in this paper has been observed in the recent x-ray diffraction studies of Goncharenko *et al.*[144]

Pickard and Needs have applied the AIRSS method to a range of other high-pressure problems such as how calcium interlocates between graphite sheets [145]: how hydrogen bonds at high pressure [146]: new phases of H_2O [147], and interesting new phases of ammonia [148] that form the rather unexpected $NH_2^- + NH_4^+$ ionic molecular crystals rather than a homogenous mix of NH_3 .

In our opinion, the merit in the random structure method is fourfold:

- it uses the great strength of DFT, the ability to relax to a local minimum in the energy surface using *ab initio* calculations;
- it has few parameters whose values need to be set;
- it is easy to apply constraints in a sensible way;
- it is easy to adapt the algorithm to new techniques such as defects, surfaces, *etc.*

6.3 Summary

In this chapter a range of different methods for finding the global minimum of an energy surface have been discussed. The concept of a temperature as a guiding parameter plays heavily in simulated annealing which, through the new developments of parallel tempering, may turn out to be a very useful technique. Genetic algorithms, a very biological approach to solving the global minimum problem, have also been discussed. Again we have seen that this method has scope for finding new structures.

Finally, we discussed random structure searching, the simplest of the three methods. The successes of this method were discussed in some detail. We see that the

method has much scope and could be modified for other classes of structures. The application of the AIRSS method to defects in semiconductors is the topic of Chapter 8.

Chapter 7

Point Defects

Like human defects, those of crystals come in a seemingly endless variety, many dreary and depressing, and a few fascinating.

“Solid State Physics”, Neil W. Ashcroft and N. David Mermin,
Brooks/Cole, 1976

7.1 Introduction

IN THIS CHAPTER a brief overview of point defects is presented. We outline how they are detected experimentally by their vibrational or electronic properties since there is no X-ray diffraction method to determine their structures. Finally, we discuss how to predict theoretically these defect properties using *ab initio* techniques.

Firstly, it should be understood that point defect refers to a local deviation from the perfect crystal lattice. Defect is somewhat of a misnomer since the presence of defects can produce beneficial as well as detrimental properties in the bulk crystal. Point defects come in many different forms; the description below also serves to define the nomenclature of the field. At finite temperatures, vacancies and interstitials are

to be found in a lattice at equilibrium. Vacancies, denoted $\{V\}$, are where an atom is missing from a lattice site, and the presence of a vacancy can also cause a rearrangement of atoms on neighbouring lattice sites, moving them from their perfect lattice positions. Interstitial defects, denoted $\{I\}$, form when there are more atoms present in a given part of crystal than there are lattice sites. The extra atoms are located in the voids between crystal sites or they can share crystal sites with other atoms – known as *split-interstitials*. An interstitial of the same type of atom as the host crystal is known as a *self-interstitial*. For crystals containing more than one type of atom, such as ZnO or GaAs, anti-site defects form when an atom of type A, sits on a site of type B. Finally, we refer to a defect that contains more than one type of atom, as a *complex*.

Perhaps the earliest use of defects was when stone-age man found that he could harden copper by adding trace amounts of tin; thus the Bronze age began. Much more recently, a similarly profound discovery of adding small amounts of group III or group V elements to silicon and germanium has brought about a revolution in electronics. The resulting p-type and n-type materials are the constituents of all semiconductor diodes and transistors. Defects can also have a harmful effect on semiconductor devices. Hydrogen, oxygen, nitrogen molecules &c. readily enter the crystal bulk during device manufacture. The atoms can easily bind to the n- and p-type dopants inhibiting their electrical activity.

Defects are also solely responsible for electrical conductivity in ionic solids, and are the cause of colours in many crystals. Defects called *colour centres* form optical absorption lines which appear in the optically forbidden band of the host crystal. This gives many gemstones their characteristic colour.

7.2 Experimental Methods

It seems as if there is a never-ending set of acronyms referring to the different spectroscopies which can be used for defect analysis. There are the electron-probe-based spectroscopies ELNES/EELS and DLTS: the X-ray spectroscopies EXAFS/XANES along with positron annihilation and photoluminescence studies. All of these meth-

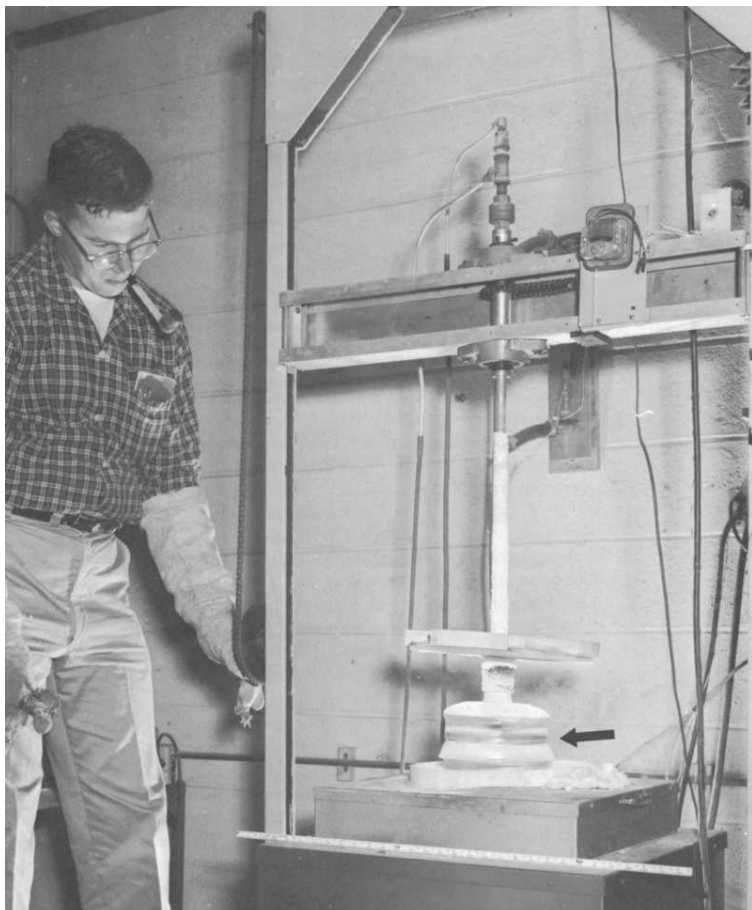


Figure 7.1: The Czochralski Process, [*Introduction to Solid State Physics, 3rd ed., Charles Kittel, John Wiley, 1968.*] A single crystal of Cesium Iodide (black arrow) is pulled from the molten cesium iodide in the crucible beneath. Defects from nitrogen, oxygen and hydrogen molecules in the air readily enter these crystals during manufacture. This author believes that the pipe-smoke will not help the purity of the crystal much either!

ods being out of the scope of this brief introduction to defect analysis.

From the experimental and theoretical body of literature in the next chapters, vibrational studies and electron-paramagnetic-resonance (EPR) imaging are by far the most widely used. We discuss these experimental techniques a little more below.

7.2.1 Vibrational Spectroscopies

At finite temperature atoms are not fixed at their lattice sites: they vibrate around them. These vibrations propagate disturbances called *phonons* throughout the bulk.

When a defect is present in the crystal, it too will vibrate, but at different frequencies to those of the phonon modes of the bulk. These defect vibrations, may be localised around the defect and its nearest-neighbours and hence are called *local vibrational modes* (LVM). The LVM experiments are sensitive to LVM frequencies higher than the phonon modes of the host crystals. The LVM can be studied by measuring what frequencies of IR are absorbed by the bulk containing the defects. If different isotopes of the same impurity atoms are used, they will have different LVM, helping to characterise the defect.

One such method of measuring the LVM of defects is Fourier-transform infrared spectroscopy (FTIR). The sample is irradiated with IR and a detector measures the frequencies which are absorbed and their intensities. Subtracting the absorption intensities of the host crystal without the defect leaves the absorbed intensities that correspond to the LVM of the defects within the crystal. Monochromatic IR sources are expensive, so FTIR instead produces an *interferogram* from a non-monochromatic source, using a Michelson interferometer. In the interferometer the relative phase of the two IR paths through the interferometer is slowly changed. This results in a complicated absorption pattern at the detector which is then Fourier transformed to find the individual absorbed frequencies.

An alternative approach is Raman spectroscopy. Here monochromatic photons are inelastically scattered by the crystal. The incoming photon excites the system to a virtual energy level. The system then decays to an excited vibrational state of the system, emitting a photon in the process. The frequency change between the two

photons is equal to the excited state energy level. Since elastic (Rayleigh) scattering is the dominant process, very sensitive detectors are necessary to detect the Raman scattered photons.

7.2.2 Electron Paramagnetic Resonance Imaging

Electron Paramagnetic Resonance imaging (EPR), also known as electron spin resonance imagining, may be used whenever there are unpaired electrons in the system. It works by the Zeeman-splitting of electron energy levels when a sample is placed in a magnetic field. Microwave radiation of frequency v is shone on a sample as an external magnetic field \mathbf{B} is slowly varied. A sharp peak is detected in the derivative of the microwave absorption, whenever $hv = \Delta E$, where ΔE is the energy of the Zeeman-split states and h is Planck's constant. The Zeeman-splitting energy is $\Delta E = g\mu_B\mathbf{B}$, where μ_B is the Bohr magneton and g the dimensionless magnetic moment (or g -factor).

Further information can be obtained by studying the hyperfine splitting of these peaks. The hyperfine splitting is caused by the interactions between electronic and nuclear spins.

7.3 Ab initio Quantities

It seems that most of the methods mentioned above can be calculated using *ab initio* techniques.

Information about vibrational modes of solids can be obtained within density-functional perturbation theory (DFPT) within the harmonic approximation. See the review article by Baroni *et al.*[149]. Atoms are assumed to experience a force proportional to their displacement from their equilibrium position. From the knowledge of the second-derivatives of the total energy, the matrix of the interatomic force constants, \mathbf{C} can be derived between atoms κ and κ' . After Fourier transforming \mathbf{C} and dividing by $\sqrt{M_\kappa M_{\kappa'}}$ we obtain the dynamical matrix $\tilde{\mathbf{D}}$, where M_κ and $M_{\kappa'}$ are the masses of atoms κ and κ' respectively. The eigenvalues of matrix $\tilde{\mathbf{D}}$ are the squares of the phonon frequencies and the eigenvectors are the normal modes of

the solid. The intensities of the IR-active modes are then calculated from a knowledge of the electric dipole moments of the system. Raman-scattering intensities are more difficult to calculate, and involve third-derivatives of the total energy. See for example the derivation in Porezag *et al.*[150].

EELS/ELNES spectra may be calculated using CASTEP[151], since for high-energy electrons the electron energy loss function is proportional to the imaginary part of the dielectric function [152]. One of the early studies showed excellent agreement between experimental and theoretical spectra[153] for cubic boron nitride.

The EPR g tensor arises from modelling the EPR spectrum using the following Hamiltonian,

$$\hat{H}_{\text{eff}} = \frac{\alpha}{2} \mathbf{S} \cdot \mathbf{g} \cdot \mathbf{B} + \sum_I \mathbf{S} \cdot \mathbf{A}_I \cdot \mathbf{I}_I, \quad (7.1)$$

where α is the fine-structure constant, \mathbf{S} is the total electron spin, \mathbf{I}_I is the nuclear spin of nuclei I , \mathbf{B} is the applied uniform magnetic field, \mathbf{A}_I is the hyperfine tensor and \mathbf{g} is a tensor generalisation to 3D of the g -factor in Sec. 7.2.2.

Both \mathbf{g} and the hyperfine interactions described by \mathbf{A}_I are available using DFT [154, 155].

Since none of these techniques have been used within this dissertation, they are not mentioned in any further detail. We merely note that none of the above *ab initio* techniques can be used to study a system until the structure of the defect is known. The rest of the dissertation is dedicated to this goal.

In the following chapters we find the DFT ground-state structures of various defects, but note that this may not be the end of the story. For example, to match a DFT ground-state structure to what is seen in spectroscopies many other factors need to be taken into account, such as kinetic contributions, quantum tunnelling, negative-U behaviour &c. Nevertheless *ab initio* structure determination takes us a fair way to our goal.

Chapter 8

Hydrogen in Silicon

8.1 Introduction

HYDROGEN IS A VERY COMMON impurity in semiconductors whose roles in silicon include passivating surfaces and defects [156]. Much is known about the vacancy in silicon but rather little understanding of self-interstitials has been gleaned from experiments, so there is considerable reliance on theoretical work. Self-interstitials are common in silicon and they are expected to react with impurities to form defect complexes. Mobile hydrogen atoms are expected to bind strongly to self-interstitial defects in silicon, and hydrogen-silicon complexes have been detected in experiments [157].

Silicon self-interstitials are readily formed during device manufacture and bombardment with electrons or ions. According to DFT calculations, the most stable structure is the split- $\langle 110 \rangle$ defect, with the hexagonal interstitial being slightly higher in energy and the tetrahedral interstitial being still higher in energy [158, 159, 160]. The results of two quantum Monte Carlo calculations are consistent with these three defects having low energies [160, 161]. Mukashev *et al.*[162] attributed the AA12 electron paramagnetic resonance centre to a self-interstitial defect, possibly a single self-interstitial. Calculations by Eberlein *et al.*[163] found the doubly-positively-charged single self-interstitial to be stable at the tetrahedral site, and that it was broadly consistent with the AA12 defect.

Much of what is known about hydrogen in silicon has been learnt from studies of vibrational modes which are accessible to infrared absorption experiments and may also be calculated within first-principles methods. Only one hydrogen-silicon complex has so far been firmly identified in experiments. Budde *et al.*[157] identified the silicon self-interstitial with two hydrogen atoms using Fourier transform infrared (FTIR) absorption spectroscopy. The observed properties were found to be in excellent agreement with the results of DFT calculations [157].

Throughout this dissertation we denote the silicon self-interstitial atom by I and the n hydrogen atoms by H_n , and the whole defect is referred to as $\{I, H_n\}$. A metastable defect is indicated by an asterisk. We also use the notation devised by Gharaibeh *et al.*[38] where $(n)-(m)\cdots$ means n hydrogen atoms bonded to one silicon atom and m hydrogen atoms bound to a neighbouring silicon atom, *etc.* For example, the silicon self-interstitial bonded to two hydrogen atoms mentioned above is referred to as $\{I, H_2\}$ and the arrangement of H atoms shown in Fig. 8.3 is described as (1)-(1).

The first calculations we are aware of on the $\{I, H\}$ defect were by Déak *et al.*, [164] who reported two possible structures which, however, are different from those found subsequently by Van de Walle and Neugebauer [165]. In each structure found by Déak *et al.*[164] the second nearest neighbour silicon atom to the hydrogen has a dangling bond, whereas Van de Walle and Neugebauer's lowest energy structure does not contain dangling bonds. Budde *et al.*[157] found $\{I, H\}$ structures based on split- $\langle 110 \rangle$ and split- $\langle 100 \rangle$ self-interstitials both of C_{1h} symmetry, with the $\langle 110 \rangle$ defect being 0.24 eV lower in energy. The $\{I, H\}$ defect based on the split- $\langle 110 \rangle$ interstitial was similar to that found by Van de Walle and Neugebauer[165] whereas the split- $\langle 100 \rangle$ is similar to the lowest energy structure of Déak *et al.*[164] Gharaibeh *et al.*[38] found a structure similar to Van de Walle and Neugebauer's[165] lowest energy defect.

Déak *et al.*[164, 166] also studied the $\{I, H_2\}$ defect. Their lowest energy $\{I, H_2\}$ defect is also based on a split- $\langle 110 \rangle$ self-interstitial with its two dangling bonds terminated by hydrogen atoms. Further evidence in favour of this structure has been obtained in a variety of studies [165, 157, 167, 38]. Gharaibeh *et al.*[38] also

found this to be the most stable of the $\{I, H_n\}$ family of defects.

Hastings *et al.*[167] studied the $\{I, H_3\}$ defect within Hartree-Fock (HF) theory, finding a structure with two hydrogen atoms bonded to a silicon and a third bonded to a neighbouring silicon, *i.e.*, a (2)-(1) configuration of hydrogen atoms. They found interstitial silyl (SiH_3) to be 0.44 eV higher in energy and concluded that it is unlikely to be found in bulk silicon. More complete DFT calculations by the same group [38] found a $\{I, H_3\}$ defect with a (1)-(1)-(1) configuration.

Hastings *et al.*[167] studied the $\{I, H_4\}$ defect within HF theory, finding a ground-state structure similar to the $\{I, H_2\}$ defect, but with additional hydrogen atoms bonded to the nearest-neighbour and second-nearest-neighbour silicon atom to the self-interstitial, resulting in a (1)-(1)-(1)-(1) configuration. They also found a metastable (2)-(2) configuration 0.2 eV higher in energy and showed that interstitial silane (SiH_4) is very unlikely to form. A later DFT study by the same group [38] found the ground state of $\{I, H_4\}$ to be a (3)-(1) configuration.

In this chapter we present calculations for the defects $\{I, H_i\}$, $i = 1, 4$, as found by the AIRSS approach using first-principles DFT methods. We describe the modifications to the random structure searching scheme in Sec. 8.2.1. The non-standard Brillouin-zone integration scheme we have used has already been described in Sec. 2.7.5, and the details of our DFT calculations and some convergence tests were discussed in detail in Sec. 2.7.2. Our results are described in Sec. 8.4 and our main conclusions are summarised and discussed in Sec. 8.6.

8.2 Computational Approach

8.2.1 Random Structure Searching

We have already discussed in Chapt. 6 that “Random structure searching” has been proven to be a powerful tool for finding structures of solids under high pressures [141, 145, 146, 147, 143]. The basic algorithm is very simple: we take a population of random structures and relax them.

Pickard and Needs [141] showed that “random structure searching” can be ap-

plied to finding structures of defects. In the current chapter we have searched for silicon self-interstitial defect structures using a 32-atom body-centred-cubic unit cell of diamond-structure silicon. The initial configurations were generated by removing an atom and its four nearest neighbours, making a “hole” in the crystal, and placing six silicon atoms at random positions within the hole. The initial configurations therefore consisted of a region of perfect crystal and a defect region in which atoms are positioned randomly. This is an example of a constraint of type (*iv*) mentioned in Chapt. 6. Relaxing the members of an ensemble of such initial configurations generated the split- $\langle 110 \rangle$, tetrahedral and hexagonal interstitial configurations, which various DFT calculations have shown to be lowest in energy [157, 158, 159, 168, 169].

We explored four choices of the hole used to generate the initial configurations: (*a*) remove one silicon atom and its four nearest neighbours; (*b*) remove one silicon atom; (*c*) do not remove any silicon atoms and take the centre of the hole to lie at the hexagonal site; (*d*) the same as (*c*) but with the hole at the tetrahedral site. The initial configurations were generated by placing the appropriate atoms randomly within cubic boxes of sizes ranging from 2 to 6 Å centred on the hole. Choices (*b*), (*c*), and (*d*) generally led to us finding the structure we believe to be most stable within roughly 100 random searches, while the larger hole of choice (*a*) was less successful and sometimes failed to find the ground state within 500 searches.

8.2.2 Density-Functional-Theory Calculations

Our calculations were performed using the Generalised Gradient Approximation (GGA) density functional of Perdew, Burke and Ernzerhof (PBE) [170]. The planewave basis-set code CASTEP [35] was used with its built-in ultrasoft [36] pseudopotentials which include non-linear core corrections [171]. All of the results presented here were obtained with non-spin-polarised calculations. Some searches and large supercell calculations were repeated allowing spin-polarisation, but no significant changes were found in the energy differences between structures. For the case of the bond-centred hydrogen atom in 32 atoms of silicon we performed calculations with and without spin polarisation. The difference in total energies were ~ 0.0003 eV, which was much less than the accuracy required. Hence the remainder of the chapter uses

non-spin polarised calculations for speed, however we duly note that spin polarisation can play a crucial part in some kinds of defect. The defects were treated as metals at a kT of 0.2 eV which corresponds to a temperature of ~ 2300 K.

We carried out convergence tests on the formation energy of a bond-centred hydrogen atom in silicon from interstitial H₂ using 256-atom silicon cells as discussed in Sect. 2.7.2. We define the formation energy, E_f , of a bond-centred H in silicon from interstitial H₂ calculated with N -atom silicon cells as

$$E_f(H_{bc}, N) = E(H_{bc}, N) - \frac{E(H_2, N)}{2} - \frac{E(N)}{2}, \quad (8.1)$$

where $E(X, N)$ is the energy of the X defect in a N -atom silicon cell, and $E(N)$ is the bulk energy for N atoms.

The Fourier transform grid used for wavefunction manipulation was set to integrate, without aliasing, frequencies twice as high as the maximum frequency in the basis set. We checked the convergence of $E_f(H_{bc})$ with respect to the charge augmentation grid required for the ultrasoft pseudopotentials, finding it to be converged to within 0.005 eV at 2.75 times the maximum frequency in the orbital basis set. We found that $E_f(H_{bc})$ was converged to within ± 0.02 eV with a basis set of $E_{PW} = 230$ eV.

We tested different k-point sampling schemes in the 256-atom cell. The values of $E_f(H_{bc})$ for the $n = 3$ standard MP and Multi-B grids agreed to within 0.002 eV and we therefore considered these to be converged. The value of $E_f(H_{bc})$ calculated for the 256-atom cell with the $n = 2$ standard MP grid differed from the converged result by ~ 0.04 eV, whereas the error from the Multi-B grid was six-times smaller.

8.3 Calculating the Formation Energies

The searches were performed using a body-centred-cubic supercell of a size to contain 32-atoms of bulk silicon. We used a $n = 2$ Multi-B k-point grid, which we estimate gives energy differences between structures converged to within 0.006 eV. However, the 32-atom cell is too small to give highly accurate geometries and for-

Defect	$E_f(\{I\})$ (eV)
Split- $\langle 110 \rangle$	3.66
Hexagonal	3.69
Tetrahedral	3.96

Table 8.1: Formation energies for self-interstitial defects in 256-atom cells of silicon, as defined by Eq. (8.2).

mation energies. We therefore embedded the most promising structures within 256-atom body-centred-cubic unit cells and relaxed using a $n = 2$ Multi-B grid until the forces on each atom were less than $0.001 \text{ eV}\text{\AA}^{-1}$.

The formation energy of the self-interstitial is defined as

$$E_f(\{I\}, N) = E(\{I\}, N) - \frac{N+1}{N} E(N), \quad (8.2)$$

where $E(\{I\}, N)$ is the energy of the self-interstitial cell.

We define the formation energy per hydrogen atom of a system containing a defect with n hydrogen atoms and i silicon atoms relative to a system containing i isolated self-interstitial defects and $n/2$ interstitial hydrogen molecules as,

$$\begin{aligned} E_f(\{I_i, H_n\}, N) &= \frac{E(\{I_i, H_n\}, N) - E(\{I_i\}, N)}{n} + \\ &\quad \frac{E(N) - E(H_2, N)}{2}. \end{aligned} \quad (8.3)$$

Note that Eq. (8.3) with $i = 0$ and $n = 1$ gives Eq. (8.1) for the formation energy of bond centred hydrogen.

8.4 Results

The formation energies of self-interstitial defects as defined by Eq. (8.2) are given in Table 8.1. In agreement with numerous previous studies [157, 158, 159, 168, 169] we find the most stable defect to be the split- $\langle 110 \rangle$ interstitial. The hexagonal and tetrahedral interstitials are 0.03 eV and 0.3 eV higher in energy, respectively. Hence all three self-interstitial defects are candidates for forming a low energy $\{I, H_n\}$ defect in the presence of hydrogen.

Defect	Configuration	E_f per H atom (eV)	Degeneracy d_i
H_2	Molecule	0.00	3
H_2^*	(1)-(1)	0.10	-
H_{bc}	Bond Centre	1.04	-

Table 8.2: Formation energies per H atom and degeneracies per atomic site, d_i , of hydrogen defects in silicon. The H_2 is the lowest in energy defect.

Defect	Configuration	E_f per H atom (eV)	Degeneracy d_i
$\{I, H\}$	(1)	-0.53	4
$\{I, H\}^*$	(1)	-0.39	-
$\{I, H_2\}$	(1)-(1)	-0.69	12
$\{I, H_2\}^*$	(2)	-0.61	-
$\{I, H_3\}$	(2)-(1)	-0.39	24
$\{I, H_3\}^*$	(1)-(1)-(1)	-0.34	-
$\{I, H_4\}$	(1)-(2)-(1)	-0.48	24

Table 8.3: Formation energies per H atom as defined by Eq. (8.3) and degeneracies per atomic site, d_i , for various hydrogen/silicon self-interstitial complexes. The formation energies are represented pictorially in Fig. 8.1. We note that these formation energies are without zero-point energy corrections. They serve as a comparison between our ground state structures and the DFT results in the literature.

Our search for hydrogen defects in bulk silicon found the lowest energy defects known previously, but no new defects. We found the bond centred H atom, the H_2 molecule with the H-H bond pointing along a $\langle 100 \rangle$ direction, and the H_2^* metastable defect of Chang and Chadi [172]. The formation energies of hydrogen defects in silicon given in Table 8.2 show the H_2 molecule to be the most stable, as found in previous calculations [173, 174, 175], with the H_2^* defect and bond-centred-hydrogen being respectively 0.10 eV and 1.04 eV per H atom higher in energy.

The formation energies of the hydrogen/silicon self-interstitial complexes are calculated with reference to a system containing the most stable self-interstitial (the split- $\langle 110 \rangle$) and the most stable hydrogen defect in pure silicon, the H_2 molecule. The data in Table 8.3 shows that the $\{I, H_2\}$ defect has the lowest formation energy, followed by the $\{I, H_2\}^*$. These data are shown in pictorial form in Fig. 8.1.

Our searches for the $\{I, H\}$ defect found the previously-known structure [165, 38] of C_s symmetry, but we also found a new lower-energy structure of higher C_{3v} symmetry. The C_{3v} defect is 0.14 eV lower in energy and is based on a hydrogen

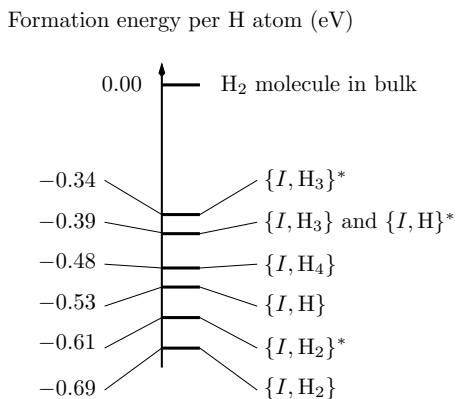


Figure 8.1: Formation energies per hydrogen atom using Eq. (8.3) for various hydrogen defects in silicon calculated with respect to silicon containing a self-interstitial defect and silicon containing hydrogen molecules.

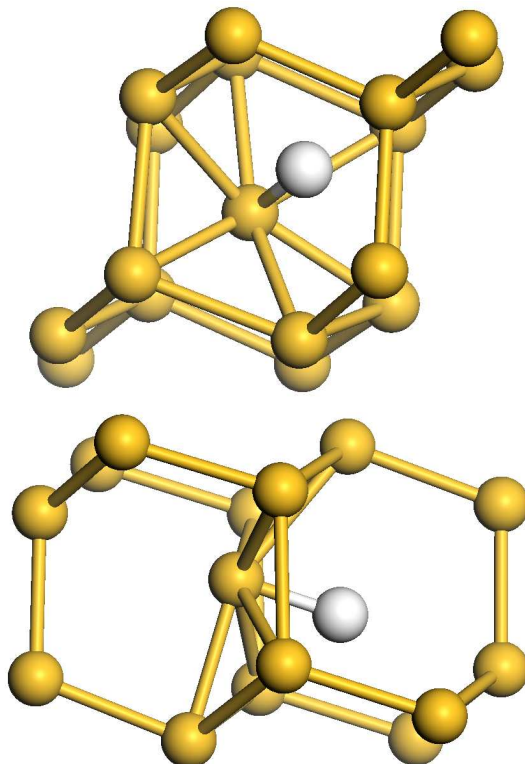


Figure 8.2: Two projections of the new $\{I, \text{H}\}$ defect of C_{3v} symmetry found in this work. Silicon atoms are shown in yellow and the hydrogen atom is white. This defect is based on a hexagonal self-interstitial rather than the split- $\langle 110 \rangle$ self-interstitial of previous work.

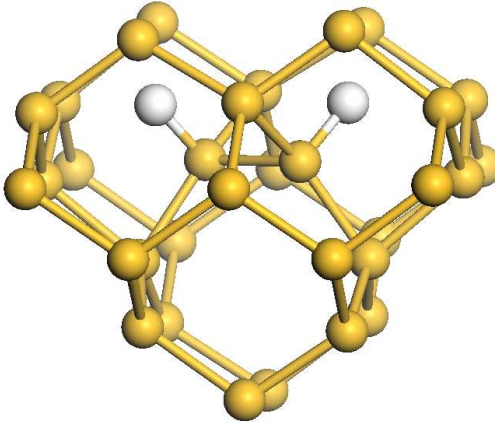


Figure 8.3: The most stable $\{I, H_2\}$ defect which has C_2 symmetry and was also found in previous work [164, 166, 165, 38, 157, 167]. Silicon atoms are shown in yellow and the hydrogen atoms are white. The defect is based on a split- $\langle 110 \rangle$ silicon interstitial defect, with hydrogen atoms saturating the two dangling bonds.

atom bonded to a hexagonal self-interstitial with the Si-H bond pointing along a $\langle 111 \rangle$ direction, rather than the split- $\langle 110 \rangle$ interstitial on which the C_s $\{I, H\}$ defect is based.

Our searches found the $\{I, H_2\}$ (1)-(1) defect structure reported previously[164, 166, 165, 38, 157, 167] which is shown in Fig. 8.3 and whose formation energy we calculated to be -0.69 eV/H. The second most stable $\{I, H_2\}$ defect, which has a (2) structure, is the $\{I, H_2\}^*$ defect found previously by Déak *et al.*[164] and is shown in Fig. 8.4. This defect is based on a buckled bond-centred Si atom with two H atoms saturating its dangling bonds. The $\{I, H_2\}$ and $\{I, H_2\}^*$ both have C_2 symmetry. Hastings *et al.*[167] found $\{I, H_2\}^*$ to be 0.40 eV higher in energy than $\{I, H_2\}$ within HF theory. Later Gharaibeh *et al.*[38] found it to be 0.05 eV above the ground state. Our calculations gave an energy 0.08 eV/H higher than the $\{I, H_2\}$ of Fig. 8.3.

The lowest energy $\{I, H_3\}$ defect we found is a (2)-(1) configuration of C_1 symmetry, which is shown in Fig. 8.5 and has a formation energy of -0.39 eV/H. This defect has the same configuration of hydrogen atoms but a different structure to the one found by Hastings *et al.*[167] using HF theory. They also found a metastable $\{I, H_3\}^*$ structure of C_1 symmetry with a (1)-(1)-(1) configuration just 0.1 eV higher in energy. However, more recently this group have used DFT methods and found

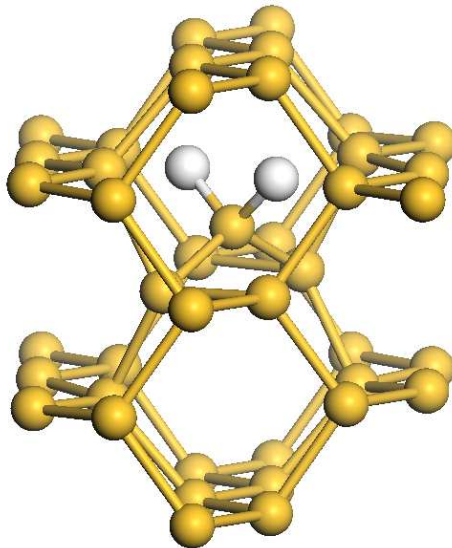


Figure 8.4: The second most stable $\{I, H_2\}^*$ defect which has C_2 symmetry and was also found in previous work [164]. Silicon atoms are shown in yellow and the hydrogen atoms are white. The defect is based on a buckled bond-centred silicon self-interstitial.

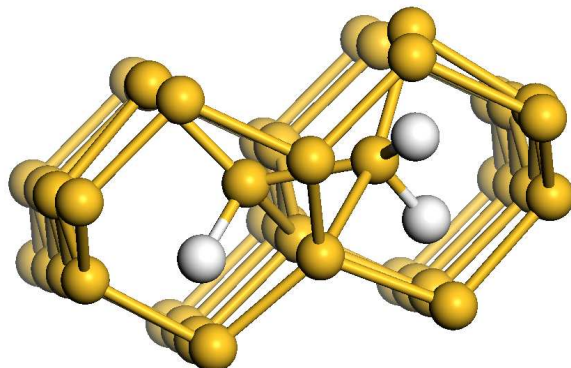


Figure 8.5: The new $\{I, H_3\}$ defect of C_1 symmetry found in this work. Silicon atoms are shown in yellow and the hydrogen atoms are white. The defect is based on a deformed split- $\langle 110 \rangle$ self-interstitial.

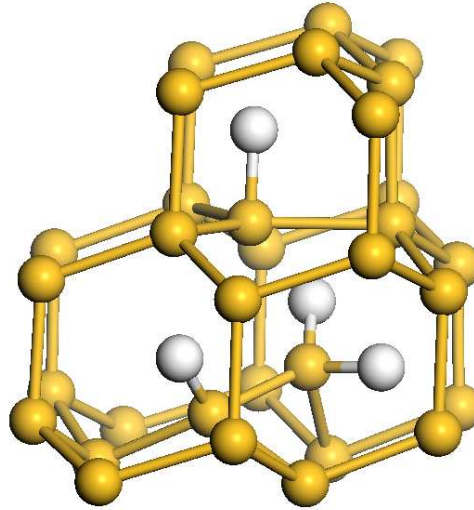


Figure 8.6: The new $\{I, H_4\}$ defect of C_1 symmetry found in this work. Silicon atoms are shown in yellow and the hydrogen atoms are white. It is based on the new $\{I, H_3\}$ (see Fig. 8.5) with a defect similar to the H_1^* defect of Chadi [176] adjacent to it on the anti-bonding site.

the (1)-(1)-(1) configuration to be lower in energy than a (2)-(1) configuration [38]. We find both the new (2)-(1) and (1)-(1)-(1) configurations mentioned above, with the new one being 0.05 eV/H lower in energy than the (1)-(1)-(1).

The most stable $\{I, H_4\}$ defect we found, shown in Fig. 8.6, is made up from the $\{I, H_3\}$ defect of Fig. 8.5 with a defect similar to the H_1^* adjacent to it at the anti-bonding-type site as shown by Chadi [176]. This $\{I, H_4\}$ defect has a (2)-(1)-(1) configuration and C_1 symmetry. Our $\{I, H_4\}$ defect is different from the lowest energy one found by Hastings *et al.* [167] within HF theory, which has a (1)-(1)-(1)-(1) configuration. We have not been able to obtain the lowest energy $\{I, H_4\}$ structure from Gharaibeh *et al.*'s paper [38], although from the description given, we know that it is different from ours. We are therefore unable to perform a full comparison of energies for $\{I, H_4\}$.

8.5 Relative Abundances

The relative abundances of the defects at zero temperature can be calculated from the defect energies as a function of the ratio of the concentrations of the self-

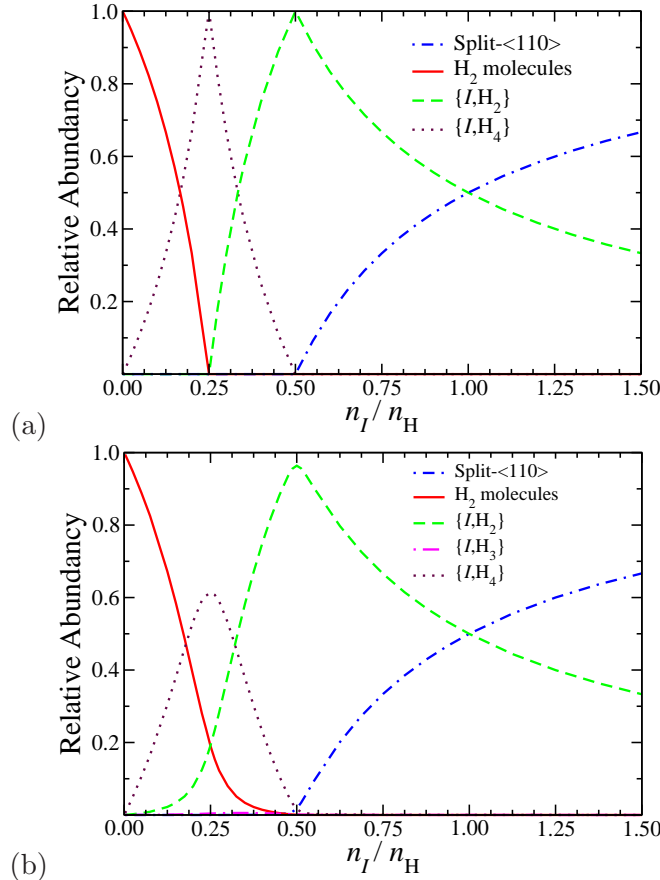


Figure 8.7: Relative abundances of the defects at zero temperature (a) and 1200 K (b). n_I/n_H is the ratio of the concentration of interstitial silicon atoms to hydrogen atoms. At low n_I/n_H there is a large relative abundance of H_2 molecules. As n_I/n_H increases, H_2 molecules bind strongly to the Si self-interstitials, forming $\{I, H_4\}$ defects. As n_I/n_H increases further, formation of $\{I, H_2\}$ defects is favoured. However, an increase in n_I/n_H above 0.5 does not lead to formation of $\{I, H\}$, because the mixed state of $\{I\}$ and $\{I, H_2\}$ is more favourable. The most significant differences at 1200 K are that the abundance of $\{I, H_4\}$ is somewhat reduced and that H_2 and $\{I, H_2\}$ defects are favoured instead, and $\{I, H_3\}$ has a small but finite abundance in a region which peaks at around $n_I/n_H = 0.4$. The abundance of $\{I, H\}$ at 1200 K is negligible.

Cell	Bulk	H	I	Concentration	Energy
256 Si	1	0	0	n_1	E_1
256 Si + Split-<110>	1	0	1	n_2	E_2
256 Si + H ₂	1	2	0	n_3	E_3
256 Si + {I, H ₁ }	1	1	1	n_4	E_4
256 Si + {I, H ₂ }	1	2	1	n_5	E_5
256 Si + {I, H ₃ }	1	3	1	n_6	E_6
256 Si + {I, H ₄ }	1	4	1	n_7	E_7

Table 8.4: Linear programming constraint table – Each 256-atom cell is given parameters according to the number of different types of atom it contains, B, H, and I. These correspond to Bulk, Interstitial (silicon) and Hydrogen. These parameters are used as the constraints for the linear program. Note that we count the bulk atoms as 1 not 256 for ease. As all cells have the same number of bulk atoms, n_B is a normalisation factor only.

interstitial and hydrogen atoms, n_I/n_H . The solution to this problem is a simple linear program, which is outlined below.

We take the energies of all the possible cells, and label them with the number of bulk, interstitial silicon, and interstitial hydrogen atoms they contain, see Table 8.4.

Next we define an energy cost function, E_{Cost} , which is the energy of the system for a given set of concentrations of defects,

$$E_{\text{Cost}} = \sum_{i=1}^7 n_i E_i, \quad (8.4)$$

and minimise E_{Cost} using the following linear constraints,

$$\begin{aligned} n_B &= n_1 + n_2 + n_3 + n_4 + n_5 + n_6 + n_7, \\ n_I &= n_2 + n_4 + n_5 + n_6 + n_7, \\ n_H &= 2n_3 + n_4 + 2n_5 + 3n_6 + 4n_7, \end{aligned}$$

which conserve the number of silicon interstitials n_I , number of hydrogen atoms n_H and number of bulk cells n_B .

Fig. 8.7 (a) shows that only four defects form in this model, {I}, {I, H₂}, {I, H₄}, and {H₂}, with the {I} defect corresponding to the lowest-energy split-<110> self-interstitial. The main features of Fig. 8.7 are that when $n_I \ll n_H$ {I, H₄} defects

are formed and the surplus H atoms form $\{H_2\}$ defects, and when $n_I \gg n_H$ $\{I, H_2\}$ defects are formed and the surplus Si atoms form $\{I\}$ defects.

At finite temperatures, see Fig. 8.7 (b), we consider the defect free energies, which should contain contributions from the vibrational free energy and the configurational entropy. We have not evaluated the vibrational free energies, which would involve costly phonon calculations, but we have calculated the configurational contributions. These are expected to be significant because we deal with defects containing from one atom (split- $\langle 110 \rangle$ self-interstitial) up to five atoms ($\{I, H_4\}$). In general, defects containing fewer atoms are expected to be favoured by the configurational entropy at higher temperatures. In this finite temperate case, it is the Helmholtz free energy, \tilde{E}_{Cost} , that must be minimised, subject to the same constraints as the zero temperature case.

$$\tilde{E}_{\text{Cost}} = \sum_{i=1}^7 n_i E_i - k_B T \sum_{i=1}^7 \ln \left(\frac{n_B! d_i^{n_i}}{(n_B - n_i)! n_i!} \right), \quad (8.5)$$

where k_B is the Boltzmann constant, T is the temperature, n_i is the number of defects per lattice site, n_B is the number of lattice sites and d_i the degeneracy per lattice site.

The degeneracy d_i can be evaluated straightforwardly in some cases. For example, the $\{I, H\}$ defect of Fig. 8.2 has a degeneracy per atomic site of four because it is formed from a Si atom at a hexagonal site (of which there are two per atomic site) and the Si-H bond can point in one of two directions. Calculating the degeneracy for more complicated defects is not necessarily straightforward, and therefore we have developed a computational scheme to evaluate defect degeneracies. The scheme comprises the following steps:

- (i) Generate a set of structures by applying the symmetry operations of the space group of the host crystal to the defect structure;
- (ii) Identify structures from this set which differ only by a translation vector of the lattice of the host crystal and remove all but one of them;
- (iii) The defect degeneracy per primitive unit cell is the number of structures re-

maining.

The defect degeneracies calculated in this fashion are reported in Tables 8.2 and 8.3. Where we present d_i only for the lowest energy defect of each type. The defect concentrations are then obtained by minimising the Helmholtz free energy of the system for fixed concentrations n_I and n_H . In our model we consider only the lowest energy neutral defects of each type listed in Tables 8.2 and 8.3. This is very much a “proof of concept” calculation, in a complete model other defects such as clusters of self-interstitial Si atoms and complexes involving other impurity atoms should be considered along with the metastable defects we discovered, vibrational effects of the defects present and rotational entropies of H_2 ¹.

8.6 Discussion

In this chapter we have presented first-principles DFT results using AIRSS for hydrogen/silicon complexes in silicon. The searches were carried out in 32-atom silicon cells, while the final results were obtained with 256-atom cells. We used a multi-B method to perform the BZ sampling, which we demonstrated to be superior to the standard MP sampling in Chapt. 2.

Formation energies of the defects were calculated with respect to the lowest energy self-interstitial defect and lowest energy hydrogen defect in bulk silicon. We have confirmed that the previously described $\{I, H_2\}$ and $\{I, H_2\}^*$ defects are the most stable. We have, however, found a new $\{I, H\}$ defect which is significantly lower in energy than the one previously reported in the literature. Our defect is based on the hexagonal self-interstitial whereas the previously-reported one was based on the split- $\langle 110 \rangle$ self-interstitial. We also found a new, lower energy, $\{I, H_3\}$ defect and a new $\{I, H_4\}$ defect.

The relative abundances of the defects at zero temperature were calculated as a function of the ratio of the concentrations of the self-interstitial and hydrogen atoms, n_I/n_H . Only four defects can form in this model, $\{I\}$, $\{I, H_2\}$, $\{I, H_4\}$, and $\{H_2\}$, with the $\{I\}$ defect corresponding to the lowest-energy split- $\langle 110 \rangle$ self-interstitial.

¹Which we have treated as static in one of three orientations at the tetrahedral site.

At finite temperatures, we considered the defect free energies. There is little change to the relative abundances in Fig. 8.7, although the abundance of $\{I, H_4\}$ is reduced compared to $\{I, H_2\}$ for similar hydrogen concentrations. This is an effect of taking into account configurational entropy.

It is interesting to note that only the $\{I, H_2\}$, $\{I, H_2\}^*$, and $\{I, H_4\}$ defects are perfectly saturated, *i.e.*, each Si atom has four covalent bonds and each H atom has one, and that these defects have the lowest total formation energies (defined as $nE_F(\{I, H_n\})$ with E_F given by Eq. (8.3)). It is, of course, not possible to achieve perfect saturation of a Si/H structure with an odd number of H atoms, as a saturated structure must contain two bonds per Si atom and half a bond per H atom.

Overall we conclude that “random searching” is a useful tool for finding the structures of low-energy defects in semiconductors.

Chapter 9

Hydrogen / Nitrogen defects in Silicon and Diamond

9.1 Introduction

IN THE PREVIOUS CHAPTER WE applied the AIRSS method to the relatively simple problem of the structures hydrogen/silicon complexes in bulk silicon. Using AIRSS, we recovered all previously-known ground-state defect structures and found some new defects with lower-energy atomic configurations. With AIRSS proven as a useful tool in understanding point-defects, in this chapter we apply it to a more complicated defect problem.

Discovered in 1959, there has been increasing interest in nitrogen defects in silicon due to their ability to improve the physical properties of the crystals [177]. Nitrogen impurities increase the strength of the silicon crystal by immobilising dislocations which reduces warping during wafer processing [178]. The majority of silicon used in electronic devices today is manufactured using the Czochralski process (which we refer to as Cz-Si). In this process a seed crystal is pulled and rotated from a crucible containing molten silicon, to form a silicon crystal at the interface. For high quality samples the float-zone (Fz-Si) method is used. Nitrogen impurities suppress void formation in Fz-Si, whereas in Cz-Si they increase the prevalence of smaller voids. This is important since large voids have been shown to cause gate

oxide failure in devices [179].

Nitrogen is also involved in the so called “ABC” optical centre found in silicon [180]. This centre is stable and appears during annealing at 700°C. It has been suggested that this centre is formed from a pair of substitutional nitrogen atoms, $\{2N_s\}$ ¹ [181]. However, concentrations of $\{2N_s\}$ are low [180] ($\sim 10^{13} \text{ cm}^{-3}$) and FTIR measurements by Stein [182] conclude that substitutional nitrogen makes up only 1% of the total nitrogen content. Stein’s FTIR experiments also agree with the earlier electron paramagnetic resonance (EPR) measurements of Brower *et al.*[183] and Stein concludes that the observed 653 cm^{-1} line is due to a local vibrational mode (LVM) of some kind of substitutional nitrogen centre.

The dominant nitrogen defect in silicon was confirmed as an interstitial pair of nitrogen atoms, $\{2N_i\}$ using a combination of channelling and LVM experiments combined with *ab initio* DFT calculations [184]. Calculations suggest binding energies of the $\{2N_i\}$ defect of between 3.86 and 4.3 eV [185, 186], except for Gali *et al.*[187] who propose 1.73 eV.

There have been many investigations of nitrogen-vacancy defects [186, 185, 181, 188] due to the ability of nitrogen to suppress void formation. Goss *et al.*[181] calculate the formation energy of $\{2N_s\}$ to be 1.6 eV higher than that of $\{2N_i\}$. They note that $\{2N_i\}$ will bind with any number of vacancies, although binding with two vacancies to produce $\{2N_s\}$ is particularly stable. Other works agree and suggest a binding energy for $\{2N_s\}$ of between 3.4 and 3.6 eV [185, 181, 189].

Overall, nitrogen is mobile in silicon although the dominant $\{2N_s\}$ species appears to be immobile. It has been suggested that this species dissociates into smaller, but as yet unspecified, more mobile species [190]. The reaction barriers and pathways of nitrogen propagating in silicon have been studied in detail [191, 192, 193].

Wide band-gap semiconductors have more favourable properties for use in devices than silicon². Diamond is a wide band gap semiconductor (with a gap of

¹We adopt the same nomenclature for defects as in the previous chapter. The number and type of atoms present in the defect are denoted within braces. Substitutional and interstitial forms are differentiated by the suffixes *s* and *i*. Where it is important to differentiate between the defect in silicon or diamond, the host crystal is given as a suffix, *e.g.* $\{2N_s\}_{\text{Si}}$.

²See the figures of merit for different semiconductors in Table 2 of [194].

5.50 eV at room temperature [195]), it has a high carrier mobility, high thermal conductivity and a low dielectric constant. Within the last 20 years it has become possible to produce diamond using chemical vapour deposition (CVD) [196], which has produced very high electron and hole mobilities of 4500 and $3800 \text{ cm}^2\text{V}^{-1}$, respectively [197]. Diamond could potentially be used for many applications requiring high frequency, high power and high-temperature-resistant semiconductors [198].

The problem of doping of diamond is holding back its use in devices. Doping damages the perfect crystal causing self-interstitials and vacancies. These vacancies are very stable. The monovacancy is mobile above 700°C and the divacancy above 1000°C [196]. Vacancies and interstitials can also be produced by irradiation. Diamond has a much smaller lattice constant than silicon (3.557 \AA versus 5.430 \AA at 0°C) and so the vast majority of defects are substitutional.

Diamond crystals are classified according to the quantity of nitrogen they contain. Type I crystals contain nitrogen as an impurity, type II is virtually nitrogen free. Type I crystals are subdivided into Ia and Ib, where Ia is found naturally, and Ib is normally only synthesised. Type Ia is further categorised by the type of nitrogen defect present. Type Ia A contains mainly $\{2N_s\}$ defects, whereas type Ia B contains $\{4N_s, V\}$ defects. Most gem-quality diamond contains both A and B defects and is called type Ia A/B. The synthetic type Ib is dominated by the $\{N_s\}$ defect.

Diamond is *p*-type doped using boron but at present a suitable *n*-type dopant has not been found. Both are necessary before useful devices can be produced. Nitrogen is a possible candidate for *n*-type doping, although $\{N_s\}$ has a donor level at about 1.7 eV [199] below the conduction band, which is too deep to be used in practical applications. The P1 EPR signal has been ascribed to the $\{N_s\}$ substitutional defect [200] which causes a broad IR peak around 1130 cm^{-1} [201]. This defect has trigonal C_{3v} symmetry as deduced from its zero phonon line at 1.945 eV³.

Apart from its potential as a dopant, nitrogen in diamond has other applications. For example, it bonds strongly to dislocations present in the crystal [204]. The $\{N_s, V^-\}$ defect has a number of technological applications. It is a strong candidate

³[202] as referenced in [203].

to be used as a qubit in quantum computing [205, 206]. It is also a stable single-photon source, making it potentially useful in quantum cryptography [207].

We now turn our attention to the behaviour of hydrogen in these semiconductors and its interaction with nitrogen defects. Hydrogen is mobile at modest temperatures within diamond. The H_2 molecule can be found in diamond, but the $\{\text{H}_2\}^*$ complex (Fig. 9.3) is more favourable by around 2.1 to 3.32 eV [208, 209, 210].

A single nitrogen substitutional, $\{\text{N}_s\}$, is able to capture a hydrogen atom but a deep level forms [208, 211] so it is not useful for *n*-type doping. A shallow donor has, however, been proposed by Miyazaki *et al.*[212], based on the nitrogen A-type $\{2\text{N}_s\}$ defect. This defect captures hydrogen with an ionisation energy of 0.6 eV. It has been experimentally verified that muons are also captured by the A-type defect [213], giving substance to the claim. There is some controversy over whether the 3107 cm^{-1} vibrational line is associated with H/N complexes [214, 208].

Hydrogen molecules are also usually present in large-scale processing of silicon wafers. These molecules readily enter the bulk, causing a change in the electrical properties, such as passivating electrically active defects and also forming new electrically active defects. Hydrogen bonds to the weak covalent bonds of self-interstitials and vacancies along with dopants and other impurities. An excellent review article by Estreicher [215] highlights the role of hydrogen in semiconductors.

Despite hydrogen and nitrogen both being common impurities in silicon, there has only been one *ab initio* theoretical study of their interaction [188]. It concluded that both $\{\text{N}_s\}$ and $\{\text{N}_i\}$ are able to trap hydrogen atoms, although with smaller binding energies than $\{\text{V}, \text{H}\}$. They assign the FTIR 2967 cm^{-1} line, discovered by Pajot *et al.*[216] in silicon prepared in a hydrogen atmosphere, to the N–H stretch mode of the $\{\text{N}_i, \text{H}\}$ defect. However this proved controversial, see the discussion at the end of this chapter.

First we present the results of our own investigations of nitrogen and hydrogen defects. We recover all previously known defects, but are unable to find any more stable ones. We then turn our attention to diamond due to its difference in lattice constant and hence potentially different defect characteristics. We search for new nitrogen defects and H/N complexes. Again we are able to reproduce previously

known defects, but are unable to find any new defects that may be useful as n -type dopants.

9.2 Computational Approach

We have already discussed the AIRSS method in Chapter 6 and how it is applied in practice in Chapter 8.

Our approach to understanding H/N complexes in silicon and diamond is to build up a picture of the lowest energy defects containing different sets of impurity atoms. We begin from a simulation cell that contains 32-atoms of bulk crystal as before (either silicon or carbon). Into this cell we place different numbers of defect atoms (N and H), vacancies and interstitials. One simulation cell might have a silicon vacancy and a nitrogen atom, or for example, two nitrogen atoms and one hydrogen atom. An AIRSS search is performed for each simulation cell. Again we use the PBE [170] generalised-gradient approximation exchange-correlation functional and ultrasoft pseudopotentials [36] with non-linear core corrections [171]. We sample the Brillouin zone of the reciprocal-space cell using a multi-B $2 \times 2 \times 2$ grid [1], as described in Section 2.7.5.

From the AIRSS searches, each initial simulation cell produces many different arrangements of the defect atoms. The lowest energy structure from each initial cell is then further relaxed, with a higher planewave cutoff and a tighter force tolerance of 0.001 eV/A. Sometimes higher energy metastable results are also further relaxed, for example if they have an energy very close to the ground state, or if they show some other interesting feature. A linear-program using the lowest-energy atomic arrangement of each defect type is then produced. This program minimises the total energy of the system with respect to different defect concentrations and allows us to see which defects are most likely to form.

With this understanding we then calculate the formation energies of the most probable defects. We define the formation energy, E_f as,

$$E_f = E_D - \sum_{i=1,t} n_i \mu_i, \quad (9.1)$$

where n_i , is the number of each atom of type i , in the defect cell of energy E_D . The chemical potentials, μ_i , for the H/N defects in silicon are,

$$\mu_{\text{Si}} = \frac{E(32\text{Si})}{32}, \quad (9.2)$$

$$\mu_{\text{H}} = \frac{E(32\text{Si}, 2\text{H}) - E(32\text{Si})}{2}, \quad (9.3)$$

$$\mu_{\text{N}} = \frac{E(32\text{Si}, 2\text{N}) - E(32\text{Si})}{2}, \quad (9.4)$$

where $E(32\text{Si})$ is the total energy of a 32-atom unit cell of perfect crystalline silicon and $E(32\text{Si}, 2\text{H})$ is the total energy of the same cell but containing 32-atoms of silicon and the lowest energy double-hydrogen-atom defect (which is known from previous studies of hydrogen in silicon to be an interstitial molecule, see Table 8.2). $E(32\text{Si}, 2\text{N})$ is the total energy of the same cell but also containing the lowest 2-nitrogen-atom defect.

We also use this method to evaluate the formation energies of carbon defects. We use the most stable nitrogen and hydrogen defects as the chemical potentials.

9.3 Results

9.3.1 Nitrogen in Silicon

We performed AIRSS searches for the following scenarios, a single nitrogen interstitial, $\{\text{N}_i\}$; two nitrogen interstitials, $\{2\text{N}_i\}$; a nitrogen interstitial with a silicon vacancy, $\{\text{N}_i, \text{V}\}$, *i.e.* a nitrogen substitutional, $\{\text{N}_s\}$ and two nitrogen interstitials with two vacancies, $\{2\text{N}_i, 2\text{V}\}$ ($=\{2\text{N}_s\}$).

Since the results only confirm what is already known, and since from previous experimentation we have seen absolute defect energies change by embedding into a 256-atom cell, yet relative energies remain reasonably stable, it was felt that the computational cost outweighed the merit of embedding the silicon results into larger cells.

The most stable nitrogen defect is the $\{2\text{N}_i\}$, see Fig. 9.1 (a), and this is used as the nitrogen chemical potential for all of the subsequent N and H/N defects.

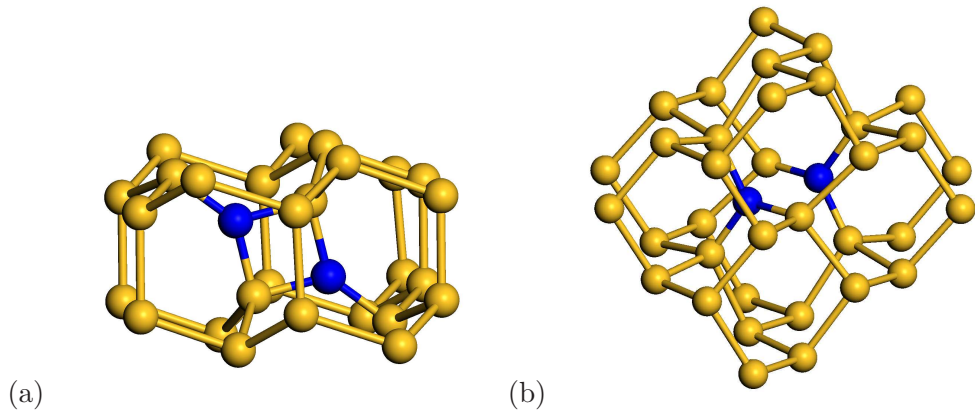


Figure 9.1: Double-nitrogen defects silicon — The silicon atoms are shown in yellow and the nitrogen atoms are shown in blue. (a) The ground-state $\{2N_i\}$ defect, which has C_{2h} symmetry. This defect has the lowest formation energy in silicon, and hence is used as the chemical potential for nitrogen in silicon in the subsequent calculations. (b) The ground-state $\{2N_s\}$ defect which has D_{3d} symmetry. Both defects are described fully in the text.

We found the $\{2N_i\}$ defect to have C_{2h} symmetry. It comprises a four-membered nearly-square ring of two nitrogen and two silicon atoms in a $\langle 110 \rangle$ plane with the nitrogen and carbon atoms three-fold and four-fold co-ordinated, respectively. The longer side is calculated to be 1.76 Å, the shorter side 1.73 Å, with a N–Si–N bond angle of 89.4° so that the nitrogen atoms are separated by 2.46 Å. This is in good agreement with Jones *et al.*[184] who calculated sides of 1.79 and 1.76 Å and a N–Si–N bond angle of 89°. These atomic positions are in close agreement with much of the literature [188, 191, 181, 186]. Karoui however *et al.*[189] presents a much more skewed structure with a nitrogen separation of 2.28 Å and a N–Si–N bond angle of 98°.

We also found the $\{2N_s\}$ defect which has D_{3d} symmetry, shown in Fig. 9.1 (b). This resembles two $\{N_s\}$ defects on nearest neighbour sites. This defect has also been widely reported in the literature. Each nitrogen atom is bonded to the three nearest neighbour silicon atoms with a bond length of around 1.85 Å. The three bond angles are 118.3°, and the nitrogen atoms are 3.45 Å apart. Its stability is due to it being completely saturated – all of the nitrogen atoms are three-fold co-ordinated whilst all of the carbon atoms are four-fold co-ordinated. Our results agree very well with previous reports of Si–N bond lengths of 1.77 [189], 1.83 [181], and 1.84 Å[188, 185]. Bond angles are reported in the range of 118 – 119° and the separation of nitrogen

Defect	E_f (eV)
$\{N_s\}$	1.80
$\{N_i\}$	1.79
$\{2N_s\}$	1.70
$\{2N_i\}$	0.00
$\{N_s, 2H_i\}$	1.50
$\{N_s, H_i\}$	0.80
$\{N_i, H_i\}$	0.44
$\{H_2\}$	0.00

Table 9.1: Formation energies of the defects we have found in silicon formed from the most stable N and H defects, as defined by Eq. 9.1.

atoms are between 3.51 and 3.68 Å[189, 181, 188, 185].

The formation of single nitrogen defects is much less likely, see Table 9.1. The lowest-energy $\{N_i\}$ defect is similar to those found previously [188, 189, 181] and has C_s symmetry. The nitrogen shares a lattice site with a silicon atom. The N–Si bond length is 1.73 Å. The nitrogen atom is 3-fold co-ordinated, its other two bonds being 1.76 and 1.77 Å long.

The most stable $\{N_s\}$ defect has a nitrogen atom on a lattice site, with T_d symmetry. The nitrogen attracts the 4 nearest neighbour silicon atoms towards it, forming bonds of length 2.03 Å, compared with 2.35 Å in the bulk. However, the widely accepted result, see for example McAfee *et al.*[188], shows this defect slightly away from the lattice site, with C_{3v} symmetry. This leaves the nitrogen with 3 bonds each of 1.85 Å. We do see this structure in the searches but it is 0.1 eV higher in energy than the ground state. We can only assume that this energy shift is caused by the limited size of the simulation cell.

Previous studies show that $\{N_i\}$ has a similar formation energy to $\{N_s\}$ [186], as we have also found, although in a crystal with no self-interstitials or vacancies the $\{N_i\}$ defect is much more likely to form. This model ignores the fact that silicon vacancies cost an extra 4 eV, as the chemical potential for silicon is set to that of a bulk atom. Therefore it is more favourable for single interstitial nitrogen to bind to another single interstitial and form a double-interstitial nitrogen than force a silicon vacancy to form and create a substitutional defect.

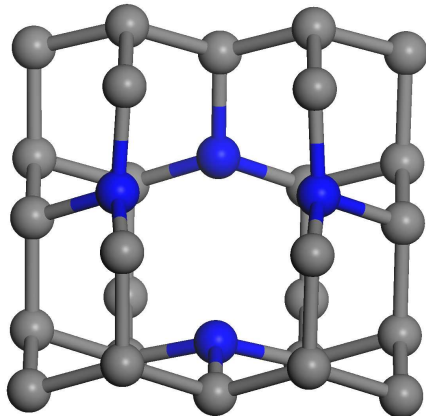


Figure 9.2: The $\{4N_s, V\}$ defect in diamond — It is based on the Loubser-Van Wyk model and is also known as the B-defect. The carbon atoms are shown in grey, the nitrogen atoms in blue. The defect belongs to the T_d symmetry group and is the most stable nitrogen defect in diamond that we find. We use this to define the chemical potential for nitrogen in diamond.

9.3.2 Nitrogen in Diamond

We performed AIRSS searches using the following 32-atom simulation cells, a single carbon vacancy, $\{V\}$; a single carbon interstitial, $\{I\}$; a nitrogen interstitial, $\{N_i\}$; a nitrogen substitutional $\{N_s\}$, a nitrogen substitutional and a vacancy, $\{N_s, V\}$; two nitrogen atoms and a vacancy, *i.e.* $\{N_i, N_s\}$; two nitrogen substitutionals $\{2N_s\}$ and four nitrogen atoms with five vacancies, $\{4N_s, V\}$.

Since the $\{4N_s, V\}$ defect is known to be the most stable of the above set of defects we use it as the chemical potential for nitrogen in diamond. The most stable hydrogen defect in diamond, $\{H_2\}^*$ is shown in Fig. 9.3 and is used to produce the chemical potential for hydrogen. $\{H_2\}^*$ is the first metastable hydrogen defect in silicon, hence the asterisk, whereas in diamond it is the most stable.

Table 9.2 shows that the three lowest energy nitrogen defects in diamond are $\{4N_s, V\}$, $\{2N_s\}$ and $\{N_s\}$. The most common defects in natural diamond are the type A $\{2N_s\}$ and the type B $\{4N_s, V\}$, with the latter having the lower formation energy.

The $\{4N_s, V\}$ B-defect shown in Fig. 9.2, has T_d symmetry and is based on the Loubser-Van Wyk model. The nitrogen atoms, which are all three-fold co-ordinated, form a tetrahedron around the carbon vacancy. The N–C bond lengths are 1.47 Å,

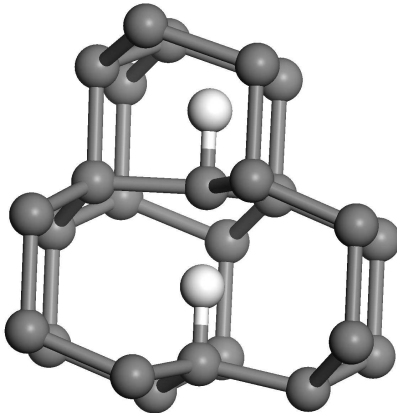


Figure 9.3: $\{\text{H}_2\}^*$ defect in diamond. The carbon atoms are shown in grey, the hydrogen atoms are shown in white. The defect has a C_{3v} symmetry. It comprises one hydrogen atom at a bonding site and one on an anti-bonding site. This defect is the ground-state configuration of hydrogen in diamond, although it has been identified as a metastable defect in bulk silicon, see Chapter 8. We use this to define the chemical potential of hydrogen in diamond.

Defect	E_f (eV)
$\{\text{I}\}$	11.70
$\{\text{V}\}$	6.71
$\{\text{N}_i\}$	9.29
$\{\text{N}_s, \text{N}_i\}$	7.10
$\{2\text{N}_s\}^*$	5.38
$\{\text{N}_s, \text{V}\}$	5.15
$\{\text{N}_s\}$	3.01
$\{2\text{N}_s\}$	2.20
$\{4\text{N}_s, \text{V}\}$	0.00
$\{\text{N}_i, \text{H}_i\}$	6.26
$\{\text{N}_i, 2\text{H}_i\}$	6.24
$\{2\text{N}_s, \text{H}_i\}$	1.72
$\{\text{N}_s, 2\text{H}_i\}$	1.24
$\{\text{N}_s, \text{H}_i\}$	0.53
$\{\text{H}_2\}^* {}^a$	0.00

Table 9.2: Formation Energies of the defects we have found in diamond derived from the most stable N and H defects as defined by Eq. 9.1.

[a] This defect is the first metastable hydrogen defect in silicon, hence the asterisk. It is the most stable hydrogen defect in diamond.

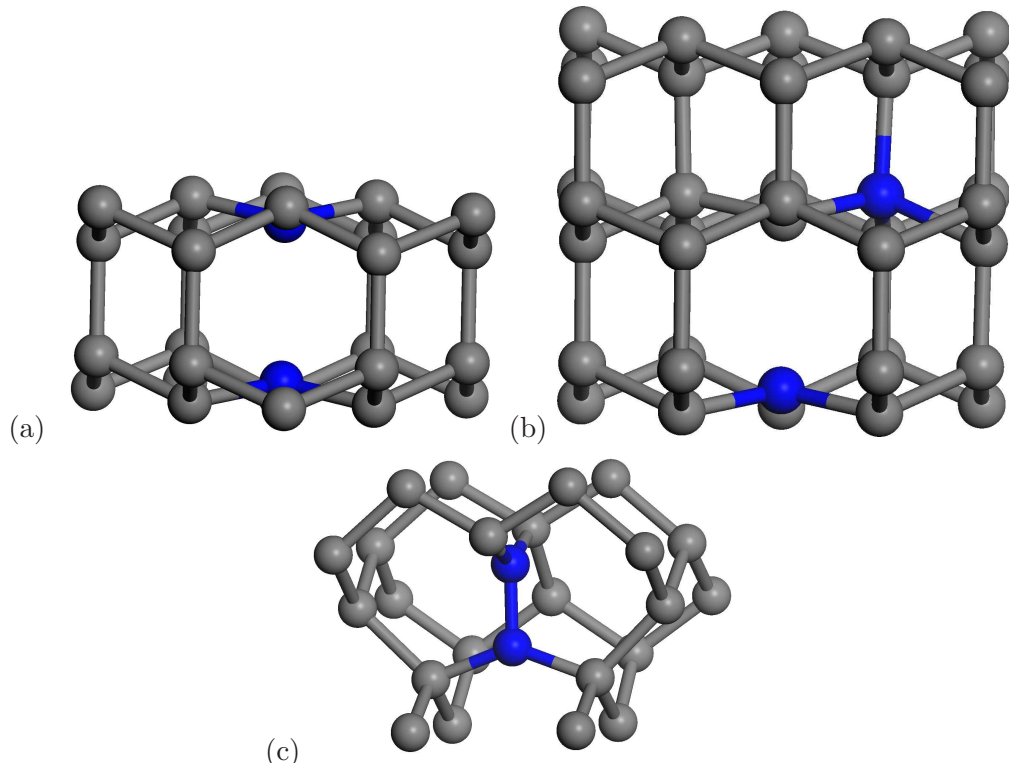


Figure 9.4: Double-nitrogen defects diamond — The carbon atoms are shown in grey, the nitrogen atoms are in blue. (a) The double-nitrogen substitutional $\{2N_s\}$ defect is known as the A-defect, it has D_{3d} symmetry, and is the second-most-stable nitrogen defect in diamond. (b) The third-most-stable nitrogen defect in diamond is the $\{2N_s\}^*$ which has C_s symmetry. (c) Two nitrogen atoms at one lattice vacancy gives rise to the $\{N_i, N_s\}$ defect which has a split- $\langle 001 \rangle$ configuration of D_{2d} symmetry. These defects are described fully in the text.

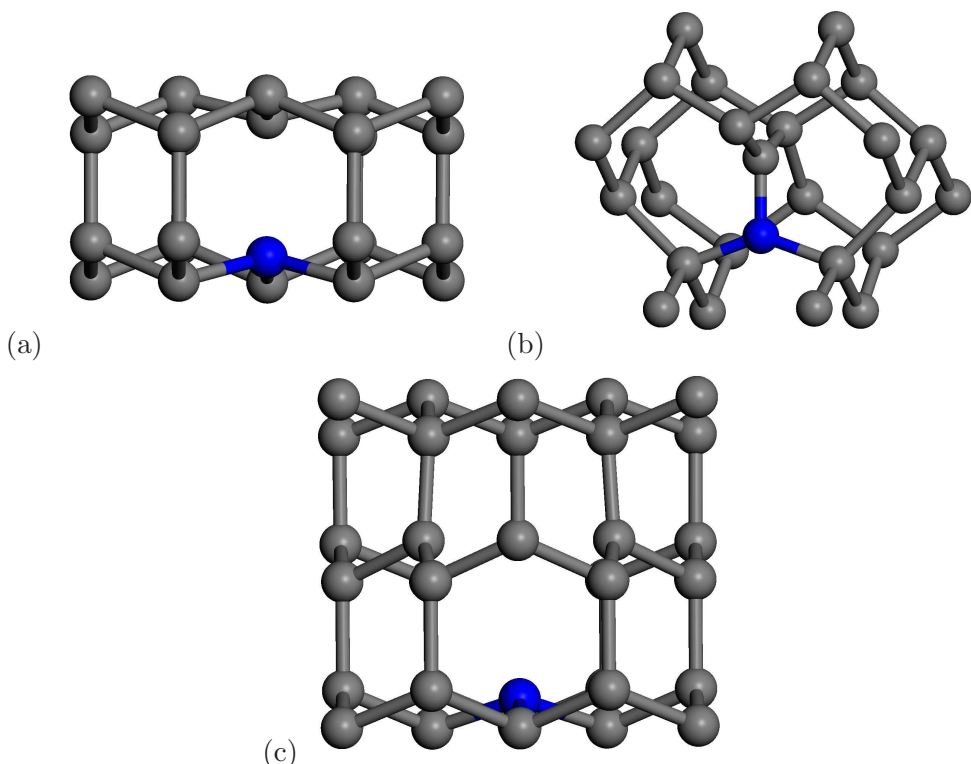


Figure 9.5: Single-nitrogen defects in diamond — The carbon atoms are shown in grey, the nitrogen atoms in blue. (a) The single-nitrogen substitutional defect, $\{N_s\}$, known as the C-centre has C_{3v} symmetry and is the major nitrogen defect found in synthetic diamond. (b) The nitrogen interstitial, $\{N_i\}$ has C_{2v} symmetry and a formation energy of 9.29 eV making it unlikely to form. (c) The nitrogen substitutional with a vacancy, $\{N_s, V\}$, has a C_{3v} symmetry. These defects are described fully in the text.

(94 % of the length of bulk C–C bonds) which is in good agreement with the value of 1.49 Å obtained by Briddon *et al.*[217, 218], and Mainwood [219] who quote a reduction to 96 % of the C–C bond length. Mainwood *et al.* also give the binding energy of the B-defect as 8.2 eV compared with a vacancy and a pair of A-defects. Our calculations give a slightly higher value of 8.91 eV.

The {2N_s} A-defect of D_{3d} symmetry was also found, with a formation energy 1.10 eV per nitrogen atom higher than the B-defect. The defect comprises of three-fold co-ordinated nitrogen substitutional atoms on adjacent lattice sites, as shown in Fig. 9.4 (a). The C–N bond lengths are all 1.46 Å (95 % of the bulk C–C bond length) and the N–N distance is 2.19 Å (a 30 % increase from the molecular N–N bond length). This is in good agreement with Mainwood [219] and Briddon *et al.*[217, 218]. The former finds the N–N bond increased by 38 % and N–C bond decreased to 95 % of the bulk C–C bond length, whereas the latter suggests 30 % and 96 %, respectively.

We also find the metastable {2N_s}* defect shown in Fig. 9.4 (b), which has C_s symmetry. It is higher in energy than {2N_s}, but 0.64 eV more energetically favourable than two isolated {N_s} defects. The nitrogen atoms are inequivalent and are on second nearest neighbour sites 2.80 Å apart. One nitrogen atom is bonded to its 3 nearest neighbour carbon atoms with bonds of length 1.45 Å, the other is bonded to its four nearest neighbours, with bond lengths of 1.59, 1.59, 1.51, 1.43 Å.

The {N_s} defect is rare in natural diamond but is the prevalent defect in synthetic diamond and is sometimes known as the C-centre. It is shown in Fig. 9.5 (a) and has C_{3v} symmetry. The nitrogen moves away from the lattice site and is bonded to three of its neighbouring carbon atoms, with N–C bonds of 1.48 Å. It increases the distance to the fourth carbon atom, which is only three-fold co-ordinated, by 1.98 Å an increase of 28 % over the C–C bulk bond length, which is consistent with the range of 25–33 % reported by Lombardi *et al.*[220].

The higher formation energy defects are mentioned below for completeness although they are less likely to form. The C_{2v} symmetry {N_i} defect forms a split defect pointing along the $\langle 0\ 0\ 1 \rangle$ direction at a lattice site, as shown in Fig. 9.5 (b). The N–C distance between the off-lattice site C and the N is 1.28 Å whereas the

other N–C bonds are 1.39 Å long. Both of the atoms on the lattice site are three-fold co-ordinated and planar. This is in good agreement with Goss *et al.*[221], who calculate the N–C bond lengths to be 1.26, 1.37 and 1.37 Å. They calculate the binding energy of the $\langle 001 \rangle$ -split compared to a self-interstitial and an $\{N_s\}$ to be 5.6 eV, which is in good agreement of our estimate of 5.42 eV.

$\{N_s, N_i\}$ shown in Fig. 9.4 (c) has a very similar structure to $\{N_i\}$. The nitrogen atoms are equivalent, they are three-fold co-ordinated, planar and centred on the carbon vacancy site. The defect is of D_{2d} symmetry. The N–N bond is 1.27 Å long and is directed along a $\langle 001 \rangle$ direction. The N–C bond lengths are all 1.39 Å. This defect has been studied by Goss *et al.*[221], who report 1.24 Å and 1.38 Å for the N–N and N–C bond lengths, respectively.

The $\{N_s, V\}$ defect has a nitrogen atom adjacent to a vacancy, as shown in Fig. 9.5 (c). It has a relatively high formation energy of 5.15 eV and belongs to the C_{3v} symmetry group. We find that the nitrogen has three bonds all 1.48 Å long, in excellent agreement with Gali *et al.*[203] who report 1.46 Å. Around the defect there are three carbon atoms, all three-fold co-ordinated.

9.3.3 Hydrogen and Nitrogen in Silicon

With an understanding of the most stable nitrogen defect we now progress to adding hydrogen into the simulation cells. We performed AIRSS searches with interstitial nitrogen and hydrogen atoms, $\{N_i, H_i\}$; substitutional nitrogen and interstitial hydrogen, $\{N_s, H_i\}$; and substitutional nitrogen and two hydrogen atoms, $\{N_s, 2H_i\}$. To our knowledge there has been only one study on hydrogen/nitrogen defects in silicon, by McAfee *et al.*[188].

The most stable of the hydrogen/nitrogen defects is $\{N_i, H_i\}$ with C_s symmetry, depicted in Fig. 9.6 (a). This takes the form of a buckled-bond-centred nitrogen atom, which is three-fold co-ordinated with bonds very close to planar. The hydrogen is bonded to the nitrogen. The N–Si bond lengths are both around 1.71 Å and the N–H bond-length is 1.03 Å. This is in good agreement with McAfee *et al.*[188], who found bond lengths of 1.73 Å and 1.05 Å, respectively.

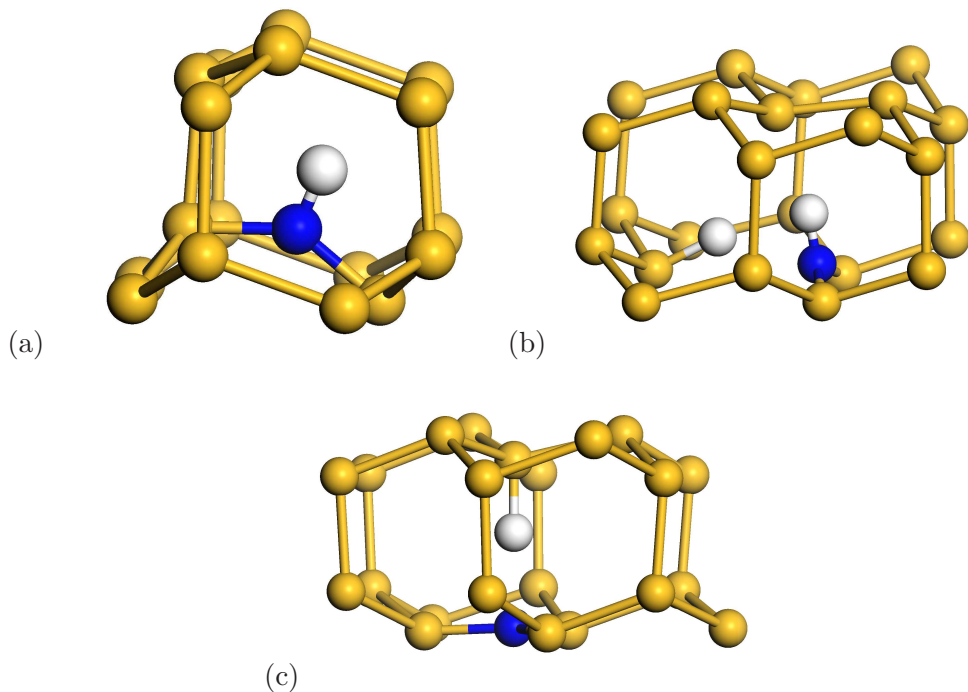


Figure 9.6: Hydrogen/nitrogen defects in silicon — The silicon atoms are shown in yellow, the nitrogen atoms in blue and the hydrogen atoms in white. (a) The C_s symmetry $\{N_i, H_i\}$ defect is the most stable hydrogen/nitrogen defect, with a formation energy of 0.44 eV. (b) The first metastable defect is the $\{N_i, 2H_i\}$ defect, which has a formation energy of 0.75 eV and also belongs to the C_s symmetry group. (c) The $\{N_s, H_i\}$ defect is also metastable with respect to separate nitrogen and hydrogen defects, although it is the most stable hydrogen/nitrogen defect in diamond. It has C_{3v} symmetry. The defects are discussed in more detail in the text.

The first metastable defect we find, $\{N_s, 2H_i\}$, has C_{3v} symmetry and is shown in Fig. 9.6 (b). To our knowledge this defect has not been described in the literature before. This is quite a complicated defect, and is slightly more energetically favourable than $\{N_s, H_i\}$ which is described below. $\{N_s, 2H_i\}$ looks similar to the $\{N_s, H_i\}$ defect but with the Si–N bond no longer pointing directly towards the nitrogen atom, and the bonds to the nitrogen atom are slightly less planar. The extra hydrogen is bonded to the three-fold co-ordinated nitrogen, placing the nitrogen in a similar configuration to the $\{N_i, H_i\}$ defect. The N–Si bonds are both 1.77 Å long, slightly longer (4 %) than in $\{N_i, H_i\}$ and the N–H bond length is 1.06 Å, 3 % longer than in $\{N_i, H_i\}$. The H–Si bond length is 1.49 Å, shorter than in the $\{N_s, H_i\}$ case.

Finally, we report the $\{N_s, H_i\}$ defect, shown in Fig. 9.6 (c). This is similar to the C_{3v} symmetry $\{N_s\}$ defect but with the hydrogen now bonded to the three-fold co-ordinated silicon atom, increasing its co-ordination number to four. The three N–Si bonds are all 1.85 Å, the same as in $\{N_s\}$. The N–H distance is 1.95 Å long and the H–Si bond is 1.80 Å long, in good agreement with McAfee *et al.*[188].

9.3.4 Hydrogen and Nitrogen in Diamond

We performed AIRSS searches on five scenarios, a nitrogen interstitial and a hydrogen interstitial, $\{N_i, H_i\}$; a nitrogen interstitial and two hydrogen interstitials, $\{N_i, 2H_i\}$; the same but with substitutional nitrogen, $\{N_s, H_i\}$, $\{N_s, 2H_i\}$; and two substitutional nitrogen atoms with a single hydrogen interstitial, $\{2N_s, H_i\}$.

The lowest energy $\{N_i, H_i\}$ defect found (shown in Fig. 9.7 (a)) is very similar to the $\{N_i\}$ defect, only with the hydrogen terminating the dangling carbon bond. The nitrogen forms a split- $\langle 001 \rangle$ configuration with a carbon atom displaced from its lattice site. It is of C_s symmetry with the nitrogen atom three-fold co-ordinated and the carbon atom four-fold co-ordinated (in contrast to the $\{N_i\}$ defect) since the dangling bond of the carbon atom is terminated by the hydrogen atom. The N–C bond length is 1.30 Å while the other two N–C bonds were longer at 1.38 and 1.40 Å, and the C–H bond was 1.03 Å long. This defect has a very high formation energy of 6.26 eV, hence it has not been mentioned in the diamond defect literature. It would require a nitrogen interstitial defect, already with a very large formation

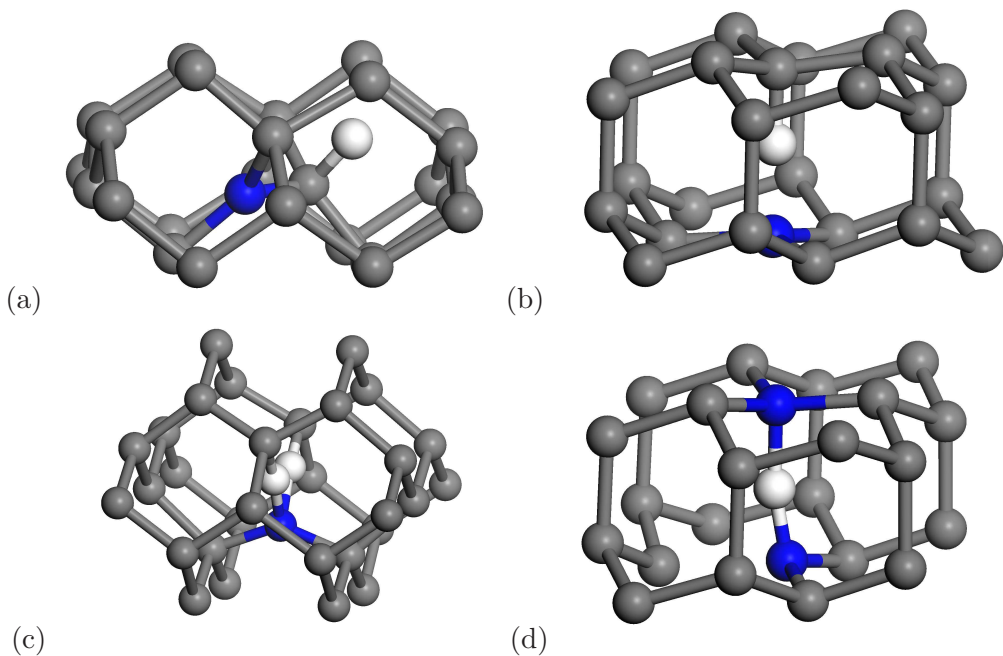


Figure 9.7: Hydrogen/nitrogen defects in diamond — The carbon atoms are shown in grey, the nitrogen atoms in blue and the hydrogen atoms in white. (a) The $\{N_i, H_i\}$ defect, which is metastable in silicon, is the ground-state structure (of its type) in diamond. It has C_{3v} symmetry. (b) The $\{N_s, H_i\}$ defect has C_s symmetry and is similar to the analogous defect in silicon, see Fig. 9.6(c). (c) The $\{N_s, 2H_i\}$ defect has near to C_{2v} symmetry. The two hydrogen atoms are not equivalent, but nearly so. See Table 9.3. (d) The $\{2N_s, H_i\}$ defect which also belongs to the C_s symmetry group. These defects are discussed in more detail in the text.

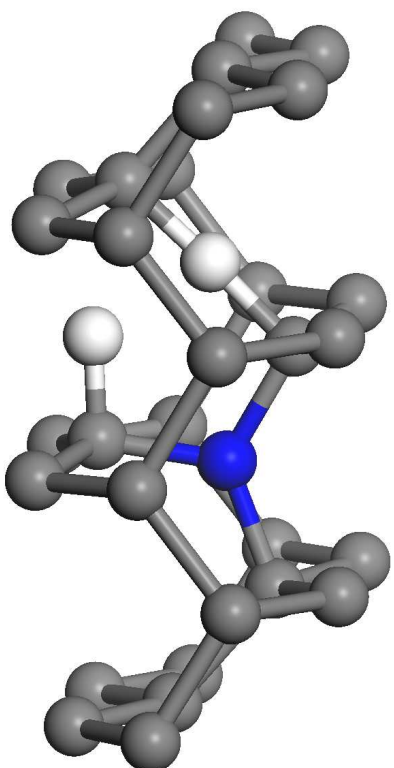


Figure 9.8: The $\{N_i, 2H_i\}$ defect is quite complicated. The carbon atoms are shown in grey, the nitrogen atoms in blue and the hydrogen atoms in white. It is similar to the $\{N_i, H_i\}$ defect but with a bond centred hydrogen bonded to a nearest-neighbour carbon atom. It has C_s symmetry and is discussed in more detail in the text.

Bond	Length (Å)
$\text{H}^{(1)}\text{--C}^{(1)}$	1.09
$\text{H}^{(1)}\text{--N}$	1.21
$\text{H}^{(2)}\text{--N}$	1.13
$\text{H}^{(2)}\text{--C}^{(2)}$	1.14
$\text{H}^{(1)}\text{--H}^{(2)}$	1.35

Table 9.3: Bond lengths of the $\{\text{N}_s, 2\text{H}_i\}$ defect.

energy of 9.29 eV to bind to a hydrogen atom.

The lowest-energy $\{\text{N}_i, 2\text{H}_i\}$ defect found is quite complicated as shown in Fig. 9.8. This defect also belongs to the C_s symmetry group and to the best of our knowledge, it has not been mentioned in the literature before. It is similar to the $\{\text{N}_i, \text{H}_i\}$ defect, but with the other hydrogen atom sitting in the bond-centred position next to one of the first-nearest-neighbour carbon atoms. The N–C bond lengths are 1.33, 1.35 and 1.30 Å. The nitrogen and all carbon atoms are three-fold and four-fold co-ordinated respectively.

The C_{3v} symmetry $\{\text{N}_s, \text{H}_i\}$ defect, shown in Fig. 9.7 (b), is similar to the analogous defect in silicon, see Fig. 9.6 (b). The nitrogen atom takes a similar position to that in the $\{\text{N}_s\}$ defect. The three N–C bonds are 1.46 Å long. The dangling carbon bond is terminated by a hydrogen atom which is 1.04 Å away from the carbon atom and 1.28 Å away from the nitrogen atom. This is in good agreement with Goss *et al.*[208] who calculate 1.06 and 1.26 Å, respectively.

Adding an extra hydrogen atom results in the $\{\text{N}_s, 2\text{H}_i\}$ defect shown in Fig. 9.7 (c). This defect, which has almost C_{2v} symmetry, is similar to the $\{\text{N}_s, \text{H}_i\}$ defect mentioned above, but with a hydrogen atom in the middle of one of the N–C bonds. To the best of our knowledge this defect is not mentioned in the literature. Both of the hydrogen atoms sit in buckled-bond-centred positions. Both hydrogen atoms are bonded to the nitrogen which is over-co-ordinated and has four bonds. From the bond lengths in Table 9.3, we can see that the hydrogen atoms are not equivalent.

The C_s symmetry defect $\{2\text{N}_s, \text{H}_i\}$, shown in Fig. 9.7 (d), is quite interesting. It is similar to the $\{2\text{N}_s\}$ defect with a hydrogen atom mid-way between the nitrogen atoms. One of the nitrogen atoms is bonded to three carbon atoms, with bond

lengths of 1.47, 1.47 and 1.49 Å. These are comparable to the {2N_s} defect where all the C–N bond lengths are 1.46 Å. The distance between this nitrogen atom and the hydrogen atom is 1.21 Å, whereas the second nitrogen atom is 1.05 Å away from the hydrogen atom. This second nitrogen atom has only two bonds to carbon atoms, both around 1.42 Å long. This type of defect was described by Miyazaki *et al.*[212]. However it was later proposed by Goss *et al.*⁴ that the defect reconstructs into the more stable atomic arrangement which we find above and is pictured in the review article [222].

9.4 Discussion

The large formation energies of hydrogen/nitrogen defects suggest that they are only present in bulk silicon in very small concentrations. The hydrogen/nitrogen defects studied have higher energies than the double-nitrogen interstitial defect and the hydrogen molecule at the tetrahedral site. Furthermore, since we have studied the least complex hydrogen/nitrogen defects, if we have overlooked a type of defect with a more favourable formation energy, it would be expected to contain more defect atoms and therefore might be unfavourable when entropy effects were included.

The H/N complex most likely to form in silicon is the {N_i, H_i} defect, which has a formation energy of 0.44 eV. This defect is assigned by McAfee *et al.*[188] to the FTIR 2967 cm⁻¹ vibrational line discovered by Pajot *et al.*[216] giving credibility to its existence, however a more recent paper by Lavrov *et al.*[223] assigns the vibrational line to a stretch mode of a dicarbon-dihydrogen complex⁵. This defect has also been found to be the lowest energy defect of its type in GaAs and Ge⁶. The defect is consistent with our saturated co-ordination-number theory that the most stable defects contain atoms that have all of their valence electrons in bonds and hence contain no dangling bonds. In this case, hydrogen has one bond, the nitrogen has three bonds and both silicon atoms involved in the defect contain four bonds.

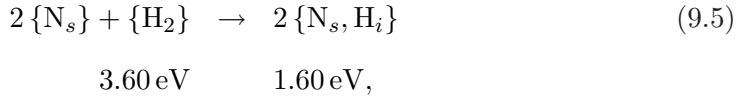
By considering the difference in the formation energies of isolated nitrogen and

⁴Unpublished.

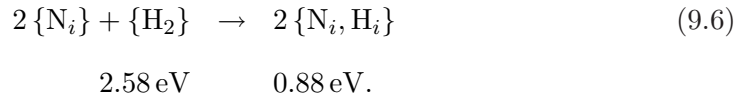
⁵I thank E. Lavrov for bringing this to my attention.

⁶A. J. Morris, C. J. Pickard and R. J. Needs, *unpublished* 2009.

hydrogen defects in bulk silicon we can see that any single-nitrogen defect should capture a hydrogen atom. When hydrogen molecules bond to $\{N_s\}$ it releases 1.0 eV per nitrogen atom,



and hydrogen also bonds to $\{N_i\}$, releasing 0.85 eV per nitrogen atom,



Since all H/N defect complexes have a positive formation relative to the hydrogen molecule and the $\{2N_i\}$ defect, we see that these two species cannot bind.

To the best of our knowledge this is the first time that all of the diamond defects presented have been studied at once in the same computational conditions and the results summarised in tabular form. We note from Tables 9.1 and 9.2 that interstitial defects in diamond have a much higher formation energy than in silicon. This is due to diamond having a smaller lattice constant than silicon, hence there is less space to accommodate interstitials.

It is important to analyse the diamond formation energies for each type of diamond separately. For example, for natural Ia A/B type diamond, all the defects in Table 9.2 may be considered. We see that the dominant defects are $\{4N_s, V\}$ and $\{H_2\}^*$, which means that hydrogen will not bond to any of the nitrogen defects we have studied.

When considering type Ia A diamond, we must exclude the $\{4N_s, V\}$ B-defect. This changes the prevalent defects quite substantially. Instead of forming $\{2N_s\} + \{H_2\}^*$ defects (each costing 2.20 eV) it is now much more favourable for hydrogen to bond to isolated $\{N_s\}$ and form $2\{N_s, H_i\}$ (costing a total of 1.06 eV) or perhaps for $\{2N_s\}$ to capture a hydrogen atom, resulting in $\{2N_s, H_i\} + \frac{1}{2}\{H_2\}^*$, with a formation energy of 1.72 eV. Since the dominant defect is the A centre, this inconsistency must be caused by either kinetic effects or perhaps there not being a

suitable reservoir of hydrogen in the bulk.

Finally if we take typical synthetic type Ib diamond, we must discount all double-nitrogen defects too. Sque *et al.*[211] comment that $\{2N_s, H_i\}$ is unlikely to form in synthetic diamond, and presumably they follow our reasoning that $\{2N_s\}$ defects are not present to capture the hydrogen atoms. Hence it is much more likely that $\{N_s, H_i\}$ and $\{N_s, 2H_i\}$ will form, (with formation energies of 0.53 and 1.24 eV respectively) than $\{N_s\} + \{H_2\}^*$, which has a higher formation energy of 3.01 eV. Chevallier *et al.*[214] also comment that it is entirely possible that we should see H/N defects in Ib diamond. However, many H defects are grown-in to synthetic diamond during manufacture, hence the defects present are process dependent and it is not always appropriate to use bulk energetics to draw conclusions.

In summary whether hydrogen atoms bond to nitrogen defects is entirely dependent on the type of nitrogen defects present in bulk diamond. Hence some types of diamond are expected to have hydrogen/nitrogen complexes and others will have separate nitrogen and hydrogen defects.

Whilst our searches did not find any new defect structures, out of the defect scenarios tried, they were able to reproduce easily all of the ground-state DFT structures of defects present in the literature compatible with the simulations cells chosen. Except the case of the $\{N_i\}_{Si}$ defect, where the ground-state defect was found to be metastable by 0.1 eV, all of the searches predicted the correct ground-state structure. This was especially successful for the $\{2N_s, H_i\}_C$ defect where the correct ground-state has only recently been found by Goss *et al.*[222] after further relaxing a more symmetric structure [224, 212].

It is disappointing that the method was not able to find any new structures. However, AIRSS does give the researcher more confidence in finding the DFT ground-state structure by searching over more of the potential energy landscape of atomic configurations than previously possible. We conclude that with a new system, that is less-well understood, AIRSS could shed light on defects much more rapidly than conventional methods. An example of such a problem is shown in the next chapter.

Chapter 10

Hydrogen / Nitrogen / Oxygen defects in Silicon

10.1 Introduction

FROM THE PREVIOUS two chapters we conclude that AIRSS is most useful when the number of impurity atoms is large enough to make it infeasible to use educated guesses and physical intuition for the structure of defects. In Chapter 8 we saw that previous intuition for the structure of the {I, H} defect was incorrect due to the reasonable, yet wrong, assumption that adding a hydrogen atom to the lowest-energy non-hydrogenated defect would lead to the lowest-energy hydrogenated defect. However, as we saw in Chapter 9 intuition has produced the lowest-energy nitrogen and nitrogen/hydrogen defects in both diamond and silicon. In this chapter we choose a complicated problem, containing hydrogen, nitrogen and oxygen defects in silicon and show that in this case AIRSS can find new and interesting defects. In Section 10.2.2 we justify our use of 32-atom cells in this and the previous chapter.

Hydrogen is a common impurity in silicon which is particularly important as a passivator of surfaces and bulk defects [156]. The role of hydrogen in semiconductors is highlighted in a review by Estreicher [215]. Adding nitrogen impurities to silicon affects the formation of voids and may increase the strength of the silicon crystal by immobilising dislocations, which reduces warping during wafer processing [178]. The

majority of silicon used in device technologies is manufactured in a quartz crucible by the Czochralski process, during which oxygen from the quartz readily enters the melt, see for example the review by Newman [225].

A wide variety of experimental probes are used to study defects in silicon, but it is often difficult to determine their detailed structures from measurements alone. Theoretical studies using *ab initio* techniques are helpful in this regard, as they are used to calculate both the defect formation energies and some of their experimental signatures. For example, local vibrational modes of defects are accessible to infra-red (IR) absorption experiments and may also be calculated within *ab initio* methods.

Throughout this chapter we denote a defect complex by listing its constituent atoms between braces, $\{A_i, B_s, \dots\}$, where a subscript denotes whether an atom is substitutional (s) or interstitial (i). For example, a defect containing two interstitial hydrogen atoms and a substitutional nitrogen atom is denoted by $\{2H_i, N_s\}$. Despite hydrogen and nitrogen being common impurities in silicon, we are aware of only one *ab initio* theoretical study of their interaction [188]. It was concluded that both $\{N_s\}$ and $\{N_i\}$ defects are able to trap hydrogen atoms, although with smaller binding energies than that of a hydrogen atom and a vacancy. The Fourier transform infra-red (FTIR) vibrational line at 2967 cm^{-1} found in silicon prepared in a hydrogen atmosphere is assigned to the N–H stretch mode of the $\{H_i, N_i\}$ defect [216]. Interstitial oxygen may be present in Cz-Si in concentrations as high as 10^{18} cm^{-3} . Oxygen impurity atoms may be used for gettering metallic impurities, which increases the overall crystal quality, but they also form electrically active thermal donors (TD) [226]. TDs can affect the local resistivity within the silicon wafer [227]. In addition, oxygen also interacts with nitrogen in bulk silicon to form TDs, and small concentrations of hydrogen can greatly enhance the formation of TDs [228, 229, 230]. It has been shown that the presence of hydrogen atoms in silicon crystals enhances the diffusion of oxygen. It has also been suggested that hydrogen passivates the electrical activity of N/O complexes in Cz-Si [231].

It is clear from these examples that the interactions between hydrogen, nitrogen, and oxygen impurities in silicon lead to important and complicated behaviour. Here we present the results of a computational search for low-energy defect complexes in

silicon containing hydrogen, nitrogen, and oxygen atoms. We confirm the stability of many of the previously-known defects and also report the structures and formation energies of some new low-energy defects.

The rest of this chapter is set out as follows, in Sec. 10.2 we discuss the computational methods used in the study. In Sec. 10.3 we describe the calculation of the defect formation energies and explain our choice of chemical potentials. A recap of H/N defects is presented in Sec. 10.4 and results for N/O defects are presented in Sec. 10.5, H/O defects in Sec. 10.6, and H/N/O defects in Sec. 10.7. The relative abundances of the defects are studied in Sec. 10.8 and a discussion of our results is presented in Sec. 10.9.

10.2 Computational Approach

10.2.1 Random Structure Searching

Creating the initial simulation cell is a three-stage process. First, we choose the size of the disruption to the perfect silicon lattice by defining the radius of a sphere in which the impurity atoms are to be placed randomly. We choose radii between 3 and 7 Å. Secondly, we chose the number of silicon atoms to have their positions randomised. In this study we randomise the position of 1 to 3 silicon atoms depending on the number of hydrogen, nitrogen and oxygen impurity atoms present. The randomisation sphere is centred on the centroid of the removed silicon atoms. Finally, the required number of hydrogen, nitrogen and oxygen impurity atoms and the chosen 1, 2 or 3 silicon atoms are placed at random positions within the sphere. The configurations are then relaxed using DFT forces calculated as in previous chapters,

10.2.2 Justification of the Use of 32-Atom Cells

The searches we report in this chapter are carried out in a body-centred-cubic simulation cell which would hold 32 atoms of crystalline silicon. Although this is a small cell, tests indicate that it is adequate for obtaining good structures for most of the defects studied and reasonably accurate formation energies, while keeping the com-

putational cost low enough to permit extensive searching. In Chapter 8 we reported results for hydrogen/silicon complexes in silicon. The searches were carried out in the same 32-atom cell used here, but each of the defect structures was re-relaxed in a 128-atom cell to obtain more accurate structures and energies. The defect formation energies for the 32-atom cells were not reported, but they are in fact in excellent agreement with the 128-atom values. Consider, for example, the calculations for an interstitial silicon atom (denoted by I) and hydrogen impurity atoms in crystalline silicon as reported in Chapter 8 and Ref. [1]. The changes in the formation energies on increasing the cell size from 32 to 128 atoms for the defects $\{I, H\}$, $\{I, H_2\}$, $\{I, H_3\}$ and $\{I, H_4\}$ are only 0.00, -0.07, -0.01 and -0.02 eV, respectively. Ref. [158] reports a study of self-interstitial defects in silicon, showing that the formation energies of the split-<110>, hexagonal and tetrahedral self-interstitials differed by less than 0.15 eV between cells with 16, 54, and 128 atoms.

We have also compared our results for N/O defects in silicon with data from the literature. Fujita *et al.*[232] used DFT and 216-atom cells to calculate the binding energies for the following defect reactions in silicon: $\{2N_i, O_i\} + \{O_i\} \rightarrow \{2N_i, 2O_i\}$, $\{2N_i\} + \{O_i\} \rightarrow \{2N_i, O_i\}$, and $\{N_i, O_i\} + \{O_i\} \rightarrow \{N_i, 2O_i\}$, obtaining 0.91, 0.98, and 1.12 eV, respectively, in good agreement with our 32-atom cell results of 0.80, 0.91 and 0.97 eV, respectively. Finally, Coutinho *et al.*[233] used DFT and 64-atom cells to calculate the formation energy of the $\{O_i\}$ defect, obtaining values between 1.989 and 1.820 eV, depending on the basis set used, which is in good agreement with our value of 1.90 eV. We should not, of course, expect a 32-atom cell to be sufficient for all point-defect calculations in silicon, and especially not for charged defect states, but there is a strong case for believing it to be adequate for the purposes of the current study.

10.3 Calculating the Formation Energies

In order to define defect formation energies it is necessary to specify the chemical potentials of the atomic species. The chemical potential for silicon is taken to be the bulk silicon value, so that the energy cost to add a silicon atom to a defect is the energy of a silicon atom in perfect crystalline silicon. The chemical potential for

hydrogen is derived from the lowest energy hydrogen defect in silicon, which is an interstitial molecule at the tetrahedral site, $\{H_2\}_i$, with the bond pointing along a $\langle 100 \rangle$ direction. This is the same chemical potential as used in our study of hydrogen impurities in silicon [1]. We use the most energetically favourable nitrogen defect, $\{2N_i\}$,[184, 188, 191, 181, 186] to set the chemical potential of nitrogen.

We perform around 130 AIRSS searches with one, two, three, or four interstitial oxygen atoms per cell. The lowest energy $\{O_i\}$ defect found is the buckled-bond-centred configuration which has been studied extensively [234, 235, 236, 233, 237, 238]. The $\{2O_i\}$ defect has two buckled-bond-centred oxygen atoms bonded to a silicon atom. This defect was first reported in Ref. [239] and is known as the staggered $\{2O_i\}$ defect.

Our searches also find the previously-reported staggered chain $\{3O_i\}$ defect [239, 240, 241, 242, 236, 243, 244]. We find a new structure, see Fig. 10.1, with a formation energy 0.15 eV lower than the staggered chain. To the best of our knowledge this defect has not been mentioned before. We also find the $\{4O_i\}$ defect which was previously reported as the $O_4(1,1)$ defect in Ref. [245].

Table 10.1 shows the formation energies per oxygen atom of the four oxygen defects and quartz, using the chemical potential of the $\{O_i\}$ defect as the reference for supplying oxygen atoms. We note that the formation energy decreases with each additional oxygen, showing that oxygen defects tend to aggregate, the lowest possible energy being achieved by forming crystalline SiO_2 (quartz). Needels *et al.* reported DFT calculations of the stability of O clusters in Si as a function of temperature [239].

We consider three different chemical potentials for oxygen. These correspond to choosing the source of oxygen atoms as $\mu_{\{O_i\}}$, $\mu_{\{4O_i\}}$, and μ_{quartz} . The chemical potential $\mu_{\{nO_i\}}$ for oxygen with the source of oxygen atoms being the $\{nO_i\}$ defect is calculated as the energy of the lowest-energy structure of the 32-atom silicon cell containing n oxygen atoms and the energy of the 32-atom bulk silicon cell, divided by n . The $\{O_i\}$ defect gives the highest oxygen chemical potential, while quartz gives the lowest chemical potential, μ_{quartz} . We include the chemical potential, μ_{quartz} , since it is the opposite extreme to $\mu_{\{O_i\}}$ in terms of oxygen saturation.

Defect	E_f per O (eV)
O	0.00
2O	-0.25
3O	-0.42
4O	-0.46
Quartz	-1.90

Table 10.1: Formation energies per oxygen atom for different oxygen complexes, relative to the oxygen bond-centred defect (O_{bc}). These values can also be thought of as the oxygen chemical potentials relative to a source of oxygen atoms consisting of single-oxygen defects.

Defect	O_i	$4O_i$	Quartz	Saturation
Bulk	0.00	0.00	0.00	✓
$\{2N_i\}$	0.00	0.00	0.00	✓
$\{O_i\}$	0.00	0.46	1.90	✓
$\{2O_i\}$	-0.50	0.42	3.29	✓
$\{3O_i\}$	-1.27	0.12	4.41	✓
$\{4O_i\}$	-1.85	0.00	5.73	✓
$\{H_2 i\}$	0.00	0.00	0.00	✓
$\{H_i, N_i\}$	0.45	0.45	0.45	✓
$\{H_i, N_s\}$	0.81	0.81	0.81	✓
$\{2H_i, N_s\}$	0.76	0.76	0.76	✗
$\{N_i, O_i\}$	0.43	0.89	2.32	✗
$\{N_i, 2O_i\}$	-0.54	0.39	3.25	✗
$\{N_i, 3O_i\}$	-0.92	0.49	4.76	✗
$\{2N_i, 2O_i\}$	-1.71	-0.78	2.09	✓
$\{2N_i, O_i\}$	-0.91	-0.44	0.99	✓
$\{3N_i, O_i\}$	0.15	0.61	2.05	✗
$\{H_i, O_i\}$	0.65	1.11	2.54	✗
$\{H_i, 2O_i\}$	-0.04	0.89	3.75	✗
$\{2H_i, O_i\}$	-0.23	0.23	1.67	✓
$\{2H_i, 2O_i\}$	-0.76	0.17	3.03	✓
$\{H_i, N_i, O_i\}$	-0.68	-0.22	1.21	✓
$\{2H_i, N_i, O_i\}$	-0.26	0.20	1.63	✗
$\{H_i, 2N_i, O_i\}$	-0.49	-0.03	1.40	✗
$\{H_i, N_i, 2O_i\}$	-0.85	0.08	2.94	✓

Table 10.2: Formation energies defined by Eq. (9.1) in eV for various H/N/O complexes with three different choices of the oxygen chemical potential. The final column indicates whether the system could form a structure with fully-saturated covalent bonding (✓), or whether it cannot (✗), see Sec. 10.9. The defect structures shown in bold have not, to the best of our knowledge, been reported in the literature before. The N/H defect energies have already been presented in Table 9.1, but are shown here for comparison with the new defects.

The formation energy of a defect, E_f , is defined as in Eqn. 9.1.

10.4 H/N Defects

We performed around 250 searches. These defects were discussed in Section 9.3.3. All of the H/N complexes we mention in this section have $E_f > 0$, and hence they are unlikely to form spontaneously.

10.5 N/O Defects

Our searches for the N/O complexes required around 1800 random starting structures. These searches found all the previously-known lowest-energy structures except the $\{2N_i, 2O_i\}$ defect. The $\{2N_i, 2O_i\}$ defect is quite large and it is probable that we have not relaxed a sufficiently large number of starting structures to find it.

For the $\{N_i, O_i\}$ defect we obtain the previously-known interstitial ring [246]. This defect has a positive $E_f(O_i)$ of 0.43 eV, and hence is unlikely to form. The structure of our $\{N_i, 2O_i\}$ defect is the same as found in previous studies [246, 232, 247]. This defect has a negative $E_f(O_i)$ of -0.54 eV, and therefore it could form in silicon.

We are not aware of any previous reports of the $\{N_i, 3O_i\}$ defect, which is shown in Fig. 10.2(a). The $\{N_i, 3O_i\}$ defect has a negative $E_f(O_i)$ of -0.92 eV, showing that a single bond-centred oxygen atom will bind to the $\{N_i, 2O_i\}$ defect.

Our searches for the $\{2N_i, 2O_i\}$ defect did not yield the structure reported previously,[248] which has different oxygen positions. We generated the structure reported by Fujita *et al.*[248] “by hand” and found it to be 0.19 eV lower in energy than our best structure. The defect of Fujita *et al.*[248] has a negative formation energy of $E_f(O_i) = -1.71$ eV, and the formation energy remains negative even when the reference structure for the oxygen chemical potential is taken to be that of the $\{4O_i\}$ defect in silicon. It is disappointing that our search has not given the previously-known lowest-energy $\{2N_i, 2O_i\}$ defect. However, we have included the lowest-energy known structure in our analysis of the relative populations of the

various defects presented in Sec. 10.8.

We find the previously-known lowest-energy $\{2N_i, O_i\}$ defect, [246, 248, 247, 249] which has a formation energy of $E_f(O_i) = -0.91$ eV. This defect binds oxygen very strongly and $E_f(O_i)$ remains negative even with the oxygen chemical potential from the $\{4O_i\}$ defect.

We are not aware of any previous reports of the $\{3N_i, O_i\}$ defect in the literature, which is shown in Fig. 10.2 (b). The $\{3N_i, O_i\}$ defect is quite large and it may not be well described within a 32-atom cell. The $\{N_i, 3O_i\}$ defect of Fig. 10.2 (a) and the $\{3N_i, O_i\}$ defects of Fig. 10.2 (b) both show a three-fold coordinated O atom. We have studied the difference between the self-consistent charge density of the defect system and that of overlapping atomic charge densities for $\{3N_i, O_i\}$ and $\{N_i, 3O_i\}$. The build-up of charge between the Si and three-fold-coordinated O atoms is of a similar nature for all three Si atoms we conclude that the it is best described as having three Si-O bonds. We also note that the bond lengths of the three-fold-coordinated O atom in $\{3N_i, O_i\}$ of 1.76, 1.79 and 1.89 Å, and those in $\{N_i, 3O_i\}$ of 1.73, 1.75 and 1.81 Å, are quite similar.

10.6 H/O Defects

We have relaxed around 350 starting structures for the H/O defects. The lowest energy $\{H_i, O_i\}$ defect that we find is composed of a buckled-bond-centred oxygen atom adjacent to a buckled-bond-centred hydrogen atom. This structure was also found by Estreicher [250, 251]. This defect has, however, been the subject of some controversy, as Jones *et al.*[252, 253] proposed that the hydrogen atom is attached to a silicon atom at an anti-bonding site. Our search also finds this defect configuration, but we calculate it to be 0.32 eV higher in energy than the ground state structure.

Our lowest-energy $\{H_i, O_i\}$ defect has a positive formation energy, and hence it is unlikely to form. The $\{2H_i, 2O_i\}$ defect is composed of two such defects in close proximity to one another, as shown in Fig. 10.3 (b). The defect has a negative formation energy and, to our knowledge, it has not been presented in the literature previously.

The lowest-energy $\{2H_i, O_i\}$ defect that we find (Fig. 10.3 (a)) adopts a $\{H_2\}^* + O_{bc}$ configuration. Measurements have shown an IR absorption line at 1075.1 cm^{-1} which has been assigned to a $O_i\text{-}H_2$ complex [254]. However, the $\{H_2\}^* + O_{bc}$ configuration of the $\{2H_i, O_i\}$ defect does not contain a hydrogen molecule. We also find a $\{2H_i, O_i\}$ defect structure containing a hydrogen molecule, but it is metastable with an energy 0.26 eV above our ground-state structure. To the best of our knowledge the $\{H_2\}^* + O_{bc}$ defect structure has not been reported previously.

Our most stable $\{H_i, 2O_i\}$ defect is a $O_{bc} + O_{bc} + H$ configuration. This defect has also been studied by Rashkeev *et al.* (see Fig. 3(a) of Ref. [243]), who report it to be a thermal double donor (TDD).

The $\{H_i, 2O_i\}$, $\{2H_i, O_i\}$ and $\{2H_i, 2O_i\}$ defects all have negative formation energies $E_f(O_i)$ and are therefore likely to form in bulk silicon.

10.7 H/N/O Defects

We have performed around 500 structural relaxations for the H/N/O defects. The four defects $\{H_i, N_i, O_i\}$ (Fig. 10.7 (a)), $\{2H_i, N_i, O_i\}$ (Fig. 10.7 (b)), $\{H_i, 2N_i, O_i\}$ (Fig. 10.7 (c)), and $\{H_i, N_i, 2O_i\}$ (Fig. 10.7 (d)), all have negative formation energies when using $E_f(O_i)$, and $\{H_i, N_i, O_i\}$ and $\{H_i, 2N_i, O_i\}$ also have negative formation energies when using $E_f(4O_i)$.

The $\{H_i, N_i, O_i\}$ defect has a formation energy of -0.68 eV compared with 0.43 eV for $\{N_i, O_i\}$. This implies that hydrogen readily binds to the $\{N_i, O_i\}$ defect. The hydrogen atom bonds to a silicon atom and breaks the third bond of the over-coordinated oxygen atom, giving the structure shown in Fig. 10.7 (a). This results in a defect with fully saturated bonds which is therefore quite low in energy.

The $\{2H_i, N_i, O_i\}$ defect is very similar to the $\{H_i, N_i, O_i\}$ defect mentioned above. The extra hydrogen atom bonds to the nitrogen atom which is then over-coordinated, having four bonds, see Fig. 10.7 (b). The over-coordinated nitrogen atom is energetically unfavourable and this defect would not readily form from $\{H_i, N_i, O_i\}$, however it could form from $\{N_i, O_i\}$ by capturing a hydrogen molecule.

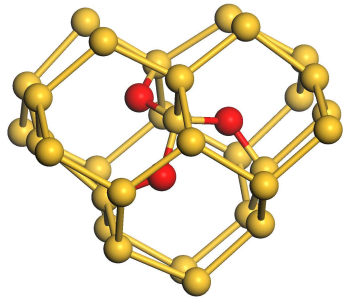


Figure 10.1: The $\{3O_i\}$ defect is composed of three buckled-bond-centred oxygen atoms, each bonded to a single, four-fold coordinated silicon atom. Silicon atoms are shown in yellow and oxygen atoms in red.

The $\{H_i, 2N_i, O_i\}$ defect is an interesting case. The nitrogen atom is over-coordinated because it binds to the hydrogen atom, see Fig. 10.7 (c). Since $\{2N_i, O_i\}$ has a formation energy of -0.91 eV and $\{H_i, 2N_i, O_i\}$ has a formation energy of -0.49 eV it is unlikely that a hydrogen atom will bind to $\{2N_i, O_i\}$.

The $\{H_i, N_i, 2O_i\}$ defect is very interesting. The fully-saturated bonding of this defect results in a low formation energy of -0.85 eV . This is lower than the formation energy of $\{N_i, 2O_i\}$, and hydrogen will therefore bind to this defect. The $\{H_i, N_i, 2O_i\}$ defect has a similar geometry to $\{3O_i\}$, but with one of the oxygen atoms replaced by a HN group. A HN group acting in a similar fashion to an oxygen atom was also observed in the $\{N_i, H_i\}$ defect of McAfee,[188] which looks similar to the bond-centred $\{O_i\}$ defect.

10.8 Relative Abundances

The formation energies of the various defects can be used to calculate the relative abundances of the defects at zero temperature as a function of the ratios of the H/N/O concentrations. The relative abundances for a chosen set of concentrations are those which minimise the total energy, and the chemical potentials do not enter the calculation. However, if we allow the oxygen atoms to combine with silicon to form quartz, it is straightforward to show that the minimum energy is always obtained by producing as much quartz as possible, so that no point defects containing oxygen atoms remain in the bulk, and the hydrogen and nitrogen atoms form $\{H_2 i\}$

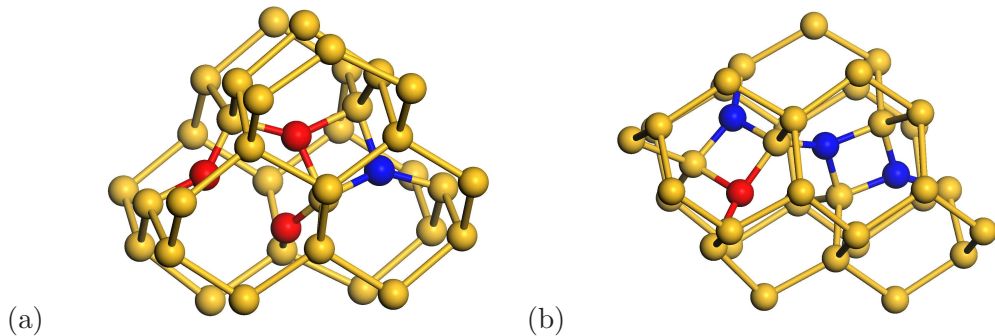


Figure 10.2: (a) The $\{N_i, 3O_i\}$ defect contains a four-atom ring consisting of a nitrogen atom, an oxygen atom and two silicon atoms. The two other oxygen atoms are in buckled-bond-centred positions. Note that the structure contains an over-coordinated oxygen atom with three bonds. (b) The lowest-energy $\{3N_i, O_i\}$ defect consists of a four-atom ring of two nitrogen atoms and two silicon atoms adjacent to another four-atom ring of an oxygen atom, a nitrogen atom and two silicon atoms. Note that the structure contains an over-coordinated oxygen atom with three bonds. The silicon atoms are in yellow, the nitrogen atoms in blue and the oxygen atom in red.

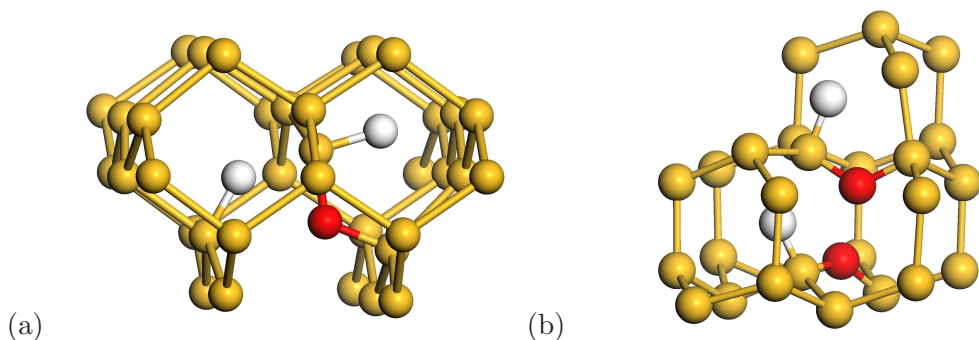


Figure 10.3: (a) The $\{2H_i, O_i\}$ defect is composed of a buckled-bond-centred oxygen atom adjacent to a distorted $\{H_2\}^*$ defect. This defect has a negative formation energy, showing that the $\{H_2\}^*$ defect[172] is stabilised by the presence of oxygen. (b) The $\{2H_i, 2O_i\}$ defect is composed of two adjacent $\{H_i, O_i\}$ defects. The silicon atoms are shown in yellow, the oxygen atom in red and the hydrogen atoms in white.

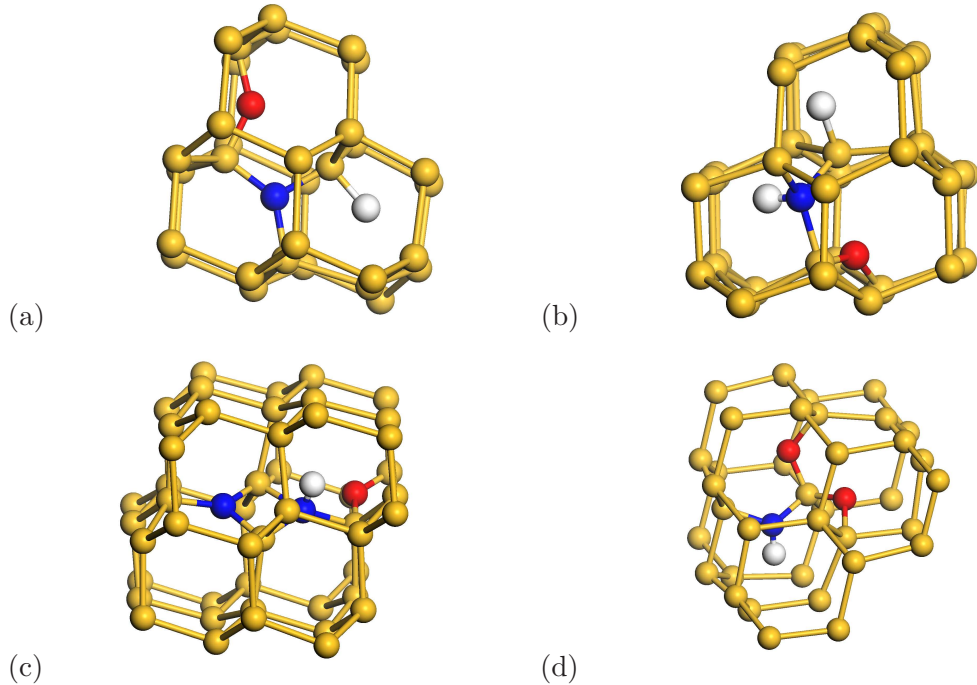


Figure 10.4: (a) The $\{H_i, N_i, O_i\}$ defect contains a nitrogen and silicon atom sharing a lattice site, with the dangling silicon bond terminated by the hydrogen atom. A nearest-neighbour silicon atom of the nitrogen atom is bonded to a buckled-bond-centred oxygen atom. (b) The $\{H_i, N_i, O_i\}$ defect contains a nitrogen and silicon atom sharing a lattice site, with the dangling silicon bond terminated by the hydrogen atom. A nearest-neighbour silicon atom of the nitrogen atom is bonded to a buckled-bond-centred oxygen atom. (c) The $\{2H_i, N_i, O_i\}$ defect is similar to the $\{H_i, N_i, O_i\}$ defect but with the nitrogen atom acquiring the extra hydrogen atom, making it over-coordinated with four bonds. This defect has the highest formation energy of all the H/N/O defects studied and is therefore unlikely to form. (d) The $\{H_i, N_i, 2O_i\}$ defect is very similar to the $\{3O_i\}$ defect, but with one of the oxygen atoms replaced by a NH group. The silicon atoms are shown in yellow, the oxygen in red, the nitrogen in blue and the hydrogen atoms in white.

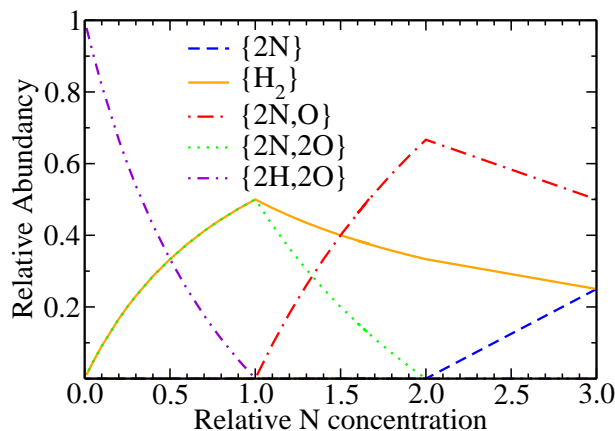


Figure 10.5: Relative concentrations of H/N/O defects in silicon as a function of the nitrogen concentration. At low nitrogen concentrations ($H:N:O = 1:<0.5:1$), the predominant defect is $\{2H_i, 2O_i\}$. As the nitrogen concentration increases the concentration of $\{2H_i, 2O_i\}$ decreases, with $\{2N_i, 2O_i\}$ and molecular hydrogen being formed. As the nitrogen concentration increases above unity, the concentration of $\{2N_i, 2O_i\}$ declines and $\{2N_i, O_i\}$ begins to form. At nitrogen concentrations larger than two, the additional nitrogen atoms form $\{2N_i\}$ defects.

and $\{2N_i\}$ defects. This is inconsistent with the extensive experimental evidence for other point defects in silicon involving hydrogen, nitrogen, and oxygen atoms. To gain some insight into the H/N/O defects which may be present we must therefore limit the propensity to form quartz and other low-energy oxygen defects in some way. We have chosen to present relative abundances in which the formation of $\{2O_i\}$, $\{3O_i\}$, $\{4O_i\}$, up to quartz are excluded, while allowing the formation of $\{O_i\}$. This is an arbitrary choice, but it serves to illustrate the type of behaviour which may arise. Figs. 10.5, 10.6, and 10.7 show relative abundances of the defects as a function of the H/N/O concentrations. In each figure we keep the concentrations of two of the species constant and equal to unity, while the concentration of the third impurity varies from zero to three. The main features of Figs. 10.5, 10.6, and 10.7 are that, for equal concentrations of hydrogen, nitrogen, and oxygen, the dominant defects are hydrogen molecules and the $\{2N_i, 2O_i\}$ defect. Varying the nitrogen or oxygen concentration leads to the formation of a wide variety of defects. Increasing the hydrogen concentration, however, only generates more hydrogen molecules. Other scenarios can be investigated using the data given in Table 10.2.

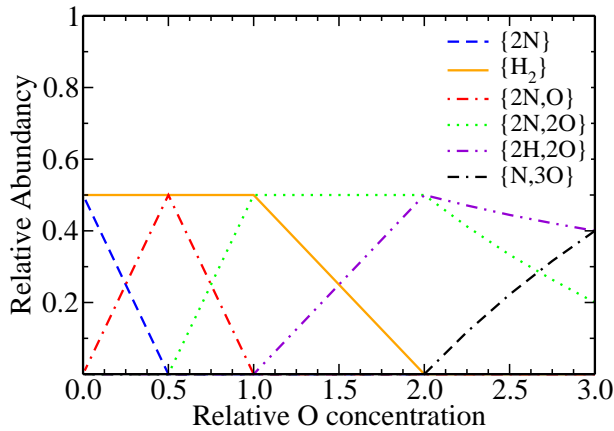


Figure 10.6: Relative concentrations of H/N/O defects in silicon as a function of the oxygen concentration. The behaviour is complex in this case, although the general trend is simply that the more stable defects containing larger numbers of oxygen atoms are favoured at higher oxygen concentrations.

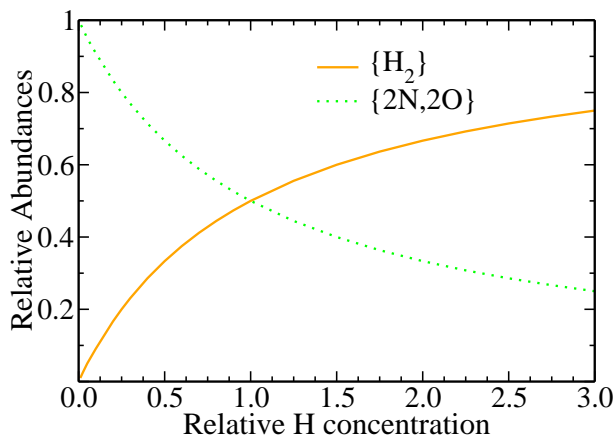


Figure 10.7: Relative concentrations of H/N/O defects in silicon as a function of the hydrogen concentration. Increasing the hydrogen concentration simply generates more interstitial hydrogen molecules.

10.9 Discussion

We have presented *ab initio* calculations of H/N/O complexes in bulk silicon within DFT. The defect complexes were generated in 32-atom supercells using the AIRSS method as outlined in Ref. [1]. The 32-atom cells are large enough to give a reasonable description of most of the defects, but small enough to allow extensive searching. To the best of our knowledge this is the first time that H/N/O complexes in silicon have been studied in detail. This work may be regarded as a “proof of concept” study in which we demonstrate that systematic searches for defect structures with several impurity species are possible.

AIRSS searches were performed on oxygen, hydrogen, and nitrogen defects to evaluate chemical potentials for the atoms. Whilst carrying out the searches on oxygen defects, we discovered a new $\{3O_i\}$ defect, shown in Fig. 10.1, which is more stable than the staggered defect which has been reported in the literature.

Our searches reproduced all of the previously-known lowest-energy H/N complexes. We have also described a new metastable $\{2H_i, N_s\}$ defect which is more favourable than some of the other H/N complexes presented in the literature.

The searches for N/O complexes were slightly less successful. We were unable to find the previously-known lowest-energy $\{2N_i, 2O_i\}$ defect. In this case, we performed DFT calculations on the previously-known structure for comparison. We discovered a new $\{3N_i, O_i\}$ defect (Fig. 10.2(a)) and a new $\{N_i, 3O_i\}$ defect (Fig. 10.2(b)) which is more stable than the $\{N_i, 2O_i\}$ defect, implying that an oxygen atom could bind to $\{N_i, 2O_i\}$.

Our searches reproduced all of the previously-known lowest-energy H/O complexes. We find the $\{H_i, O_i\}$ defect to have a positive formation energy, and therefore it is unlikely to form, but two adjacent $\{H_i, O_i\}$ defects can form a $\{2H_i, 2O_i\}$ defect (Fig. 10.3(b)) which has a formation energy of $E_f(O_i) = -0.76$ eV. We also find a new $\{2H_i, O_i\}$ defect which is based on the previously-reported H_2^* defect [172]. The $\{2H_i, O_i\}$ defect has $E_f(O_i) = -0.23$ eV, showing that the H_2^* defect can bind an oxygen atom.

To the best of our knowledge, no previous discussion of H/N/O complexes in

silicon has appeared in the literature. The $\{H_i, N_i, O_i\}$ and $\{H_i, N_i, 2O_i\}$ defects are more energetically favourable than their non-hydrogen-containing counterparts $\{N_i, O_i\}$, $\{N_i, 2O_i\}$, showing that many of these defects could exist in hydrogenated forms.

Another point of interest is that H/N complexes behave in an analogous fashion to oxygen defects. For example, the $\{H_i, N_i\}$ defect adopts a buckled-bond-centred arrangement with the hydrogen atom terminating the dangling bond on the nitrogen atom. The nitrogen atom takes a similar position to the oxygen atom in the O_{bc} defect, however without the hydrogen atom, since oxygen forms only two covalent bonds. The same relationship holds between the $\{3O_i\}$ and $\{H_i, N_i, 2O_i\}$ defects, where again the H/N group in the latter behaves like an O_{bc} defect in the former.

The right-hand column of Table 10.2 indicates whether or not it is possible for the indicated set of atoms to form a fully-saturated covalently-bonded structure. In such a structure each silicon atom is bonded to four other atoms, each nitrogen to three, each oxygen to two, and each hydrogen to one. As each bond is shared between two atoms, a fully-saturated covalently-bonded structure is impossible if the number of electrons is odd. We note from the data in Table 10.2 that the lowest energy defects are normally those having completely saturated bonds. A similar result for hydrogen defects in silicon was reported in [1]. This simple and rather obvious rule is useful for choosing combinations of impurity atoms which might form stable defects.

Consider a host crystal containing three types of impurity atom. (An example might be H/N/O impurities in silicon as studied here, but without the possibility of silicon vacancy formation which was allowed in our study of H/N defects.) Limiting the total number of impurity atoms to be ≤ 4 gives 34 possible cell contents for which searches must be performed. Increasing the number of possible impurities to five (while maintaining the maximum number of impurities in a cell to be ≤ 4) gives a total of 125 possible cell contents. The extra impurities could be other types of atoms, but they could also be host vacancies V and interstitials I , although this would reduce the number of possible cell contents to 112 because introducing a host vacancy and interstitial is the same as not introducing either. Searching over

the “impurities” H/N/O/I/V in silicon, with a maximum number of impurities of ≤ 4 and the same computational parameters as in the present study would cost about three times as much as the present study. For each set of cell contents we have in this work performed between about 20–900 structural relaxations, which appeared to be adequate in this case, although the required number is expected to increase rapidly with the size of the “hole” in the host crystal. In some cases it may be necessary to use larger “holes” to obtain all of the low-energy defects, and perhaps larger simulation cells as well. We have automated the search procedure and the calculations are performed in parallel. It appears to us that defect structure searches of the type described in this chapter with up to, say, five types of impurity are perfectly feasible with modern computing facilities.

Chapter 11

Discussion

IN THIS DISSERTATION two methods of computer simulation within condensed matter physics have been presented which both use random numbers. In Part II we studied point defects in crystals using the AIRSS technique. The atomic positions of point defects were chosen randomly, then relaxed to a local minimum using forces calculated within DFT.

11.1 AIRSS Defect Method

In Chapter 6 we discussed various global minimisation techniques based both on Simulated Annealing and Genetic Algorithms. Finally we presented a thorough description of the *ab initio* random structure searching (AIRSS) method, which was developed in the later chapters and applied to point defects in semiconductors.

Defects in semiconductors was the topic of Chapter 7, where we discussed the experimental methods used in point-defect investigations and how some of these quantities are also calculable using *ab initio* methods.

In Chapter 8 we presented the first results of the modified AIRSS algorithm to point-defect systems. We found three new hydrogen/silicon complexes: the $\{I, H\}$, $\{I, H_3\}$ and $\{I, H_4\}$ defects, demonstrating that AIRSS is a promising tool for point-defect structure determination. We presented the relative abundances of these different defects at zero temperature for different hydrogen and silicon concentrations.

By calculating the degeneracies of each defect, that is, the number of different ways the same defect could be formed per lattice site, we were able to calculate the configurational entropy of each defect. The vibrational free energy was not taken into account. This in turn allowed us to calculate the relative abundances of these defects at finite temperatures, such as at the temperatures of crystal-growth.

In Chapter 9 we demonstrated the capabilities of AIRSS with a more advanced problem. We studied nitrogen/hydrogen defects in both silicon and diamond, both well-studied fields; so it was not surprising that AIRSS was unable to find any lower-energy structures than those reported in the literature. However, AIRSS was 100 % successful at finding the DFT ground states of the structures attempted in three weeks, which had taken other *ab initio* techniques far longer to uncover.

With the exception of $\{N_i\}_{Si}$ which was found incorrectly to be metastable by 0.1 eV, all of the known ground-state defects were also correctly identified as the lowest-energy defects of their type with AIRSS. AIRSS was successful with the $\{2N_i, H_i\}_C$ defect which had only been uncovered the previous year.

This dissertation is the first time that all of N/H in C/Si defects had been presented together, so that the relative stabilities of the different type of defects could be compared on an even footing. We showed that in silicon, hydrogen does not bind to nitrogen defects since $\{2N_i\}$ and $\{H_2\}$ are more stable.

In diamond the story was a little different as interstitial defects are suppressed and have much higher formation energies since diamond has a much smaller lattice constant than silicon. It was important to specify which type of diamond is studied (1a A/B, 1a A or 1b) before we could decide the likelihood of N/H defects forming. We found that in 1a A/B-type diamond N/H binding was not possible but in 1a A and 1b types it is was much more likely. AIRSS was not able to find any new defects in these systems, it did however allow a range of defects to be found quickly.

Finally, in Chapter 10 we tested the AIRSS defect method for a problem which was much less-well studied. H/N/O defects in bulk silicon have quite a low symmetry due to their complexity, so the traditional approach of placing defect atoms at high symmetry points in the lattice had not been feasible. We already had an understanding of N and H defects separately in silicon from Chapter 8. We used

AIRSS to search for O defects and found, along with the well-known ground states, a new ground state for the $\{3O_i\}$ defect.

We turned our attention to considering N/O and H/O defect pairs, then to complexes containing all three different types of species. By considering the formation energies of the ground-state defect of each type, we were able to show that H binds to the $\{N_i, O_i\}$ and $\{2N_i, O_i\}$ defects forming $\{H_i, N_i, O_i\}$ and $\{H_i, 2N_i, O_i\}$ respectively. We also showed that when the H_2 molecule comes into contact with O_{bc} it forms the $\{O_i, 2H_i\}$ complex which looks similar to a lower symmetry version of the H_2^* defect (shown in diamond in Fig. 9.3). In other words, oxygen stabilises the H_2^* defect, essentially trapping the H_2 molecules in the bulk. AIRSS was also able to show an interesting effect where an N/H complex behaves in a similar chemical way to an O defect, hence O_{bc} and $\{3O_i\}$ have the same structure as $\{N_i, H_i\}$ and $\{H_i, N_i, 2O_i\}$ respectively.

We also found some weaknesses in AIRSS. Whilst it easily found the $\{2N_i\}$ defect, which is a ring structure of two silicon atoms and two nitrogen atoms, it was unable to reproduce the correct ground-state structure of $\{2N_i, 2O_i\}$ with the calculations performed. It was unclear why it could not find the correct minima, since when the correct ground-state structure was added “by hand” it was shown to be stable within the same DFT parameters as the unsuccessful search. We can only assume that many more searches than were computationally feasible were necessary to find the correct structure.

Finally we presented a quick way to estimate whether a defect type would be stable. We counted the number of unpaired electrons in the system by assigning H=1, O=2 and N=3. Whenever the total was even, the defect was very stable, whenever the number was odd, the defect was much less stable.

This was the first application of the AIRSS defect method to a completely unstudied problem, that of H binding to N/O complexes. Although AIRSS had problems with one of the N/O defects it solved the H/N/O binding problem and produced some other new interesting structures along the way.

11.2 Discussion

The AIRSS algorithm is perhaps the simplest conceivable for structure prediction. It is really amazing that it has only now begun to be used. One of the main strengths of AIRSS is its perfect parallelisability. Many thousands of small DFT calculations may be run on large computers. Since these calculations are usually small they benefit from fast communications within a node and are not affected by the slower communication between computational nodes.

The main constraint of the AIRSS algorithm is the *exponential wall*. The number of searches increases exponentially with the number of degrees of freedom. This may be eased with the use of constraints.

More recently we have begun to develop the AIRSS defect method further. The methodology to date has been to use relatively small simulation cells, with a fine k-point sampling the Brillouin zone. This keeps each individual DFT calculation reasonably cheap. However, from our studies on oxygen interstitial defects in alumina¹ we realise that large simulations cells containing ~ 120 atom calculations do not pose a problem. This is because,

- The *exponential wall* applies to the randomised atoms, not the total number of atoms. In this case the increase in computational cost scales as $\mathcal{O}(N^3)$ as usual in DFT, as long as the size of the randomised “hole” remains fixed.
- The larger cells need fewer k-points for Brillouin zone sampling. We can obtain converged results with a single k-point. If we place this k-point at the Γ -point then we benefit from at least a factor of two decrease in calculation time, since CASTEP needs only to perform real-number arithmetic.

In the long-run this new methodology should lead to a reduction in the number of erroneous minima found in our searches due to finite-simulation-cell size effects and should improve the accuracy of the total energy calculations when performing AIRSS searches involving charged states.

It is clear that the AIRSS defect methodology still has much to offer: calculations

¹In collaboration with Nick Hine, Imperial College, London and University of Cambridge.

of hydrogen in ZnO already show promising new structures². In this project we will begin to understand how AIRSS copes with charged defects.

11.3 AIRSS Outlook

So finally we move on to a discussion of the AIRSS method in general. The high pressure phases projects produce new knowledge all the time: there have been studies of TeO₂ [255], Lithium [256], Nitrogen [257] and Ammonia [148] all within the past two years.

I believe that most of the AIRSS development work will be focused on “constraints” so as to further limit the degrees of freedom of the randomisation leaving only those believed to be important to the problem.

For the future I can see AIRSS being applied to some very interesting and important problems, such as: surface reconstructions, and the behaviour of molecules on surfaces: or applied to interfaces, such as semiconductor / semiconductor oxide interfaces. In the longer term AIRSS could also be used to design new meta-materials with specific properties, such as direct band gaps, or specific dielectric properties for plasmonic applications. However care must be taken if this route is followed: even if a material can be designed, there is no guarantee that can be manufactured, especially if it is not the ground state of the material.

To conclude, this is the first PhD thesis that describes, develops and applies the AIRSS method. The method is so intuitive, has produced many excellent results and still has so much to offer that I am sure it will not be the last thesis on this topic.

²By the author, not included in this dissertation due to time constraints.

Appendices

Appendix A

Trial Wavefunctions as a Product of Two Slater Determinants

HERE I PRESENT A PROOF of the use of a product of two Slater determinants as a trial wave function. The proof can be found in several books such as, Foulkes *et al.*[53], however I found the following derivation easier to understand.

We can write the space and spin MB wavefunction in the following way:

$$\Psi = D_{\uparrow\downarrow} = \frac{1}{\sqrt{N!}} \sum_{\alpha} \widehat{P}_{\alpha} \phi_{\alpha_1} \dots \phi_{\alpha_N}, \quad (\text{A.1})$$

where N is the number of particles, ϕ are the one-particle orbitals, a product of a spatial, ψ and spin χ functions. We define \widehat{P}_{α} as a permutation operator that generates antisymmetric permutations of $\phi_{\alpha_1} \dots \phi_{\alpha_N}$.

For a spin independent operator, \hat{O} , its expectation value is,

$$\begin{aligned} \langle \hat{O} \rangle &= \langle D_{\uparrow\downarrow} | \hat{O} | D_{\uparrow\downarrow} \rangle \\ &= \frac{1}{N!} \left\langle \sum_{\alpha} \widehat{P}_{\alpha} \phi_{\alpha_1} \dots \phi_{\alpha_N} | \hat{O} | \sum_{\beta} \widehat{P}_{\beta} \phi_{\beta_1} \dots \phi_{\beta_N} \right\rangle. \end{aligned} \quad (\text{A.2})$$

We can always define a new permutation operator, \widehat{P}_{γ} , such that $\widehat{P}_{\beta} = \widehat{P}_{\alpha} \widehat{P}_{\gamma}$, and

$$\langle \hat{O} \rangle = \frac{1}{N!} \left\langle \sum_{\alpha} \widehat{P}_{\alpha} \phi_{\alpha_1} \dots \phi_{\alpha_N} \left| \hat{O} \right| \sum_{(\alpha\gamma)} \widehat{P}_{\alpha} \widehat{P}_{\gamma} \phi_{(\alpha\gamma)_1} \dots \phi_{(\alpha\gamma)_N} \right\rangle, \quad (\text{A.3})$$

Hence the operator, \widehat{P}_{α} just changes the dummy variable order and all the $N!$ permutations give the same energy, so we now have:

$$\langle \hat{O} \rangle = \left\langle \phi_{\alpha_1} \dots \phi_{\alpha_N} \left| \hat{O} \right| \sum_{\gamma} \widehat{P}_{\gamma} \phi_{(\alpha\gamma)_1} \dots \phi_{(\alpha\gamma)_N} \right\rangle. \quad (\text{A.4})$$

Suppose that our system of N particles has m up-spin particles and we choose the particular permutation of \widehat{P}_{α} , so that $\phi_{\alpha_1} \dots \phi_{\alpha_m}$ have all up-spin spin-components and $\phi_{\alpha_{m+1}} \dots \phi_{\alpha_N}$ have all down-spin spin-components. Since \hat{O} is independent of spin, the expectation value can only be non-zero if the first m orbitals of the \widehat{P}_{γ} permutation in the *ket* are also all up-spin (hence the last $N - m$ are all down spin). This reduces the number of permutations and we may now write:

$$\begin{aligned} \langle \hat{O} \rangle &= \left\langle \phi_{\alpha_1} \dots \phi_{\alpha_N} \left| \hat{O} \right| \sum_{\uparrow} \widehat{P}_{\uparrow} \phi_{(\alpha\uparrow)_1} \dots \phi_{(\alpha\uparrow)_m} \sum_{\downarrow} \widehat{P}_{\downarrow} \phi_{(\alpha\downarrow)_{m+1}} \dots \phi_{(\alpha\downarrow)_N} \right\rangle \\ \langle \hat{O} \rangle &= \left\langle \psi_{\alpha_1} \dots \psi_{\alpha_N} \left| \hat{O} \right| \sum_{\uparrow} \widehat{P}_{\uparrow} \psi_{(\alpha\uparrow)_1} \dots \psi_{(\alpha\uparrow)_m} \sum_{\downarrow} \widehat{P}_{\downarrow} \psi_{(\alpha\downarrow)_{m+1}} \dots \psi_{(\alpha\downarrow)_N} \right\rangle \\ &= \left\langle \psi_{\alpha_1} \dots \psi_{\alpha_N} \left| \hat{O} \right| D_{\uparrow} D_{\downarrow} \right\rangle. \end{aligned} \quad (\text{A.5})$$

It is convenient to have the *bra* also in the same form as the *ket*, so we may sum over all permutations of α as long as we divide by $N!$. We have already constructed $\phi_{\alpha_1} \dots \phi_{\alpha_N}$ to have the first m orbitals up-spin, hence the permutations we choose must also be of the same kind. We now have,

$$\langle \hat{O} \rangle = \frac{1}{N!} \left\langle D_{\uparrow} D_{\downarrow} \left| \hat{O} \right| D_{\uparrow} D_{\downarrow} \right\rangle, \quad (\text{A.6})$$

so we have shown that, for a spin-independent operator,

$$\langle \hat{O} \rangle = \frac{1}{N!} \left\langle D_{\uparrow\downarrow} \left| \hat{O} \right| D_{\uparrow\downarrow} \right\rangle = \frac{1}{N!} \left\langle D_{\uparrow} D_{\downarrow} \left| \hat{O} \right| D_{\uparrow} D_{\downarrow} \right\rangle. \quad (\text{A.7})$$

Appendix B

Pairing Wavefunctions

HERE I GIVE A JUSTIFICATION for the use of singlet-pairing wave functions that go beyond a Fermi fluid description. This was shown by Bouchard *et al.*[258]. However I think it is important enough to mention it again here.

In Appendix A it was shown that an expectation value of a non-spin dependent Hamiltonian acting on a Slater determinant can be written as a product of two Slater determinants — here I follow the derivation of López Ríos [55].

Consider $\Psi = D_\uparrow D_\downarrow$ where we define \mathbf{u}_j to be a spatial position of the j^{th} *up*-particle and \mathbf{d}_j to be a spatial position of the j^{th} *down*-particle. Each orbital is described as a planewave, as for a Fermi-fluid,

$$\Psi = \begin{vmatrix} e^{i\mathbf{k}_1 \cdot \mathbf{u}_1} & \dots & e^{i\mathbf{k}_1 \cdot \mathbf{u}_N} \\ \vdots & \ddots & \vdots \\ e^{i\mathbf{k}_N \cdot \mathbf{u}_1} & \dots & e^{i\mathbf{k}_N \cdot \mathbf{u}_N} \end{vmatrix} \times \begin{vmatrix} e^{i\mathbf{k}_1 \cdot \mathbf{d}_1} & \dots & e^{i\mathbf{k}_1 \cdot \mathbf{d}_N} \\ \vdots & \ddots & \vdots \\ e^{i\mathbf{k}_N \cdot \mathbf{d}_1} & \dots & e^{i\mathbf{k}_N \cdot \mathbf{d}_N} \end{vmatrix}. \quad (\text{B.1})$$

We take the transpose of D_\uparrow which will not change the value of the product and we take the complex conjugate of the elements of the D_\downarrow matrix, which will not change the value of the product as long as for each \mathbf{k} -vector in the wavefunction the $-\mathbf{k}$ -vector is also present. We know that multiplying an entire row or column in a determinant by a number, α_i , changes the value of the determinant also by α_i . So

we may write:

$$\begin{vmatrix} \alpha_1 e^{i\mathbf{k}_1 \cdot \mathbf{u}_1} & \dots & \alpha_1 e^{i\mathbf{k}_N \cdot \mathbf{u}_1} \\ \vdots & \ddots & \vdots \\ \alpha_N e^{i\mathbf{k}_1 \cdot \mathbf{u}_N} & \dots & \alpha_N e^{i\mathbf{k}_N \cdot \mathbf{u}_N} \end{vmatrix} \times \begin{vmatrix} \alpha_1 e^{-i\mathbf{k}_1 \cdot \mathbf{d}_1} & \dots & \alpha_1 e^{-i\mathbf{k}_1 \cdot \mathbf{d}_N} \\ \vdots & \ddots & \vdots \\ \alpha_N e^{-i\mathbf{k}_N \cdot \mathbf{d}_1} & \dots & \alpha_N e^{-i\mathbf{k}_N \cdot \mathbf{d}_N} \end{vmatrix}, \quad (\text{B.2})$$

and since the pre-factor that results is only a normalisation constant we can ignore it. We now use the fact that $\det(A) \det(B) = \det(AB)$, which implies that,

$$\begin{vmatrix} \sum_{j=1}^N \alpha_j e^{i\mathbf{k}_j \cdot (\mathbf{u}_1 - \mathbf{d}_1)} & \dots & \sum_{j=1}^N \alpha_j e^{i\mathbf{k}_j \cdot (\mathbf{u}_1 - \mathbf{d}_N)} \\ \vdots & \ddots & \vdots \\ \sum_{j=1}^N \alpha_j e^{i\mathbf{k}_j \cdot (\mathbf{u}_N - \mathbf{d}_1)} & \dots & \sum_{j=1}^N \alpha_j e^{i\mathbf{k}_j \cdot (\mathbf{u}_N - \mathbf{d}_N)} \end{vmatrix}. \quad (\text{B.3})$$

Hence we have developed a singlet pairing orbital of the form,

$$\varphi(\mathbf{r}_m) = \sum_{j=1}^N \alpha_j e^{i\mathbf{k}_j \cdot (\mathbf{u}_m - \mathbf{d}_m)}. \quad (\text{B.4})$$

For N planewaves the orbital describes a fluid but when more planewaves are added to the orbital, it allows Ψ to describe pairing not represented in the fluid wavefunction.

Glossary

Abbreviations

AIRSS	Ab initio random structure searching technique.
ARPES	Angle-resolved photoemission spectroscopy technique.
BCS	Bardeen-Cooper-Schrieffer theory of superconductivity.
BEC	Bose-Einstein condensate.
CASTEP	Cambridge Serial Total Energy Package, planewave DFT code.
CC	Coupled cluster method.
CI	Configuration interaction computational method.
CVD	Chemical vapour deposition, method of producing crystals.
Cz-Si	Silicon made by the Czochralski process.
DFPT	Density-functional perturbation theory.
DFT	Density-functional theory.
DMC	Diffusion quantum Monte Carlo.
EELS	Electron energy-loss spectroscopy technique.
EXX	Exact exchange, DFT method.
FTIR	Fourier-transform infra-red spectroscopy.
Fz-Si	Silicon made by the float-zone process.

GA	Genetic Algorithm global minimum optimisation technique.
GGA	Generalised gradient approximation; E_{xc} approximation.
GW	Hedin's GW approximation to MB perturbation theory.
HEG	Homogeneous electron gas, or Jellium.
HF	Hartree-Fock theory.
KLI	Krieger, Li and Iafrate; E_{xc} approximation.
LDA	Local density approximation; E_{xc} approximation.
LSDA	Local spin-density approximation; E_{xc} approximation.
LVM	Local-vibrational mode.
MB	Many-body.
MCSCF	Multi-configurational self-consistent field method.
MP	Monkhorst-Pack Brillouin zone sampling scheme.
Multi-Γ	Multi-k-point generalisation of Γ -point Brillouin zone sampling scheme.
Multi-B	Multi-k-point generalisation of the Baldereschi mean-value point Brillouin zone sampling scheme.
NMR	Nuclear magnetic resonance experimental technique.
OBDM	One-body density-matrix.
ODLRO	Off-diagonal long-range order.
OEP	Optimised effective potential, DFT method.
PCB	Population control bias.
PDF	Probability density function.
PEP	Pauli-exclusion principle.
QMC	Quantum Monte Carlo.

SA	Simulated Annealing global minimum optimisation technique.
TBDM	Two-body density-matrix.
TDDFT	Time-dependent density-functional theory.
USPP	Ultrasoft pseudopotential.
VMC	Variational quantum Monte Carlo.

Symbols

a	s -wave scattering length.
$E[n(\mathbf{r})]$	DFT total energy functional.
ϵ	One particle orbital energy.
E_f	Defect formation energy.
E_H	Hartree energy.
$E_L(\mathbf{R})$	Local energy of a configuration in space.
E_{PW}	Energy of highest Fourier component of planewave basis set; the cut-off energy.
E_T	Reference energy in DMC, used for population control.
$E_{xc}[n(\mathbf{r})]$	Exchange and correlation energy functional.
$f(\mathbf{R}, \tau)$	Importance-sampled function.
γ_{\max}	Highest Fourier component of reciprocal space Fourier transform grid.
G_B	Many-body branching Green's function.
G_D	Many-body drift and diffusion Green's function.
g_{\max}	Highest Fourier component of planewave basis set.
\hat{H}_H	Hartree Hamiltonian operator.
\hat{H}	Many-Body Hamiltonian operator.

\hat{h}	Single-body Hamiltonian operator.
Ha	Hartree, atomic unit of energy.
\mathbf{k}	Electron crystal momentum.
k_B	Boltzmann constant.
μ	Pöschl-Teller potential well-width parameter.
μ	Lagrange multiplier.
μ	Chemical potential.
$n(\mathbf{r})$	Electron density.
\mathbf{R}	Set of all particle positions and spins — a configuration of the system.
r_s	Wigner radius, electron density parameter.
σ	Standard deviation.
σ	Spin co-ordinate.
Σ_x^i	Non-local orbital-dependent exchange operator.
D_i	Slater determinant containing i^{th} order excitations.
T	Thermodynamic temperature.
$\mathcal{T}_s[n(\mathbf{r})]$	Kinetic energy functional of the non-interacting system.
$U(\mathbf{r})$	Particle potential energy.
$\mathbf{V}(\mathbf{R})$	Drift vector.
V_{ext}	External potential.
V_H	Hartree potential.
V_H^i	Orbital-dependent Hartree potential.
V_{KS}	Kohn-Sham potential.
V_S	Effective potential.

V_{xc}	DFT Exchange correlation potential.
ϕ	Eigenfunction of Hamiltonian, <i>or</i> one particle orbital.
Ψ	Many-body wavefunction.
Φ	Trial wavefunction.
φ	A two-particle pairing orbital.
ξ	Dimensionless energy parameter.
ζ	Backflow displacement function.

Bibliography

- [1] A. J. Morris, C. J. Pickard, and R. J. Needs, Phys. Rev. B **78**, 184102 (2008).
- [2] A. J. Morris, C. J. Pickard, and R. J. Needs, Phys. Rev. B **80**, 144112 (2009).
- [3] G. A. de Wijs *et al.*, Nature **392**, 805 (1998).
- [4] D. Alf  , G. D. Price, and M. J. Gillan, Nature **401**, 462 (1999).
- [5] D. Alf  , G. D. Price, and M. J. Gillan, Nature **405**, 172 (2000).
- [6] C.-K. Skylaris, P. D. Haynes, A. A. Mostofi, and M. C. Payne, J. Chem. Phys. **122**, 084119 (2005).
- [7] G. Cs  nyi, T. Albaret, M. C. Payne, and A. De Vita, Phys. Rev. Lett. **93**, 175503 (2004).
- [8] G. Cs  nyi, T. Albaret, G. Moras, M. C. Payne, and A. D. Vita, J. Phys: Condens. Matter **17**, R691 (2005).
- [9] G. Onida, L. Reining, and A. Rubio, Rev. Mod. Phys. **74**, 601 (2002).
- [10] M. A. L. Marques *et al.*, editors, *Time-dependent Density Functional Theory* (Springer Berlin Heidelberg New York, 2006), ISBN: 3-540-35422-0.
- [11] L. Hedin, Phys. Rev. **139**, A796 (1965).
- [12] L. Hedin and S. Lundqvist, Solid State Physics **23**, 1 (1969).
- [13] M. Born and R. Oppenheimer, Am. Phys. Leipzig **84**, 457 (1927).
- [14] D. R. Hartree, Cambridge Phil. Soc. **24**, 89 (1928).
- [15] J. C. Slater, Phys. Rev. **35**, 210 (1930).
- [16] V. Fock, Z. Physik **61**, 126 (1930).
- [17] L. H. Thomas, Proc. Cambridge Philos. Soc. **23**, 542 (1927).
- [18] E. Fermi, Z. Phys. **48**, 73 (1928).
- [19] R. O. Jones and O. Gunnarsson, Rev. Mod. Phys. **61**, 689 (1989).

- [20] R. M. Martin, *Electronic Structure : Basic Theory and Practical Methods* (Cambridge, 2004).
- [21] P. Hohenberg and W. Kohn, Phys. Rev. **136**, B864 (1964).
- [22] W. Kohn and L. J. Sham, Phys. Rev. **140**, A1133 (1965).
- [23] D. M. Ceperley and B. J. Alder, Phys. Rev. Lett. **45**, 566 (1980).
- [24] J. Perdew and A. Zunger, Phys. Rev. B **23**, 5048 (1981).
- [25] J. B. Krieger, Y. Li, and G. J. Iafrate, Phys. Rev. A **45**, 101 (1992).
- [26] F. Aryasetiawan and O. Gunnarsson, Rep. Prog. Phys. **61**, 237 (1998).
- [27] A. Ma, N. D. Drummond, M. Towler, and R. J. Needs, Phys. Rev. E **71**, 066704 (2005).
- [28] C. C. J. Roothaan, L. M. Sachs, and A. W. Weiss, Rev. Mod. Phys. **32**, 186 (1960).
- [29] R. J. Gdanitz, J. Chem. Phys. **109**, 9795 (1998).
- [30] J. P. Perdew and M. Levy, Phys. Rev. Lett. **51**, 1881 (1983).
- [31] L. J. Sham and M. Schlüter, Phys. Rev. Lett. **51**, 1888 (1983).
- [32] R. W. Godby, M. Schlüter, and L. J. Sham, Phys. Rev. Lett. **56**, 689 (1986).
- [33] R. W. Godby, M. Schlüter, and L. J. Sham, Phys. Rev. B **36**, 6497 (1987).
- [34] R. W. Godby, M. Schlüter, and L. J. Sham, Phys. Rev. B **37**, 10159 (1988).
- [35] S. J. Clark *et al.*, Z. Kristallogr **220**, 567 (2005).
- [36] D. Vanderbilt, Phys. Rev. B **41**, 7892 (1990).
- [37] J. Shim, E.-K. Lee, Y. J. Lee, and R. M. Nieminen, Phys. Rev. B **71**, 245204 (2005).
- [38] M. Gharaibeh, S. K. Estreicher, P. A. Fedders, and P. Ordejón, Phys. Rev. B **64**, 235211 (2001).
- [39] H. J. Monkhorst and J. D. Pack, Phys. Rev. B **13**, 5188 (1976).
- [40] A. Baldereschi, Phys. Rev. B **7**, 5212 (1973).
- [41] G. Rajagopal, R. J. Needs, S. Kenny, W. M. C. Foulkes, and A. James, Phys. Rev. Lett. **73**, 1959 (1994).
- [42] G. Rajagopal, R. J. Needs, A. James, S. D. Kenny, and W. M. C. Foulkes, Phys. Rev. B **51**, 10591 (1995).
- [43] J. M. Soler *et al.*, J. Phys.: Condens. Matter **14**, 2745 (2002).
- [44] X.-P. Li, R. J. Needs, R. M. Martin, and D. M. Ceperley, Phys. Rev. B **45**, 6124 (1992).

- [45] B. Wood, N. D. Hine, W. M. C. Foulkes, and P. García-González, Phys. Rev. B **76**, 035403 (2007).
- [46] P. Ballone, C. J. Umrigar, and P. Delaly, Phys. Rev. B **45**, 6293 (1992).
- [47] J. Casulleras and J. Boronat, Phys. Rev. Lett. **84**, 3121 (2000).
- [48] G. E. Astrakharchik, J. Boronat, J. Casulleras, I. L. Kurbakov and Yu. E. Lozovik, in *Recent Progress in Many-Body Theories: Proceedings of the 14th International Conference Barcelona, Spain 16 - 20 July 2007*, (World Scientific Pub. Co. Inc., 2008/06) edited by J. Boronat, G. E. Astrakharchik and F. Mazzanti, pages 245-251.
- [49] L. K. Wagner, J. Phys.: Condens. Matter **19**, 343201 (2007).
- [50] S. Datta, Int. J. Mod. Phys. B **22**, 4261 (2008).
- [51] B. B. D. Nissenbaum and A. Bansil, Phys. Rev. B **76**, 033412 (2007).
- [52] I. G. Gurtubay, N. D. Drummond, M. D. Towler, and R. J. Needs, J. Chem. Phys. **124**, 024318 (2006).
- [53] W. M. C. Foulkes, L. Mitas, R. J. Needs, and G. Rajagopal, Rev. Mod. Phys. **73**, 33 (2001).
- [54] N. Metropolis, A. W. Rosenbluth, M. N. Rosenbluth, A. M. Teller, and E. Teller, J. Chem. Phys. **21**, 1087 (1953).
- [55] P. López Riós, *Backflow and Pairing wavefunction for Quantum Monte Carlo Methods.*, PhD thesis, University of Cambridge, 2006.
- [56] T. Kato, Commun. Pure Appl. Math. **10**, 151 (1957).
- [57] R. T. Pack and W. B. Brown, J. Chem. Phys. **45**, 556 (1966).
- [58] P. López Ríos, A. Ma, N. D. Drummond, M. D. Towler, and R. J. Needs, Phys. Rev. E **74**, 066701 (2006).
- [59] R. P. Feynman and M. Cohen, Phys. Rev. **102**, 1189 (1956).
- [60] M. A. Lee, K. E. Schmidt, M. H. Kalos, and G. V. Chester, Phys. Rev. Lett. **46**, 728 (1981).
- [61] K. E. Schmidt, M. A. Lee, M. H. Kalos, and G. V. Chester, Phys. Rev. Lett. **47**, 807 (1981).
- [62] Y. Kwon, D. M. Ceperley, and R. M. Martin, Phys. Rev. B **48**, 12037 (1993).
- [63] Y. Kwon, D. M. Ceperley, and R. M. Martin, Phys. Rev. B **58**, 6800 (1998).
- [64] M. Holzmann, D. M. Ceperley, C. Pierleoni, and K. Esler, Phys. Rev. E **68**, 046707 (2003).
- [65] C. Pierleoni, D. M. Ceperley, and M. Holzmann, Phys. Rev. Lett. **93**, 146402 (2004).

- [66] R. M. Panoff and J. Carlson, Phys. Rev. Lett. **62**, 1130 (1989).
- [67] M. Holzmann, B. Bernu, and D. M. Ceperley, Phys. Rev. B **74**, 104510 (2006).
- [68] J. Toulouse and C. J. Umrigar, J. Chem. Phys. **126**, 084102 (2007).
- [69] C. J. Umrigar, J. Toulouse, C. Filippi, S. Sorella, and R. G. Hennig, Phys. Rev. Lett. **98**, 110201 (2007).
- [70] N. D. Drummond and R. J. Needs, Phys. Rev. B **72**, 085124 (2005).
- [71] N. D. Drummond, Z. Radnai, J. R. Trail, M. D. Towler, and R. J. Needs, Phys. Rev. B **69**, 085116 (2004).
- [72] D. M. Ceperley and M. H. Kalos, *Monte Carlo Methods in Statistical Physics*, 2nd ed. (Springer, Berlin, Germany, 1986).
- [73] D. M. Ceperley, J. Stat. Phys. **63**, 1237 (1991).
- [74] W. Ketterle, Rev. Mod. Phys. **74**, 1131 (2002).
- [75] E. A. Cornell and C. E. Wieman, Rev. Mod. Phys. **74**, 875 (2002).
- [76] T. Köhler, K. Góral, and P. S. Julienne, Rev. Mod. Phys. **78**, 1311 (2006).
- [77] S. Giorgini, L. P. Pitaevskii, and S. Stringari, Rev. Mod. Phys. **80**, 1215 (2008).
- [78] I. Bloch, J. Dalibard, and W. Zwerger, Rev. Mod. Phys. **80**, 885 (2008).
- [79] U. Fano, Phys. Rev. **124**, 1866 (1961).
- [80] H. Feshbach, Ann. Phys. (N.Y.) **19**, 287 (1962).
- [81] S. Inouye *et al.*, Nature **392**, 151 (1998).
- [82] P. Courteille, R. S. Freeland, D. J. Heinzen, F. A. van Abeelen, and B. J. Verhaar, Phys. Rev. Lett. **81**, 69 (1998).
- [83] J. Carlson, S.-Y. Chang, V. R. Pandharipande, and K. E. Schmidt, Phys. Rev. Lett. **91**, 050401 (2003).
- [84] G. E. Astrakharchik, J. Boronat, J. Casulleras, and S. Giorgini, Phys. Rev. Lett. **93**, 200404 (2004).
- [85] S. Y. Chang, V. R. Pandharipande, J. Carlson, and K. E. Schmidt, Phys. Rev. A **70**, 043602 (2004).
- [86] G. E. Astrakharchik, J. Boronat, J. Casulleras, and S. Giorgini, Phys. Rev. Lett. **95**, 230405 (2005).
- [87] S. Y. Chang and V. R. Pandharipande, Phys. Rev. Lett. **95**, 080402 (2005).
- [88] J. Carlson and S. Reddy, Phys. Rev. Lett. **95**, 060401 (2005).
- [89] A. Gezerlis, S. Gandolfi, K. E. Schmidt, and J. Carlson, Phys. Rev. Lett. **103**, 060403 (2009).

- [90] V. K. Akkineni, D. M. Ceperley, and N. Trivedi, Phys. Rev. B **76**, 165116 (2007).
- [91] E. Burovski, E. Kozik, N. Prokof'ev, B. Svistunov, and M. Troyer, Phys. Rev. Lett. **101**, 090402 (2008).
- [92] S. Giorgini, L. P. Pitaevskii, and S. Stringari, Rev. Mod. Phys. **80**, 1215 (2008).
- [93] C. Lin, F. H. Zong, and D. M. Ceperley, Phys. Rev. E **64**, 016702 (2001).
- [94] N. D. Drummond, M. D. Towler, and R. J. Needs, Phys. Rev. B **70**, 235119 (2006).
- [95] R. P. Feynman, Phys. Rev. **94**, 262 (1954).
- [96] R. P. Feynman and M. Cohen, Phys. Rev. **102**, 1189 (1956).
- [97] A. J. Morris, C. J. Pickard, and R. J. Needs, unpublished .
- [98] P. R. C. Kent, R. J. Needs, and G. Rajagopal, Phys. Rev. B **59**, 12344 (1999).
- [99] R. J. Needs, M. Towler, N. D. Drummond, and P. López- Riós, *CASINO User's Guide Version 2.4.0*, 2009, University of Cambridge, Cambridge.
- [100] M. Bartenstein *et al.*, Phys. Rev. Lett. **92**, 120401 (2004).
- [101] J. Kinast *et al.*, Science **307**, 1296 (2005).
- [102] G. B. Partridge, W. Li, R. I. Kamar, Y. Liao, and R. G. Hulet, Science **311**, 503 (2006).
- [103] A. Perali, P. Pieri, and G. C. Strinati, Phys. Rev. Lett. **93**, 100404 (2004).
- [104] Y. Nishida, Phys. Rev. A **79**, 013627 (2009).
- [105] A. Badinski, J. R. Trail, and R. J. Needs, J. Chem. Phys. **129**, 224101 (2008).
- [106] A. Badinski and R. J. Needs, Phys. Rev. B **78**, 035134 (2008).
- [107] A. Badinski, P. D. Haynes, and R. J. Needs, Phys. Rev. B **77**, 085111 (2008).
- [108] A. Badinski and R. J. Needs, Phys. Rev. E **76**, 036707 (2007).
- [109] N. Nemec, arXiv:0906.0501 (2009).
- [110] A. Lüchow, R. Petz, and T. C. Scott, J. Chem. Phys. **126**, 144110 (2007).
- [111] F. A. Reboreda, R. Q. Hood, and P. R. C. Kent, Phys. Rev. B **79**, 195117 (2009).
- [112] F. Miescher, Med.-Chem. Unters **4**, 441 (1871).
- [113] R. Franklin and R. G. Gosling, Nature **171**, 740 (1952).
- [114] J. D. Watson and F. H. C. Crick, Nature **171**, 737 (1953).

- [115] I. A. Buyanova, W. M. Chen, and B. Monemar, MRS Internat. J. Nitride Semicond. Res. **6**, 2 (2001).
- [116] M. Garey and D. S. Johnson, *Computers and Intractability: A Guide to the theory of NP-completeness*, (W. H. Freeman and Co., 1979).
- [117] J. P. K. Doye, D. J. Wales, W. Branz, and F. Calvo, Phys. Rev. B **64**, 235409 (2001).
- [118] S. Kirkpatrick, C. D. Gelatt Jr., and M. P. Vecchi, Science **220**, 671 (1983).
- [119] L. T. Wille, Chem. Phys. Lett. **133**, 405 (1987).
- [120] J. Ma and J. E. Straub, J. Chem. Phys. **101**, 533 (1994).
- [121] C. Tsos and C. L. Brooks III, J. Chem. Phys. **101**, 6405 (1994).
- [122] M. Prentiss, D. Wales, and P. Wolynes, J. Chem. Phys. **128**, 225106 (2008).
- [123] J. Schneider, I. Morgenstern, and J. M. Singer, Phys. Rev. B **54**, 5085 (1998).
- [124] D. J. Wales, J. Phys. Chem. A **101**, 5111 (1997).
- [125] D. J. Earl and M. W. Deem, Phys. Chem. Chem. Phys. **7**, 39010 (2005).
- [126] M. A. Neumann, F. J. J. Leusen, and J. Kendrick, Angew. Chem. Int. Ed. **47**, 2427 (2008).
- [127] J. Holland, *Adaptation in Natural and Artificial Systems* (University of Michigan Press, Ann Arbor, MI, 1975).
- [128] R. L. Johnston, Dalton Trans. **22**, 4193 (2003).
- [129] C. Darwin, *On the Origin of Species* (John Murray, Albemarle Street, 1859).
- [130] M. d'Aveza and A. Zunger, Phys. Rev. B **78**, 064102 (2008).
- [131] D. M. Deaven and K. M. Ho, Phys. Rev. Lett. **75**, 288 (1995).
- [132] A. R. Oganov and C. W. Glass, J. Chem. Phys. **124**, 244704 (2006).
- [133] C. W. Glass, A. R. Oganov, and N. Hansen, Comp. Phys. Comm. **175**, 713 (2006).
- [134] A. R. Oganov and C. W. Glass, J. Phys. Cond. Mat. **20**, 064210 (2008).
- [135] R. W. Smith, Comp. Phys. Comm **71**, 134 (1992).
- [136] C. E. Mohn and W. Kob, E-MRS Fall Meeting 2007 (2008), cond-mat.mtrl-sci 0809.1613.
- [137] N. L. Abraham, *A Genetic Algorithm for Crystal Structure Prediction*, PhD thesis, Department of Physics, University of York, 2006.
- [138] N. L. Abraham and M. I. J. Probert, Phys. Rev. B **73**, 224104 (2006).
- [139] N. L. Abraham and M. I. J. Probert, Phys. Rev. B **77**, 134117 (2008).

- [140] C. J. Pickard and R. J. Needs, Phys. Stat. Sol. (b) **236**, 536 (2009).
- [141] C. J. Pickard and R. J. Needs, Phys. Rev. Lett. **97**, 045504 (2006).
- [142] M. I. Eremets, I. A. Trojan, S. A. Medvedev, J. S. Tse, and Y. Yao, Science **319**, 1506 (2008).
- [143] C. J. Pickard and R. J. Needs, Phys. Rev. B **76**, 144114 (2007).
- [144] I. Goncharenko *et al.*, Phys. Rev. Lett. **100**, 045504 (2008).
- [145] G. Csányi, C. J. Pickard, B. D. Simons, and R. J. Needs, Phys. Rev. B **75**, 085432 (2007).
- [146] C. J. Pickard and R. J. Needs, Nature Physics **3**, 473 (2007).
- [147] C. J. Pickard and R. J. Needs, J. Chem. Phys. **127**, 244503 (2007).
- [148] C. J. Pickard and R. J. Needs, Nature Materials **7**, 775 (2008).
- [149] S. Baroni, S. de Gironcoli, A. Dal Corso, and P. Giannozzi, Rev. Mod. Phys. **73**, 515 (2001).
- [150] D. Porezag and M. R. Pederson, Phys. Rev. B **54**, 7830 (1996).
- [151] P. Hasnip, A rough guide to elnes/eels with castep, 2008.
- [152] C. J. Pickard, *Ab initio Electron Energy Loss Spectroscopy*, PhD thesis, University of Cambridge, 1997.
- [153] D. N. Jayawardane, C. J. Pickard, L. M. Brown, and M. C. Payne, Phys. Rev. B **64**, 115107 (2001).
- [154] C. J. Pickard and F. Mauri, Phys. Rev. Lett. **88**, 086403 (2002).
- [155] C. G. Van de Walle and P. E. Blöchl, Phys. Rev. B **47**, 4244 (1993).
- [156] C. G. Van de Walle and J. Neugebauer, Annu. Rev. Mater. Res. **36**, 179 (2006).
- [157] M. Budde *et al.*, Phys. Rev. B **57**, 4397 (1998).
- [158] R. J. Needs, J. Phys.: Condens. Matter **11**, 10437 (1999).
- [159] S. Goedecker, T. Deutsch, and L. Billard, Phys. Rev. Lett. **88**, 235501 (2002).
- [160] E. R. Batista *et al.*, Phys. Rev. B **74**, 121102 (2006).
- [161] W.-K. Leung, R. J. Needs, G. Rajagopal, S. Itoh, and S. Ihara, Phys. Rev. Lett. **83**, 2351 (1999).
- [162] B. N. Muskashev, K. A. Abdullin, and Y. V. Gorelkinskii, Phys. Stat. Sol. (a) **169**, 73 (1998).
- [163] T. A. G. Eberlein, N. Pinho, R. Jones, B. J. Coomer, and J. Goss, Physica B **308-310**, 454 (2001).

- [164] P. Deák, M. Heinrich, L. C. Snyder, and J. W. Corbett, Mater. Sci. Eng. **B4**, 57 (1989).
- [165] C. G. Van de Walle and J. Neugebauer, Phys. Rev. B **52**, R14320 (1995).
- [166] P. Deák, L. C. Snyder, M. Heinrich, C. R. Ortiz, and J. W. Corbett, Physica B **170**, 253 (1991).
- [167] J. L. Hastings, M. Gharaibeh, S. K. Streicher, and P. A. Fedders, Physica B **273-274**, 216 (1999).
- [168] O. K. Al-Mushadani and R. J. Needs, Phys. Rev. B **68**, 235205 (2003).
- [169] A. E. Mattsson, R. R. Wixom, and R. Armiento, Phys. Rev. B **77**, 155211 (2008).
- [170] J. P. Perdew, K. Burke, and M. Ernzerhof, Phys. Rev. Lett. **77**, 3865 (1996).
- [171] S. G. Louie, S. Froyen, and M. L. Cohen, Phys. Rev. B **26**, 1738 (1982).
- [172] K. J. Chang and D. J. Chadi, Phys. Rev. B **40**, 11644 (1989).
- [173] C. G. Van de Walle, Y. Bar-Yam, and S. T. Pantelides, Phys. Rev. Lett. **60**, 2761 (1988).
- [174] C. G. Van de Walle, P. J. H. Denteneer, Y. Bar-Yam, and S. T. Pantelides, Phys. Rev. B **39**, 10791 (1989).
- [175] C. G. Van de Walle, Phys. Rev. B **49**, 4579 (1994).
- [176] D. J. Chadi, Appl. Phys. Lett. **83**, 3710 (2003).
- [177] W. Kaiser and C. D. Thurmond, J. Appl. Phys. **30**, 427 (1959).
- [178] K. Sumino, I. Yonenaga, M. Imai, and T. Abe, J. Appl. Phys. **54**, 5016 (1983).
- [179] H. Ishii *et al.*, J. J. Appl. Phys. **35**, L1385 (1996).
- [180] R. Sauer, J. Weber, and W. Zulehner, Appl. Phys. Lett. **44**, 440 (1984).
- [181] J. P. Goss, I. Hahn, R. Jones, P. R. Briddon, and S. Öberg, Phys. Rev. B **67**, 045206 (2003).
- [182] H. J. Stein, Appl. Phys. Lett. **47**, 1339 (1985).
- [183] K. L. Brower, Phys. Rev. B **26**, 6040 (1982).
- [184] R. Jones, S. Öberg, F. Berg Rasmussen, and B. Bech Nielsen, Phys. Rev. Lett. **72**, 1882 (1994).
- [185] H. Kageshima, A. Taguchi, and K. Wada, Appl. Phys. Lett. **76**, 3718 (2000).
- [186] H. Sawada and K. Kawakami, Phys. Rev. B **62**, 1851 (2000).
- [187] A. Gali, J. Miro, P. Deák, C. P. Ewels, and R. Jones, J. Phys.: Condens. Matter **8**, 7711 (1996).

- [188] J. L. McAfee, H. Ren, and S. K. Estreicher, Phys. Rev. B **69**, 165206 (2004).
- [189] A. Karoui, F. Sahtout Karoui, G. A. Rozgonyi, M. Hourai, and K. Sueoka, J. Elect. Soc. **150**, G771 (2003).
- [190] V. V. Voronkov and R. Falster, Solid State Phenom. **108-109**, 139 (2004).
- [191] N. Fujita *et al.*, Appl. Phys. Lett. **87**, 021902 (2005).
- [192] N. Stoddard, P. Pichler, G. Duscher, and W. Windl, Phys. Rev. Lett. **95**, 025901 (2005).
- [193] H. Sawada, K. Kawakami, A. Ikari, and W. Ohashi, Phys. Rev. B **65**, 075201 (2002).
- [194] L. M. Porter and R. F. Davis, Mat. Sci. Eng. B **34**, 83 (1995).
- [195] J. Singh, *Physics of semiconductors and their heterostructures* (McGraw-Hill, New York, 1993).
- [196] S. Dannefaer, Phys. Stat. Sol. (c) **4**, 3605 (2007).
- [197] J. P. Goss, J. Phys.: Condens. Matter **15**, R551 (2003).
- [198] G. A. J. Amaratunga, Science **297**, 1657 (2002).
- [199] R. G. Farrer, Sol. Stat. Comm. **7**, 685 (1969).
- [200] W. V. Smith, P. P. Sorokin, I. L. Gelles, and G. J. Lasher, Phys. Rev. **115**, 1546 (1959).
- [201] G. S. Woods, J. A. van Wyk, and A. T. Collins, Philos. Mag. B **62**, 589 (1990).
- [202] G. Davis and M. F. Hamer, Proc. R. Soc. London. Ser. A **348** (1976).
- [203] A. Gali, M. Fyta, and E. Kaxiras, Phys. Rev. B **77**, 155206 (2008).
- [204] N. Fujita, R. Jones, S. Öberg, and P. R. Briddon, Diamond Rel. Mat. **17**, 123 (2008).
- [205] L. Childress *et al.*, Science **314**, 281 (2006).
- [206] M. M. V. Gurudev Dutt *et al.*, Science **316**, 1312 (2007).
- [207] C. Kurtsiefer, S. Mayer, P. Zarda, and H. Weinfurter, Phys. Rev. Lett. **85**, 290 (2000).
- [208] J. P. Goss *et al.*, Phys. Rev. B **65**, 115207 (2002).
- [209] S. K. Estreicher, M. A. Roberson, and D. M. Maric, Phys. Rev. B **50**, 17018 (1994).
- [210] P. Briddon, R. Jones, and G. M. S. Lister, J. Phys. C **21**, L1027 (1988).
- [211] S. J. Sque, R. Jones, J. P. Goss, and P. R. Briddon, Phys. Rev. Lett. **92**, 017402 (2004).

- [212] T. Miyazaki, H. Okushi, and T. Uda, Phys. Rev. Lett. **88**, 066402 (2002).
- [213] I. Z. Machi *et al.*, Physica B **289-290**, 507 (2000).
- [214] J. Chevallier *et al.*, Diamond Relat. Mater. **11**, 1566 (2002).
- [215] S. K. Streicher, Mater. Sci. Eng. **R 14**, 319 (1995).
- [216] B. Pajot, B. Clerjaud, and Z.-J. Xu, Phys. Rev. B **59**, 7500 (1999).
- [217] P. R. Briddon, Physica B **185**, 179 (1993).
- [218] R. Jones, P. R. Briddon, and S. Öberg, Philos. Mag. Lett. **66**, 67 (1992).
- [219] A. Mainwood, Phys. Rev. B **49**, 7934 (1994).
- [220] E. B. Lombardi, A. Mainwood, K. Osuch, and E. C. Reynhardt, J. Phys.: Condens. Matter **15**, 3135 (2003).
- [221] J. P. Goss, P. R. Briddon, S. Papagiannidis, and R. Jones, Phys. Rev. B **70**, 235208 (2004).
- [222] J. P. Goss, R. J. Eyre, and P. R. Briddon, Phys. Stat. Sol. (b) **245**, 1679 (2008).
- [223] E. V. Lavrov *et al.*, Phys. Rev. B **62**, 12859 (2000).
- [224] S. P. Mehandru and A. B. Anderson, J. Mater. Res. **9**, 383 (1994).
- [225] R. C. Newman, J. Phys: Condens. Matter **12**, R335 (2000).
- [226] *Oxygen in Silicon*, edited by F. Shimura, Semiconductors and Semimetals Vol. 42, (Academic Press, Orlando 1994).
- [227] J. Häkkinen *et al.*, Nucl. Instr. and Meth. **541**, 202 (2005).
- [228] H. J. Stein and S. Hahn, J. Appl. Phys. **75**, 3477 (1994).
- [229] A. R. Brown *et al.*, Semicond. Sci. Technol. **3**, 591 (1988).
- [230] *Early Stages of Oxygen Precipitation in Silicon* edited by R. Jones, NATO Advanced Science Institutes, Series 3: High Technology, Vol. 17 (Kluwer Academic, Dordrecht, 1996).
- [231] X. Pi, D. Yang, X. Ma, Q. Shui, and D. Que, Phys. Stat. Sol. (b) **221**, 641 (2000).
- [232] N. Fujita, R. Jones, S. Öberg, and P. R. Briddon, Appl. Phys. Lett. **91**, 051914 (2007).
- [233] J. Coutinho, R. Jones, P. R. Briddon, and S. Öberg, Phys. Rev. B **62**, 10824 (2000).
- [234] S. Hao, L. Kantorovich, and G. Davies, Phys. Rev. B **69**, 155204 (2004).
- [235] H. Yamada-Kaneta, C. Kaneta, and T. Ogawa, Phys. Rev. B **42**, 9650 (1990).

- [236] M. Pesola, J. von Boehm, T. Mattila, and R. M. Nieminen, Phys. Rev. B **60**, 11449 (1999).
- [237] E. Artacho *et al.*, Phys. Rev. B **56**, 3820 (1997).
- [238] J. Plans, G. Diaz, E. Martinez, and F. Yndurain, Phys. Rev. B **35**, 788 (1987).
- [239] N. Needels, J. D. Joannopoulos, Y. Bar-Yam, and S. T. Pantelides, Phys. Rev. B **43**, 4208 (1991).
- [240] L. Tsetseris, S. Wang, and S. T. Pantelides, Appl. Phys. Lett. **88**, 051916 (2006).
- [241] Y. J. Lee, M. Pesola, J. von Boehm, and R. M. Nieminen, Phys. Rev. B **66**, 075219 (2002).
- [242] M. Pesola, Y. Joo Lee, J. von Boehm, M. Kaukonen, and R. M. Nieminen, Phys. Rev. Lett. **84**, 5343 (2000).
- [243] S. N. Rashkeev, M. D. Ventra, and S. T. Pantelides, Appl. Phys. Lett. **78**, 1571 (2001).
- [244] D. J. Chadi, Phys. Rev. Lett. **77**, 861 (1996).
- [245] Y. J. Lee and R. M. Nieminen, Comp. Phys. Comm. **142**, 305 (2001).
- [246] H. Ono, Appl. Phys. Express **1**, 025001 (2008).
- [247] A. Gali, J. Miro, P. Deák, C. P. Ewels, and R. Jones, J. Phys.: Condens. Matter **8**, 7711 (1996).
- [248] N. Fujita, R. Jones, S. Öberg, and P. R. Briddon, J. Mater. Sci. Mater. Electron. **18**, 683 (2007).
- [249] R. Jones *et al.*, Semicond. Sci. Technol. **9**, 2145 (1994).
- [250] S. K. Estreicher, Phys. Rev. B **41**, 9886 (1990).
- [251] M. Ramamoorthy and S. T. Pantelides, Solid State Commun. **106**, 243 (1998).
- [252] R. Jones, S. Öberg, and A. Umerski, Mater. Sci. Forum **83**, 551 (1992).
- [253] R. Jones, W. Jackson, A. M. Stoneham, R. C. Newman, and M. Symons, Phil. Trans. Roy. Soc. Lon. Ser. A **350**, 1693 (1995).
- [254] V. P. Markevich and M. Suezawa, J. Appl. Phys. **83**, 2988 (1998).
- [255] G. I. G. Griffiths, C. J. Pickard, and R. J. Needs, arXiv:0906.4467v1 (2009).
- [256] C. J. Pickard and R. J. Needs, Phys. Rev. Lett. **102**, 146401 (2009).
- [257] C. J. Pickard and R. J. Needs, Phys. Rev. Lett. **102**, 125702 (2009).
- [258] J. P. Bouchaud, A. Georges, and C. Lhuillier, J. Phys. France **49**, 553 (1988).

Index

- AIRSS
 Advantages, 97
 Constraints, 95, 108
- Aliasing, 26
- ARPES technique, 6
- Backflow function, 42
- Band structure, 6, 28
- Basin hopping method, 90
- Basin of attraction, 85
- Bethe-Salpeter equation, 6
- Bisection search, 85
- Bond saturation, 120
- Born-Oppenheimer approximation, 10
- Bose gasses, 36
- Brillouin zone sampling
 Multi-B scheme, 30, 109
- Chemical accuracy, 24
- Condensate fraction, 68
- Conjugate gradients method, 85
- Convergence
 DFT, 23
- Correlated sampling, 44
- Correlation
 Energy, 13
- Cost function, 43
- Coupled cluster technique (CC), 15, 36
- Crick, Francis, 81
- Cusp conditions, 42
- Darwin, Charles, 91
- Defect
 Colour centres, 100
 Complex, 100
 Self-interstitial, 100
- Degeneracy of structures, 118
- Density-matrix
 One-body, 66
 Two-body, 66
- DFT, 16
 Bandgap problem, 21
- DNA, 81
- EELS technique, 5, 100
- Electron-by-electron algorithm, 40
- Energy
 Correlation , *see* Correlation Energy
 Exchange, 13
 Free, Helmholtz, 118
 Landscape, 84
 Local, 39
 Self interaction, 13
 Surface, 84
- Entropy
 Configurational, 118
- Evolutionary Algorithm, 92
- Exact exchange method, 20
- Exponential wall, 164
- Fixed-node approximation, 45
- Fourier transform, 26
- Franklin, Rosalind, 81
- Generalised gradient approximation (GGA),
 20
- Golden ratio search, 85
- Green's function
 Branching, 48
 Drift and diffusion, 48
 Many-body, 46
- GW approximation, 6, 20
- H₂O clusters, 36

- Halley, Edmund, 9
Hartree method, 10
Hartree-Fock method, 12
Helium-3, 43
Helium-4, 43
Hohenberg-Kohn theorem, 16
Holme Fen, 89
Homogeneous electron gas, 36
 2-D, 43
Hydrogen Storage, 82

Jastrow function, 42
John O'Groats, 89

Kohn-Sham theory, 17

LDA, *see* Local density approximation
Learn-on-the-fly technique, 5
Lennard-Jones Clusters, 87
Line minimiser, 85
Linear program, 117
Local density approximation, 19
Local vibrational modes, 102

MCSCF technique, 14
Metropolis algorithm, 39
Miescher, Friedrich, 81
Minimisation
 Re-weighted, 44
 Un-reweighted, 44
Molecular crystals, 82, 90
Møller-Plesset theory, 15, 36

Newton, Isaac, 9
Nodal pockets, 52
NP-hard problems, 77, 85
Nuclein, 81

OEP method, 20

Pöschl-Teller interaction, 58
Parallel tempering technique, 90
Pauli exclusion principle, 12
Planewaves, 22
Point defects, 83
Population control bias, 49
Pseudopotentials, 22

Raman scattering, 102
Re-blocking method, 40
Semiconductors, 82
 Doping, 83
Silicon
 Self interstitial, 105
Simpson's rule, 35
Simulation, 1
Slater determinant, 12, 169, 171
Stagnation, 91
Steepest descents method, 85

Temperature bouncing method, 89
Three body problem, 9
Timestep error, 49

Variational principle, 10
Watson, James, 81
X-ray crystallography, 83